

INFORMATION TO USERS

This manuscript has been reproduced from the microfilm master. UMI films the text directly from the original or copy submitted. Thus, some thesis and dissertation copies are in typewriter face, while others may be from any type of computer printer.

The quality of this reproduction is dependent upon the quality of the copy submitted. Broken or indistinct print, colored or poor quality illustrations and photographs, print bleedthrough, substandard margins, and improper alignment can adversely affect reproduction.

In the unlikely event that the author did not send UMI a complete manuscript and there are missing pages, these will be noted. Also, if unauthorized copyright material had to be removed, a note will indicate the deletion.

Oversize materials (e.g., maps, drawings, charts) are reproduced by sectioning the original, beginning at the upper left-hand corner and continuing from left to right in equal sections with small overlaps.

Photographs included in the original manuscript have been reproduced xerographically in this copy. Higher quality 6" x 9" black and white photographic prints are available for any photographs or illustrations appearing in this copy for an additional charge. Contact UMI directly to order.

**ProQuest Information and Learning
300 North Zeeb Road, Ann Arbor, MI 48106-1346 USA
800-521-0600**

UMI[®]

GUIDE STAR LASERS FOR ADAPTIVE OPTICS

by

William Thomas Roberts, Jr.

Copyright © William Thomas Roberts, Jr. 2001

A Dissertation Submitted to the Faculty of the
DEPARTMENT OF OPTICAL SCIENCES
In Partial Fulfillment of the Requirements
For the Degree of
DOCTOR OF PHILOSOPHY
In the Graduate College
THE UNIVERSITY OF ARIZONA

2001

UMI Number: 3023498

**Copyright 2001 by
Roberts, William Thomas, Jr.**

All rights reserved.

UMI[®]

UMI Microform 3023498

Copyright 2001 by Bell & Howell Information and Learning Company.

**All rights reserved. This microform edition is protected against
unauthorized copying under Title 17, United States Code.**

**Bell & Howell Information and Learning Company
300 North Zeeb Road
P.O. Box 1346
Ann Arbor, MI 48106-1346**

THE UNIVERSITY OF ARIZONA ©
GRADUATE COLLEGE

As members of the Final Examination Committee, we certify that we have read the dissertation prepared by W. Thomas Roberts entitled Guide Star Lasers for Adaptive Optics

and recommend that it be accepted as fulfilling the dissertation requirement for the Degree of Doctor of Philosophy

Roger Angel
Roger Angel

4/13/01
Date

Richard L. Shoemaker
Richard L. Shoemaker

4/13/01
Date

Robert Eckardt
Robert Eckardt

4/13/01
Date

Date

Final approval and acceptance of this dissertation is contingent upon the candidate's submission of the final copy of the dissertation to the Graduate College.

I hereby certify that I have read this dissertation prepared under my direction and recommend that it be accepted as fulfilling the dissertation requirement.

Roger Angel
Dissertation Director, Roger Angel

4/13/01
Date

STATEMENT BY AUTHOR

This dissertation has been submitted in partial fulfillment of requirements for an advanced degree at The University of Arizona and is deposited in the University Library to be made available to borrowers under rules of the Library.

Brief quotations from this dissertation are allowable without special permission, provided that accurate acknowledgment of source is made. Requests for permission for extended quotation from or reproduction of this manuscript in whole or in part may be granted by the copyright holder.

SIGNED: *Tom Roberts*

ACKNOWLEDGEMENTS

I am grateful to my advisor and mentor, Professor Roger Angel who has taught me, among other things, a small part of his gift of thinking 'outside the box'. Though I cannot yet approach his skill in grasping the fundamental parameters, I can at least begin to appreciate it. To the many other professors in Optical Sciences and Astronomy who have been of such valuable assistance, I must also say 'thank you'. In particular I acknowledge, Dr. Jim Palmer who has everything imaginable in his lab, and more impressively, knows where to find it; Dr. Robert Eckardt, whose calm, careful, methodical and thoughtful manner helped me through many a difficult obstacle; Professors Shoemaker, Powell and Kost, all of whom served as very valuable references in the vast field of laser physics; Prof. Ewan Wright for his enthusiastic instruction in laser resonators and beam propagation; and Professor Jack Gaskill and Dr. Don McCarthy for their insights, guidance and helpful discussions.

I appreciate the opportunity afforded by James Murray and Bill Austin to learn from them at Lite Cycles, Inc.

The staff at The Optical Sciences Center and Steward Observatory have repeatedly proven their immense value to their organizations and all of us who depend on them. Thanks to Brigitte Lawson, Barbara Myers, Anne Klocko, Michelle Cournoyer, Joy Facio, Kimberly Chapman and Doris Tucker. It has been a joy to work with each of you.

Thanks to Chris Dainty at Imperial College for including me in the Laser Guide Star Adaptive Optics workshop in 1997, and to Keith Wilson at the Jet Propulsion Laboratory for reading the manuscript and for helpful suggestions.

In addition, there have been many people whose friendship has made the years at the University of Arizona some of the happiest and most fulfilling of my life. Among those meriting special recognition are Georg Mohs, Sandra Bonilla, Katie Liao, Debra Osborne, Jake Jacobsen, Michal and Zora Mlejnek, Roland Sarlot, Elena Moise, Julie Swann, Celeste Steen, Matt Kenworthy and Doug Miller. I must thank Ty Martinez whose fateful warning, 'Don't do lasers!' I probably should have heeded. Special thanks to *Der L^AT_EX Meister*, Norbert Sigrist who repeatedly helped me with 11th hour bailouts. One very close friend deserving special recognition is Heidi Ruffner; without her encouragement, I never would have undertaken this degree, and without her repeated help in growing thin films, I might never have finished it. Without the help of George Kastis, I might not have passed prelims, and without the support and encouragement of Mitsuko Kono I might not have finished this dissertation. Thank you all very much.

This work was supported by Air Force Research Grants F49620-96-1-0366, F49620-99-1-0285 and F49620-00-1-0294.

DEDICATION

For their constant love, encouragement and support, this work is dedicated to my parents, Bill and Bettie Roberts.

TABLE OF CONTENTS

LIST OF FIGURES	10
LIST OF TABLES	12
ABSTRACT	13
I Introduction and Summary	15
CHAPTER 1. INTRODUCTION - IN SEARCH OF GUIDANCE	16
CHAPTER 2. EXECUTIVE SUMMARY	20
2.1. Overview and Goals	20
2.2. Dye Laser	20
2.3. Raman Lasers	21
2.4. Temperature-Tuned Nd:YAG Laser	22
2.5. Color Center Laser	22
2.6. Mn:Apatite Laser	23
II Background and Review	25
CHAPTER 3. ATMOSPHERIC TURBULENCE EFFECTS	26
3.1. Astronomical Systems	26
3.2. Atmospheric Turbulence	27
3.2.1. The Structure Function	28
CHAPTER 4. WAVEFRONT CORRECTION SYSTEMS	31
4.1. Wavefront Sensor	31
4.2. Deformable Element	32
4.3. Guide Stars	33
4.3.1. Natural Guide Stars	34
4.3.2. Temporal Correlation	36
4.4. Artificial Guide Stars	37
4.4.1. Focal Anisoplanatism: The Cone Effect	38
4.4.2. Global Tilt	39
4.4.3. Scattering Mechanisms	39

TABLE OF CONTENTS—*Continued*

CHAPTER 5. GUIDE STAR LASER REQUIREMENTS	42
5.1. The Sodium Atom	42
5.2. Thermospheric Sodium	48
5.2.1. Height and Abundance	48
5.2.2. Sodium Temperature and Doppler Broadening	49
5.3. Sodium Saturation	50
5.4. Implications for Guide star Lasers	52
5.4.1. Temporal Considerations	53
5.4.2. Spectral Considerations	56
5.5. Review of Sodium Guide Star Lasers	58
III Sodium Guide Star Laser Research	62
CHAPTER 6. DYE LASER DEVELOPMENT	63
6.1. Background	63
6.2. Ring Laser Development	64
6.3. Power Optimization	66
6.3.1. End Pumping	67
6.3.2. Faraday Etalon	70
6.3.3. Optical Rotator Etalon	77
6.4. Measurement of Mode Structure	79
6.5. Conclusions	82
CHAPTER 7. RAMAN LASER DEVELOPMENT	83
7.1. Introduction	83
7.1.1. Nonlinear Optics	83
7.1.2. Spontaneous Raman Scattering	84
7.1.3. Stimulated Raman Scattering	87
7.2. Review of Potential Raman Laser Candidates	89
7.2.1. Raman-active Materials	89
7.2.2. High Power Lasers	91
7.2.3. Potential Combinations	95
7.2.4. Previous Work	99
7.3. CaWO ₄ Raman-shifted Laser Experiments	100
7.3.1. CaWO ₄ Shifted Nd:YAG	100
7.3.2. CaWO ₄ Raman-shifted Nd:YAG	105
7.4. Conclusion	113

TABLE OF CONTENTS—Continued

CHAPTER 8. THE COLD ND:YAG LASER	116
8.1. Background	116
8.2. Design	118
8.2.1. Zigzag Slab	119
8.2.2. Cooling Assembly	122
8.2.3. Indium Contacting	124
8.2.4. SiO ₂ Waveguide Layer	129
8.3. Testing and Results	132
8.3.1. Cooling and Nd:YAG Transmission Tests	132
8.3.2. Lasing Tests	133
8.4. Analysis and Conclusions	135
CHAPTER 9. COLOR CENTER LASER	138
9.1. Color Centers	138
9.2. Color Center Laser Development	142
9.2.1. Thermal Defocus Measurements	144
9.3. Conclusions	147
CHAPTER 10. THE APATITE LASER	149
10.1. Introduction and Background	149
10.2. Apatite (Mn:Ca ₅ (PO ₄) ₃ F)	151
10.3. Apatite Fluorescence	156
10.4. Lasing Efforts	159
10.4.1. Three Level Atom Model	159
10.4.2. Fluorescence Measurements	161
10.4.3. Transmission Data	166
10.4.4. Thermal Stress Analysis	168
10.4.5. Lasing Efforts	170
10.5. Discussion and Conclusion	171
 IV The Road Ahead	 173
CHAPTER 11. NEW SODIUM LASER CONCEPTS	174
11.1. CW fiber laser	174
11.2. Interleaved Q-switched Lasers	178
11.3. Diamond Color Center Laser	182
11.4. Conclusions	186

TABLE OF CONTENTS—Continued

APPENDIX A. ATOMIC LEVELS OF Mn^{5+}	188
A.1. Theory of the Mn^{5+} Free Ion	188
A.1.1. L S Coupling	194
A.1.2. Relativistic Corrections	197
A.1.3. Two $3d$ electrons	199
APPENDIX B. RAYLEIGH BEACONS	202
REFERENCES	210

LIST OF FIGURES

FIGURE 4.1.	Strehl ratio dependence on separation angle	36
FIGURE 5.1.	Spectral response of mesospheric sodium layer.	46
FIGURE 5.2.	Lorentz-broadened Na spectral absorption cross-section	47
FIGURE 5.3.	Doppler-broadened Na-layer number densities	50
FIGURE 6.1.	Ring dye laser layout.	64
FIGURE 6.2.	Dye laser beam quality	67
FIGURE 6.3.	Area of overlap in dye jet in which pumping is effective.	68
FIGURE 6.4.	Argon-ion pumping vs. pump incidence angle.	69
FIGURE 6.5.	Faraday etalon usage.	73
FIGURE 6.6.	Predictions of etalon tuning	74
FIGURE 6.7.	High scatter from Faraday etalon	75
FIGURE 6.8.	Rotatory power of TeO ₂	78
FIGURE 6.9.	Faraday etalon and TeO ₂ etalon tuning	79
FIGURE 6.10.	Fabry-Perot Monitoring of sodium dye laser.	80
FIGURE 7.1.	Energy diagrams depicting various Raman processes	84
FIGURE 7.2.	Spectral dependence of Raman scattering coefficient	86
FIGURE 7.3.	Scattering coefficient measurements	87
FIGURE 7.4.	Potential Raman guide star systems	95
FIGURE 7.5.	Detail of first- and second-Stokes processes	97
FIGURE 7.6.	Selected Laser/Raman combinations	98
FIGURE 7.7.	Gain curve of TRW Raman laser	100
FIGURE 7.8.	Raman spectrum of CaWO ₄	101
FIGURE 7.9.	CaWO ₄ Raman laser experimental setup	103
FIGURE 7.10.	Spectral output of Raman laser	104
FIGURE 7.11.	Compositional tuning of Nd:YAG	107
FIGURE 7.12.	CaWO ₄ -shifted Nd:YAG spectrum	108
FIGURE 7.13.	Raman laser Rigrod plot	109
FIGURE 7.14.	Power versus cavity length for Nd:YAG and Nd:YAG	110
FIGURE 7.15.	Nd:YAG laser broadening	112
FIGURE 8.1.	Thermal-induced spectral shift of Nd:YAG	117
FIGURE 8.2.	Zigzag slab laser	120
FIGURE 8.3.	Cooled zigzag laser slab	123
FIGURE 8.4.	Silver cooling pieces	124
FIGURE 8.5.	Indium contact pressure experiment	126
FIGURE 8.6.	Indium wetting spoiling TIR of prism	127
FIGURE 8.7.	Silver contact assembly diagram	128

LIST OF FIGURES—*Continued*

FIGURE 8.8. Cooled laser compression assembly	130
FIGURE 8.9. Spectrum of Nd:YAG laser as a function of temperature	134
FIGURE 8.10. Output power of the laser as a function of slab temperature.	135
FIGURE 8.11. Temperature-induced spectral shift of Nd:YAG	136
FIGURE 9.1. F ₂ color centers	140
FIGURE 9.2. Diagram of lasing action in color center materials.	141
FIGURE 9.3. Tunable color center laser diagram	142
FIGURE 9.4. Color center laser spectrum tuned to $\lambda=589$ nm	144
FIGURE 9.5. Color center laser thermal lensing experiment	145
FIGURE 9.6. Interferogram of LiF : F ₂ ⁻ color center crystal	146
FIGURE 10.1. Molecular structure of apatite.	151
FIGURE 10.2. Apatite facet planes	152
FIGURE 10.3. Portable IR spectrometer	153
FIGURE 10.4. Rough apatite crystals in beaker of CS ₂	154
FIGURE 10.5. Fracture planes in apatite	155
FIGURE 10.6. Apatite fluorescence	156
FIGURE 10.7. Apatite fluorescence spectra	157
FIGURE 10.8. 3-level atom	159
FIGURE 10.9. Fluorescence/transmission experiment	163
FIGURE 10.10. Fluorescence saturation	163
FIGURE 10.11. Apatite fluorescence yield.	164
FIGURE 10.12. Comparison of fluorescence data and functional fit.	167
FIGURE 10.13. Comparison of transmission data and functional fit.	168
FIGURE 10.14. Apatite laser cavity mode volume.	171
FIGURE 11.1. Power-dependent gain spectrum of fused silica fiber.	176
FIGURE 11.2. Spectral output of a fiber Raman laser	176
FIGURE 11.3. Spectral reflectivity of a narrow-band FBG.	178
FIGURE 11.4. Mechanically Q-switched Nd:YAG laser	179
FIGURE 11.5. Multiple Q-switched Nd:YAG lasers	181
FIGURE 11.6. H3 diamond color center spectra	183
FIGURE 11.7. Tuned diamond color center laser output.	184
FIGURE B.1. Atmospheric molecular density versus altitude	205
FIGURE B.2. Modeled O ₃ spectral absorption	206
FIGURE B.3. Modeled spectral transmission curves	207
FIGURE B.4. Modeled spectral return from Rayleigh laser	207
FIGURE B.5. Modeled spectral returns from telescope at 3 km altitude	208
FIGURE B.6. Rayleigh laser return intensity versus scattering altitude	209

LIST OF TABLES

TABLE 2.1.	List of Research Accomplishments	24
TABLE 5.1.	Summary of Sodium Guide Star Lasers	59
TABLE 7.1.	Raman shifting materials	91
TABLE 7.2.	High power gas/ion lasers	92
TABLE 7.3.	High power solid state lasers	93
TABLE 7.4.	High power glass lasers	94
TABLE 7.5.	High power tunable solid state lasers	95
TABLE 8.1.	Cooling assembly materials	126

ABSTRACT

Exploitation of the imaging capabilities of the new generation of ground-based astronomical telescopes relies heavily on Adaptive Optics (AO). Current AO system designs call for sodium guide star lasers capable of producing at least eight Watts of power tuned to the peak of the sodium D_2 line, with a high duty cycle to avoid saturation, and with 0.5-1.0 GHz spectral broadening. This work comprises development and testing of six candidate laser systems and materials which may afford a path to achieving these goals.

An end-pumped CW dye laser producing 4.0 Watts of tuned output power was developed and used to obtain the first accurate measurement of sodium layer scattering efficiency. Methods of optimizing the laser output through improving pump overlap efficiency and reducing the number of intracavity scattering surfaces are covered.

The 1181 nm fluorescence peak of Mn^{5+} ion in $Ba_5(PO_4)_3Cl$ could be tuned and doubled to reach 589 nm. While efforts to grow this crystal were under way, the Mn^{5+} ion in natural apatite ($Ca_5(PO_4)_3F$) was studied as a potential laser material. Fluorescence saturation measurements and transmission saturation are presented, as well as efforts to obtain CW lasing in natural apatite.

A Q-switched laser color-center laser in $LiF : F_2^-$ was developed and successfully tuned and doubled to the sodium D_2 line. Broad-band lasing of 80 mW and tuned narrow-band lasing of 35 mW at 1178 nm were obtained with 275 mW of input pump power at 1064 nm. The measured thermal properties of this material indicate its potential for scaling to much higher power.

A Q-switched intracavity Raman laser was developed in which $CaWO_4$ was used to shift a Nd:YAG laser, the frequency-doubled output of which was centered at 589.3 nm. To obtain light at 589.0 nm, a compositionally tuned pump laser of $Nd : Y_3Ga_{1.1}Al_{3.9}O_{12}$ was produced which generated the desired shift, but was in-

homogeneous broadened, limiting the tunable power of the material. Finally, temperature tuning of a Nd:YAG laser was demonstrated in which the laser emitted up to 8.6 Watts at a temperature of -21.5 C, bringing the wavelength into a regime favorable for efficient Raman shifting by CaWO_4 .

Part I

Introduction and Summary

Chapter 1

INTRODUCTION - IN SEARCH OF GUIDANCE

Bright star! Would I were steadfast, as thou art.

- John Keats

Since the dawn of history, civilizations have looked to the stars for guidance, literally and figuratively. The ancient Phoenicians used the star Thuban as their 'pole star' in their navigation throughout the Mediterranean. The Magi of Christian tradition found the infant Jesus by following the Star of Bethlehem. The ability of the stars to provide an accurate, immutable reference for guidance has been exploited over the years with the development of the sextant and astrolabe aiding the seafarers of the last two centuries, much as modern star-trackers provide guidance to satellites and interplanetary spacecraft today.

The motions of the 'wandering stars', the planets and comets, have been thought to foretell events, and as such have served as a guide, however unreliable, to the ancients. The appearance of Halley's comet before the Norman invasion of England had a polarizing effect on the morale of both armies, and its appearance at the coming of Cortez is said to have plunged Montezuma into such a profound depression that the enormous and powerful Aztec empire virtually accepted defeat at the hands of a small ill-equipped party without a fight. Yet the discoveries of the great 'scientific' astronomers of old, Copernicus, Kepler and Galileo, began to show the planets for the physical objects that they are, and along with Newton's theories of gravitation, demonstrated that they are subject to the same laws of motion that we observe here on Earth. By connecting the motions of the heavenly bodies with terrestrial physical principles, astronomers began to slowly chip away at the fantasy that these extraterrestrial objects somehow control earthly destinies. So successful has astronomy been

at severing this link, that the majority of educated people look with a jaundiced eye upon those who continue to look to the stars for guidance.

How ironic that astronomers themselves are now feverishly seeking their own 'guide stars', celestial objects which they find essential to understand and interpret earthly phenomena! Without guide stars, the new generation of large telescopes springing up around the world cannot realize the resolution they might otherwise be capable of, being limited by the same 'tremors of atmosphere' that Newton recognized over 300 years ago. Far from assisting with occult, mystical augury, these guide stars are used as sources of light which probe the atmosphere above telescopes. With the information that can be gleaned from this light as it traverses the unruly currents of air, modern electronic soothsayers can divine the appropriate spells to cast over the light, and reveal images of the heavens that were once clouded.

Development of a suitable guide star has been the ultimate motivation for all of the research contained herein. The directionality and relative monochromaticity of lasers makes them useful for exciting small patches high-altitude atmospheric constituents to emit light, which then acts as an apparent guide star. While straightforward in principle, the devil is in the details; it is a problem that many have grappled with, with varying degrees of success. Those guide star lasers which can be considered a success are too cumbersome, too risky, and most importantly, too expensive for their use by any but the most well endowed of observatories, causing us to question just how 'successful' they really are.

The research that is described in this dissertation has been mostly experimental in nature, prototyping and testing various laser technologies that show some degree of promise for production of an effective, efficient guide star. It is hard to imagine a research project that could give a more broad, experimental overview of general laser physics than this. Throughout the course of this investigation, it has provided the opportunity to work with many categories of laser; gain materials of solid, liquid, gas and plasma; lasing transitions of two, three and four levels; homogeneously broad-

ened, inhomogeneously broadened and mixed; lasing transitions of organic dyes, rare earth ions, transition metal ions, and radiation-induced color centers; cavities which are planar, ring, standing-wave z-shaped, concentric and hemispherical; and continuous, flash-lamp pumped, Q-switched and mode-locked temporal profiles. Beyond that, understanding the experiments and effects has reinforced my education in much of optics, and indeed of physics in general. It has required the development and use of many interferometers (Fizeau, Mach-Zehnder, Twyman-Green, Smartt point diffraction interferometer and Fabry-Perot), the application of geometrical design and aberration minimization, the propagation and measurement of Gaussian beams, and detailed radiometric analyses. Solution to the various problems that arose in the course of these investigations has required many a refresher in my atrophied knowledge (circuit theory, thermomechanics, quantum mechanics, solid-state theory, and group theory) and development of new skills (Windows programming and laboratory plumbing).

In my work operating the dye laser at the Multiple Mirror Telescope (MMT), many hours were spent in optimizing and reworking the system, trying to eke out a little more power. The cavity was configured and reconfigured, seemingly *ad infinitum* in order to maintain the system at its peak operating efficiency. In retrospect, the long, lonely nights in the noisy, windy, cold pit of the MMT provided an excellent opportunity to learn the basics of lasers, and the limits of what can and can't be done with them. The theory of the classroom is necessary, but does not provide the grounding in reality that actually working with a homemade research laser can give. It is in working with this system that I learned all of the little tricks of alignment, measurement, optimization, and understanding that serve so well in attempting to develop more advanced laser systems.

I have had help with much of the work here, whether through thoughtful discussions with those who understand the workings of solid state lasers, or through following on with the ideas and suggestions of other researchers. In many cases (such

as the development of the apatite laser material or the work with the neodymium-doped yttrium gallium aluminum garnet (Nd:YAG) laser) I was following through with work conceived and initiated by others. However, in all parts described here, I played the major role, unless otherwise noted.

Part I of this thesis is intended to preview the remainder of the dissertation, and to provide a succinct overview of my contributions to the field of guide star laser research and development. As such, it merely touches upon the highlights of each of the several projects, avoiding the minutiae of the data acquired, the analyses performed, and dead-ends abandoned. The remainder of the dissertation distills these details to provide the relevant results of the work performed over the past few years. Part II is an overview of the problem of atmospheric turbulence, and the methods by which adaptive optical systems address these problems. In these chapters, the stage is set for understanding the sodium guide star laser concept, and the stringent requirements than any such laser must meet. Finally, it provides a short review of some of the efforts applied to the development of sodium guide stars. Part III contains the bulk of the research, and the most important results that have resulted from it. These chapters detail work that was performed on a number of laser systems, all of them very different in design and specifics of operation, but all intended to push the technology toward a useful sodium guide star laser. The dissertation concludes with Part IV which contains ideas and concepts for future research and development. As such, it is lacking in much of the numerical detail required for direct implementation of the ideas. Nevertheless, I hope to be able to pursue some of these ideas in the near future. Having consumed several years of my life, the topic is of such interest to me that it is difficult to imagine myself not in pursuit of this goal.

Chapter 2

EXECUTIVE SUMMARY

2.1 Overview and Goals

Astronomical adaptive optical (AO) systems are effective for reducing the blurring of astronomical images induced by atmospheric turbulence, but require an artificial source of light, a *guide star*, above the turbulence to work when no bright natural star is present. A laser tuned to the sodium D_2 line at 588.995 nm can excite mesospheric sodium producing an effective guide star.

So far there are no good, working sodium guide star lasers. Ideally, one wants at least 8 W tuned exactly to the $F=2$ peak of the D_2 line with a spectral width of 1 GHz (0.001 nm). The laser must operate at a combination of spectral broadening and duty cycle to avoid saturation of the sodium layer.

This research has been a broad experimental investigation of lasers with the potential to achieve these goals. This chapter summarizes the results of these studies, leaving the details of the experiments and data analysis to the individual chapters in Part III. Six lasers have been investigated: a continuous-wave (CW) dye laser, an Nd:YAG/CaWO₄ Raman laser, an Nd:YAG/CaWO₄ Raman laser, a temperature-tuned Nd:YAG laser, a LiF : F₂⁻ color center laser, and an Mn:apatite laser.

2.2 Dye Laser

The tunability, multi-Watt power level and commercial availability of dye lasers has made them useful as sodium guide star lasers, and so far the only ones that have been used to obtain scientific results. However, the available dye lasers are limited in power to 3 W, are unreliable and require constant maintenance and supervision.

At the MMT, we have developed a ring dye laser operating on a single 10 MHz-broad frequency within ± 300 MHz of the center of the $F=2$ peak of the Doppler-broadened sodium line 90% of the time. This laser can reliably produce 3.4 W of tuned power, and occasionally over 4 W has been achieved. It was used to make the first measurement of CW guide star return brightness as a function of sodium column density [36].

Several concepts for reducing the losses limiting the laser power were implemented. I developed an etalon which effected a Faraday rotation of the beam polarization, allowing a single intracavity element to perform the function of tuner and Faraday rotator. I developed the concept of using a TeO_2 etalon as the optical rotator, and installed a remote-tuning system allowing us to seal the dye laser against the hostile environment of the MMT laser room. Finally, I implemented a collinear pumping system which boosted the output power by 13%.

2.3 Raman Lasers

Frequency-doubled solid state lasers are relatively reliable, efficient, and powerful. However, the frequencies obtainable by the active ions in these lasers are far removed from either the 589 nm sodium D_2 line or its half-frequency of 1178 nm. Raman lasers using stimulated Raman scattering (SRS) can produce coherent output at many frequencies otherwise unattainable by solid state lasers. Raman materials generally exhibit very low gain, however, and require pulsed laser sources to pump them and high feedback ratios to maintain the stimulated scattering.

In investigating the potential of Raman lasers, a diode-pumped, Q-switched, intracavity Raman-shifted laser based on CaWO_4 shifting of Nd:YAG was developed. The doubled output of this laser was measured at 589.25 nm, between the D lines of sodium. The total power out of the laser was 0.49 W, with an input pump diode power of 5.11 W at 808 nm, for a conversion efficiency of almost 10%.

To center the doubled emission of the laser on the sodium D₂ line (589.0 nm) a unique laser crystal of Nd:YAG was grown, which moved the doubled Raman-shifted peak to 589.06 nm. However, the compositional tuning resulted in inhomogeneous broadening, reducing its usefulness as a pump laser for obtaining power at a specific frequency.

2.4 Temperature-Tuned Nd:YAG Laser

As a pump source for a CaWO₄ Raman laser which maintains the homogeneous broadening of the Nd³⁺ ion in YAG I turned to temperature tuning. Two conductively-cooled Nd:YAG zig-zag slab lasers were made, one of which operated continuously over temperature ranges from +28.9 C to -21.5 C. This laser maintained power between 6.0 and 8.6 W, with the highest powers achieved at the lowest temperatures. A continuous, repeatable shift of lasing frequency was demonstrated at these powers with a slope of 5.78×10^{-3} nm/K. Based on this trend, at a temperature of -54 C the lasing wavelength of the Nd:YAG laser would be shifted by CaWO₄ to 1177.99 nm.

The system experienced repeated daily thermal cycling to the -40 C limit of the cooling units with no thermal failure. Interferograms of the optical path length through the slab showed induced heating along the sides of the slab from differential absorption of the pump beam, resulting in a negative cylindrical lensing with a focal length of -158 mm.

2.5 Color Center Laser

A solid state analog to the dye laser is the color center laser, in which electrons trapped at the sites of displaced anions in ionic alkali-halide salts act as the gain medium. These materials exhibit high gain over a wide frequency band similar to dyes. In particular, LiF:F₂⁻ color center material has a gain peak near 1.18 μm which is ideal for doubling to 589 nm.

We used a $\text{LiF} : \text{F}_2^-$ crystal to obtain lasing at 1178 nm. The lasing bandwidth was narrowed to fit within the 3 GHz sodium line, and the frequency-doubled output of this laser was tuned precisely to the D_2 line. With 275 mW of Q-switched Nd:YAG pump power at 1064 nm, the color-center laser emitted 80 mW broad-band, and 35 mW narrow-band at 1178 nm.

2.6 Mn:Apatite Laser

As an alternative to a single high-power laser, the concept of spatially or temporally combining many inexpensive lasers was considered. The Mn^{5+} ion doped into a compositional variant of apatite known as BCAP (Barium ChlorApatite or $\text{Ba}_5(\text{PO}_4)_3\text{Cl}$) was observed to fluoresce at 1181 nm, raising the possibility of a laser which could be directly frequency-doubled to produce a sodium guide star.

As a surrogate material, several samples of natural apatite were studied, revealing a strong π -polarized fluorescence at 1161 nm, and a weaker line at 1152 nm. The fluorescence lifetime of both lines was measured to be 550 μsec at room temperature, increasing to about 700 μsec at 150 K. Weaker fluorescence peaks near 1215 nm and 1286 nm were also observed. The long lifetime and large emission cross section result in a low saturation intensity of about 2000 W/cm^2 . Measurements of the fluorescence yield clearly show saturation at high pump intensities in agreement with the calculated 2000 W/cm^2 , while the magnitude of the saturation intensity indicates a fluorescence efficiency of 75%.

Samples of BCAP were made, though only polycrystalline material was obtained. The fluorescence peak of these BCAP samples was observed at 1180 nm, with a fluorescence lifetime of less than 150 μsec .

For the fluorapatite crystal with the best combination of crystal quality and absorption a round-trip lasing gain of 8% was calculated, necessitating a high-Q cavity and antireflection coatings. A lasing cavity with a 60 μm mode diameter was pumped

Chapter	Notable Achievements
6	First reported stable laser to calibrate sodium guide star return as a function of sodium column density
6	Collinear high-power pumping of a dye laser resulting in output power increase of 13%
6	First known attempt to combine etalon tuning and Faraday rotation in one element
7	First YGAG laser operated in CW with diode pumping
7	First development of Q-switched YGAG laser
7	First YGAG laser to operate as an intracavity Raman laser. Laser was frequency-doubled and compared with sodium reference demonstrating clear shift of lasing peak to within 1 Å of sodium D ₂ peak
8	First known Nd:YAG laser designed for high-power operation substantially below room temperature
8	First known conductively cooled Nd:YAG laser to exploit temperature reduction for tuning lasing transition
8	First known conductively cooled Nd:YAG laser demonstrating continuous tuning over temperature range of 50 C
9	First reported tuned and doubled color center laser to match wavelength and linewidth of sodium resonance
10	First known measurement of saturation intensity of Mn ⁵⁺ ion in fluorapatite

TABLE 2.1. List of Research Accomplishments

with 60 mW of continuous power from $\lambda = 685$ nm laser diodes. Though lasing was never observed, the work resulted in information about the material that will further its development.

Part II

Background and Review

Chapter 3

ATMOSPHERIC TURBULENCE EFFECTS

3.1 Astronomical Systems

Astronomical telescopes are instruments for gathering and concentrating the light from, and magnifying the images of distant bodies. Ideally, the amount of light collected by a telescope (and thus the brightness of the image produced) is directly proportional to the area of the telescope's entrance pupil. The brightness of the image is, however, an inverse function of the magnifying power at which the telescope is used, so to attain bright, clear images of extremely distant or faint sources (which are key to understanding the early universe), large area telescopes are essential.

Modern telescopes have evolved over the past few decades to assist in the exploration of the universe at greater and greater distance scales. In the first half of this century, the limits of telescope size were dictated by the mechanical limitations of the times. Reflective telescopes were recognized as being less subject to index inhomogeneities and gravitationally induced warping of the optical surfaces than refractive telescopes. Recent advances in glass-working technology and lightweight structures have allowed larger and larger telescopes to be fabricated. Some of these, such as the new Multiple Mirror Telescope (MMT), Magellan telescopes and Large Binocular Telescope (LBT), use honeycomb structures for rigid but light large reflecting surfaces. Other large mirrors such as the Very Large Telescope (VLT) and Gemini telescopes use a single sheet of glass supported with an active structure. The support structure must therefore constantly measure and control the surface shape to maintain good optical performance. Finally, ushered in by the development of the old MMT and used by the Keck Ten Meter Telescopes, the concept of multiple, independently controlled apertures has found a place in the world of modern astronomy.

3.2 Atmospheric Turbulence

As telescopes grow to larger dimensions, the principal limitation in their ability to produce bright, sharp images of distant objects is the warping of light wavefronts induced by atmospheric turbulence. Light travels virtually undisturbed across the universe only to be distorted in the last few kilometers as it propagates through the denser portions of the earth's atmosphere.

The aberrations to the wavefronts that are induced manifest themselves in three particular ways. The most well-known effect is the 'twinkling' of stars observed by the naked eye. This occurs when light along various optical paths is refracted alternately toward and away from the entrance pupil of the eye. Occasionally these portions of the wavefront add constructively or destructively to vary the intensity detected at the retina. This is a very localized phenomenon (on the order of ≈ 10 cm), and tends to be averaged out as the collecting aperture becomes larger, so twinkling is not an issue for large telescopes. For telescopes, this same phenomenon gives rise to the other two effects: image wander, and image blurring. The former is produced by an overall gradient in integrated optical density along the paths that various portions of the wavefront take. If there is a higher density, whether induced by a thermal gradient or through observation at low elevation angles, an overall tilt will be imparted to the optical wavefront. Since angle in object space transforms to position in the image plane, this tilt manifests itself by moving the image on the CCD. In principle, by comparing images taken at very short intervals, this image wander could be corrected in post processing. However, very rapid measurements tend to introduce their own problems. The final effect, image blurring, arises from two separate sources. The first is related to image wander in that over long integration times, the wandering image will cause the energy to accumulate over a larger area of the CCD. The second cause is a higher order (*i.e.* smaller spatial scale) inhomogeneity in the integrated atmospheric density, which breaks up the wavefront into multiple independent wave-

fronts propagating separately. This gives rise to the ‘speckle’ phenomenon when these independent portions of the wavefront subsequently interfere at the focal plane.

3.2.1 The Structure Function

For the purposes of understanding and ultimately mitigating turbulent effects, atmospheric models based on statistical observations are used to determine the point-to-point correlation (‘structure’) of the atmosphere. The atmospheric index structure function $D_n(\rho)$ is a measure of the variance of the difference in refractive index between points separated by a distance ρ . Strictly speaking, the index structure function $D_n(\mathbf{r}, \rho)$ is a scalar function (the variance in refractive index difference) from a position \mathbf{r} to all locations ρ with respect to it, such that

$$D_n(\mathbf{r}, \rho) = n(\mathbf{r}) - n(\mathbf{r} - \rho). \quad (3.1)$$

For the purposes of adaptive optics, analysis of this function begins with two simplifying assumptions: (1) the structure function is dependent on the magnitude of the separation of the two points $\rho = |\rho|$, but not the actual direction (*i.e.* it is isotropic), and (2) it is the same for all points \mathbf{r} in the aperture (*i.e.* it is uniform). Under these assumptions it is possible to arrive at a functional dependence of D_n on ρ ,

$$D_n(\rho) = \langle |n(\mathbf{r}) - n(\mathbf{r} + \rho)|^2 \rangle = C_n^2 \rho^{2/3} \quad (3.2)$$

where C_n^2 is the so-called index structure ‘constant’, a measure of the strength of the atmospheric turbulence [106].

To first order, the atmospheric dispersion is small, so the index structure function is independent of wavelength. This is fortunate because it implies that atmospheric monitoring at one wavelength is applicable to use for correction at another wavelength. However, the correction that must be applied corrects the phase of the light wavefronts, and since phase is inversely proportional to wavelength the correction is

waveband specific. Since the final phase at a two-dimensional point \mathbf{x} in the aperture is given by

$$\phi(\mathbf{x}) = k \int_0^{l_{max}} n(\mathbf{r}) dl \quad (3.3)$$

where we have integrated along the light path l , we can rewrite the index structure function in the form of the integrated phase structure function $D_\phi(\xi)$ given by [92]

$$D_\phi(\xi) = \langle |\phi(\mathbf{x}) - n(\mathbf{x} + \xi)|^2 \rangle. \quad (3.4)$$

where the variables \mathbf{x} and ξ are two dimensional vectors in the pupil of the telescope, the third dimension along the line of site having been integrated out. For the common calculation assuming Kolmogorov turbulence [92] we obtain the phase structure function as a function of ξ , separation between points in the pupil,

$$D_\phi(\xi) = 2.91k^2 \sec(\beta) \xi^{5/3} \int_0^\infty C_n^2(h) dh. \quad (3.5)$$

This is often written in terms of the 'Fried parameter' r_0 ,

$$D_\phi(\xi) = 6.88 \left(\frac{\xi}{r_0} \right)^{5/3}. \quad (3.6)$$

The Fried parameter in this case is

$$r_0 = \left[0.423k^2 \sec(\beta) \int_0^{h_{max}} C_n^2(h) dh \right]^{-3/5} \quad (3.7)$$

in which k is the angular wave number $2\pi/\lambda$, β is the zenith angle, and the integration is performed as a function of height h across the horizontally stratified turbulent atmospheric layers to the top of the atmosphere at h_{max} . The interpretation of r_0 is roughly the radius of a circle over which the RMS wavefront variance is approximately one radian, or perhaps more illustratively, the radius of a circular area over which an aperture of the same size would result in an instantaneous diffraction-limited image [22]. The Fried parameter generally determines the size of the subapertures over which the wavefront is measured on the wavefront sensor, and the size of the

individual pupil segments which must be independently corrected at the deformable element. It is clear from the interpretations above that larger values of r_0 correspond to better seeing conditions, with 10 - 20 cm being typical.

Chapter 4

WAVEFRONT CORRECTION SYSTEMS

The advent of cheap, fast computers and associated processing and control hardware has opened up the possibility of measuring and correcting for atmospherically induced aberrations for the first time in history. The process of wavefront correction requires three general steps:

1. The wavefront must be 'mapped' to determine the positions in the pupil of excessive phase tilt or retardation.
2. The amount of retardation at each point and subsequent amount of correction to be applied must be calculated.
3. The values obtained must be applied to a deformable element.

All of these processes must be performed within a period over which the atmospheric motion is essentially negligible over a subaperture. Ideally, the area of control of a single 'actuator' of the deformable element should map to an area in the pupil that is smaller than the area of the pupil defined by the Fried parameter.

4.1 Wavefront Sensor

Before any useful correction can be applied to the deformable element of the adaptive optic (AO) system, the type and magnitude of correction to be applied must be known. This is the job of the wavefront sensor.

The most common type of wavefront sensor is the *Shack-Hartmann* sensor which was proposed by Prof. R. V. Shack in 1971 as a modification of the static Hartmann test for measuring distortion. In this device, portions of the total wavefront are

sampled by a lenslet array which is capable of measuring only the tilt (in both x and y) across each lenslet. If the wavefront is relatively planar across an individual lenslet, that portion of the wavefront will be focussed to a point on a detector array which is related to the angle of the incident wavefront with respect to the lenslet normal. In our wavefront sensor, a normally incident wavefront will create an image centered on the junction of four pixel corners. By comparing the ratios of counts detected in these four pixels, the centroid of the image can be determined. Once the centroid is located, the incident wavefront tilt for that portion of the wavefront is known. This information is determined for each portion of the wavefront, and thus a wavefront map can be reconstructed. From the wavefront map, calculation of the amount of retardation to be applied to various portions of the wavefront is a relatively simple matter¹.

4.2 Deformable Element

To date, virtually all deformable elements have been nominally flat mirror surfaces at an intervening conjugate to the telescope pupil. They have generally consisted of either thin mirrors with piezoelectric or electromagnetic actuators providing a bending force to the mirror, or moving segmented mirrors. Such systems require reconstruction of the pupil, so they are generally reimaging systems relaying the prime focus of the telescope to a remote CCD. Liquid crystal phase modulators and spatial light modulators have also been under development as elements for reshaping the wavefront.

¹Though calculation of the needed retardation is trivial, calculation of the amount of force to be applied at various positions is not. Changing the force on a particular actuator not only changes the height of the deformable mirror at that point, but also affects the height of the neighboring locations. A coupled approach is necessary to determine the forces applied to each of the actuators on a single-sheet deformable mirror.

4.3 Guide Stars

In order for a wavefront sensor to work, we must observe a known wavefront which experiences the aberrations that light from the science object also encounters. Knowledge of the wavefront distortion is based upon the image observed by the wavefront sensor and *a priori* knowledge of the shape of the incident wavefront before atmospheric distortion. By comparison of the observed wavefront with the expected (unaberrated) wavefront, the atmospheric density variations inducing the differences can be deduced.

Planar wavefronts constitute the simplest incident wavefront shape to deal with; for planar wavefronts the image at the wavefront sensor CCD is the diffraction pattern induced by the sampling of the wavefront sensor lenslet. This type of wavefront is what we would expect from distant point sources such as individual stars in the absence of atmospheric distortion. The limited size of stars ($\leq 10^6$ km) and their extreme distances ($\geq 5 \times 10^{12}$ km) make them excellent point sources for all but the largest and closest red giants. The wavefront radius of curvature from a star is approximately the distance to the star, which makes it effectively planar.

However, astronomers do not usually find images of individual stars very interesting; rather they generally wish to have an image produced of all of the sources over a given solid angular field of view. Each point of light from that field of view contributes its own planar wavefronts propagating at an angle with respect to the planar wavefronts from each of the other luminous points, and these are very difficult to distinguish from one another at the wavefront sensor. Hence, wavefront sensing is difficult to perform using extended sources as guide stars.

To overcome this difficulty, most AO observations make use of a 'guide star'. This is a bright source close (in angle) to the object we wish to study (typically called the 'science object'). There are two types of guide stars used in adaptive optics: natural guide stars and artificial laser guide stars.

4.3.1 Natural Guide Stars

When a star exists close to the science object, it can be used as the source of light for the wavefront sensor. Light from this star traverses nearly the same path through the atmosphere as light from the science object, and thus experiences nearly the same atmospheric effects. By correcting the observed wavefront of the guide star, light from the science object is corrected as well. This technique works well, resulting in significant improvement in images of planets [90] [91], clusters [13] [101], and other extended sources [72] [19] [57]. However, because of the requirement for a bright star near the science object, natural guide star AO is limited in its application to observations of only a small fraction of the sky, as we will see below.

The standard method for determining the effectiveness of an AO system is to compare the Strehl ratio with and without adaptive optics. The Strehl ratio is the ratio of the peak intensity of an observed point source to the peak intensity of a perfectly imaged point source (an Airy pattern for most circularly symmetric systems). The common approximation of the Strehl ratio S , applicable for Strehl ratios of $S \geq 0.1$ [113] is

$$S = e^{-\sigma^2} \quad (4.1)$$

where σ is the mean induced phase error in radians. These values of σ , or more properly the wavefront phase variance σ^2 are standard figures of merit by which adaptive optics systems are measured and compared.

Guide Star Brightness Effects The radiant intensity of the guide star has a direct effect on the efficacy of the AO system. The ability of the wavefront sensor to measure the tilt of the wavefront across a subaperture depends on its ability to accurately ratio the energy falling on the pixels of the CCD. Thus, the error in the tilt estimation is a function of the noise in the signal (typically read noise, photon noise and shot noise). The read noise is usually a fixed amount per detector read event, and will

dominate the signal-to-noise ratio of the wavefront sensor at low fluxes. Both of the latter noise sources, being discrete events, are Poisson-distributed processes and thus are proportional to the square root of the incident flux. As a result, at higher fluxes where photon noise or shot noise dominate the noise spectrum, the signal-to-noise ratio improves as the square root of the incident flux. Thus, we can expect the total sensor noise expressed in wavefront variance to be the sum of the individual variances. The derived wavefront phase variance as a function of the number of photons detected N is [92]

$$\sigma_{noise}^2 = \frac{\pi^2 \theta^2}{N} \left(1 + \frac{4n_e^2}{N} \right) \left(\frac{\lambda}{D} \right)^2 \quad (4.2)$$

where θ is the angular extent of the guide star image and n_e is the number of noise electrons and/or noise from background photons per integration period.

Isoplanatic Angle As alluded to above, one of the criteria for a natural star to serve as a guide star is that it be close enough in angle to the science object that light from the guide star traverses largely the same path as light from the science object. As the angle between the guide star and the science object increases, the efficacy of the correction diminishes. The angle over which the correlation between the sampled wavefront from the guide star and the wavefront from the science object is high is called the ‘isoplanatic angle’. The errors associated with the angular separation of these two sources have been derived:

$$\sigma_{tilt}^2 = \left(\frac{\theta}{\theta_0} \right)^{5/3} \quad (4.3)$$

where the isoplanatic angle θ_0 can be approximated as

$$\theta_0 \approx 0.6 \frac{r_0}{L} \quad (4.4)$$

where L is the height of the turbulence layer, and r_0 is the Fried length for the site at the time of observation. Clearly, as the angle begins to exceed the isoplanatic angle, the uncorrected wavefront errors increase rapidly and the Strehl ratio drops rapidly as seen in Figure 4.1.

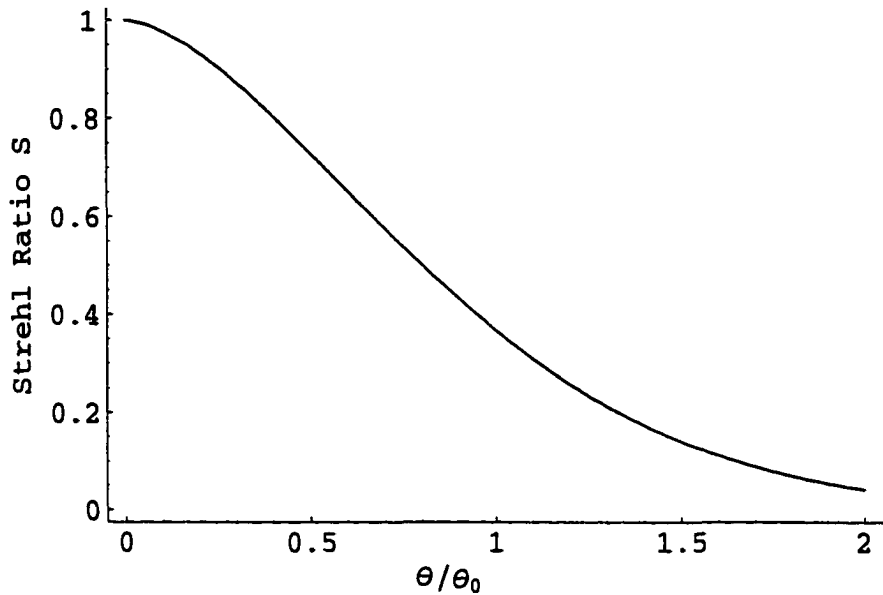


FIGURE 4.1. The Strehl ratio resulting from angles exceeding the isoplanatic angle for a given site. Fairly good imaging is produced for angles less than θ_0 , but degradation is rapid for higher angles.

4.3.2 Temporal Correlation

The dynamic nature of the atmospheric distortion implies that any wavefront we measure and correction that we subsequently apply are appropriate for a short time at best. The longer the process of measuring, analyzing and correcting takes, the less correlation there is between the measured wavefront and the corrected wavefront, and hence, the less effective the applied corrections will be. We can analyze this as a temporal error which will adversely affect the wavefront. The wavefront variance is

$$\sigma_{temp}^2 = 0.031 \left(\frac{t}{t_0} \right)^{5/3} \quad (4.5)$$

where t is time since the measurement and t_0 is the so-called Greenwood time delay [92]. This time delay is a function of the wind speed \bar{v} and Fried length r_0 , and is given by Roddier [92] as

$$t_0 = 0.314 \frac{r_0}{\bar{v}}. \quad (4.6)$$

Thus, there is an optimum correction frequency for adaptive optics, which is dependent on the brightness of the guide star and the wind velocity at the telescope. Operating the AO system at a high rate reduces the temporal decorrelation, but allows less time to integrate light from the guide star such that photon noise drives up the measurement error. Integrating for longer periods reduces this noise, but with a concomitant increase in the temporal noise shown here.

4.4 Artificial Guide Stars

Full sky coverage with adaptive optics cannot be performed using natural guide stars. There are just not enough bright stars, nor are they evenly distributed as guide star sources [59] [60]. Another source of light must be found or created to measure the spatial structure function of the atmosphere. The source must be bright enough to overcome the wavefront sensor noise, and must be 'positionable' (*i.e.* we must be able to place it 'next to' the particular science object we are interested in) and must be smaller in angular extent than the seeing-degraded telescope resolution. The source must be above any turbulence in order to measure it, and in theory should be in a fixed position above the atmosphere to keep global tilt from affecting the apparent star positions. Furthermore, it must not interfere with our observations, and should not contribute significantly to the sky background. Finally, for aesthetic and political purposes, it is desirable to have a source which is not visible to the unaided eyes of the public at large.

The only reasonable, viable candidate for meeting these requirements is to direct a relatively well-collimated laser beam on the sky in the direction of the science object. Scattering of this intense, collimated beam can then be used as the probe light for measuring the atmospheric structure function. The laser can be focussed rather narrowly to produce sources with small apparent spots (though there must be a focus correction applied to the wavefront sensing camera in most cases). With a

sufficiently bright laser, or sufficiently strong scattering, most of the aforementioned requirements can be met with a laser guide star system. However, there are a few additional problems to be overcome with using such a guide star.

4.4.1 Focal Anisoplanatism: The Cone Effect

In the natural guide star case, the extreme distances of the guide stars is represented by planar wavefronts, or alternately, by columns of parallel rays incident on the telescope entrance pupil. Likewise, the rays from the science object are comprised of similar columns of rays. The extent to which these two columns overlap in the turbulent layers determines the extent to which the turbulence in the layer is correctable. With artificial guide stars, the finite distance of the guide star (≤ 100 km) causes the rays to form a cone with a length that corresponds to the height of the guide star, and a base that corresponds to the area of the telescope entrance pupil. For turbulent layers that are much lower than the guide star, the sampling of the atmosphere from the artificial guide star approximates the atmosphere through which the light from the science object travels. However, the approximation is less and less valid as the height of the turbulent layer increases, or as the height of the guide star decreases. This effect, known as 'focal anisoplanatism' or the 'cone effect' comprises a major limitation to the usefulness of particular types of guide stars.

To a great extent, the cone effect is expected to be effectively eliminated in the future by application of multiple guide stars which individually sample the atmosphere above different portions of the telescope entrance pupil. However, multiple guide stars and the 'stitching algorithms' needed to effectively analyze partially-overlapping turbulence samples are still a number of years off.

4.4.2 Global Tilt

The second error induced by transitioning from natural guide stars to artificial guide stars is the 'global tilt' error. As the laser is projected through the atmosphere, the beam is subject to refraction from the minor thermal and pressure gradients that we are actually trying to measure. As long as the beam diameter is smaller than the turbulent cell size (effectively r_0) the beam will not be broken into multiple spots on the sky. However, the single laser spot will appear to wander about the fixed background of the stars, as the atmospheric cells through which the beam propagates vary.

Correcting for this requires that we continue to track an external star, similar to observing a natural guide star. The location of the natural star is used to determine the direction and amount of 'wander' induced in the laser guide star beam. The requirements on the system for correcting the global tilt are much less stringent than those for performing higher order corrections, so a much fainter natural star can be used. Detailed analysis [59] [60] shows that using these faint natural 'tilt' stars and a laser guide star of a few Watts, Strehl ratios of greater than 0.25 should be achievable over more than half of the total sky, dramatically increasing the potential for adaptive optics.

4.4.3 Scattering Mechanisms

So far, we have considered a generic guide star laser, and have not discussed power requirements, spectral requirements or temporal pulse formats. These last three factors all play a major role in the choice of the laser, and types of adaptive optical systems which can be used.

The type of artificial guide star AO system to be implemented depends on the scattering mechanism which the wavefront sensor will observe. There are two relevant types of scattering to be considered, Rayleigh Scattering and Resonance Scattering.

Rayleigh Scattering In 1871 Lord Rayleigh devised a theory of the scattering of sunlight based on small molecular oscillators. Using dimensional arguments, he correctly deduced that the energy scattering probability had to be proportional to $1/\lambda^4$ [42]. Though the derivation of the details of the scattering coefficients would require the Quantum Theory of Planck, Rayleigh's theory accurately (if qualitatively) explained the commonplace observations of blue skies and red sunsets.

For the mostly-diatomic atmospheric gas constituents (N_2 and O_2) the molecular oscillation resonances are in the ultraviolet region of the spectrum. In the visible portion of the spectrum, the nearer to the UV resonance, the higher the scattering probability. Hence, blue is scattered much more strongly than green, which is scattered more than yellow, etc. A simple model of Rayleigh scattering is developed in Appendix B.

To be useful as guide star lasers, Rayleigh beacons generally must be pulsed, and the returned light must be gated to generate effective point sources. Furthermore, Rayleigh scattering drops off rapidly with altitude, providing bright scattering sources mainly for low altitude portions of the beacon. As a result, the cone effect is a major problem that must be overcome when using Rayleigh beacons.

Rayleigh beacons have some significant advantages, principally related to the easing of restrictions on guide star laser development. High energy, pulsed laser systems with good beam quality are commercially available, generally at reasonable prices. There is no requirement to maintain a specific wavelength, or spectral distribution. Finally, the nature of Rayleigh scattering drives the system toward the ultraviolet, where the beacons produced are not visible to the public, and do not contribute to the background in the bands of interest to ground-based astronomers.

Resonance Scattering Lidar measurements of the upper atmosphere have identified a region of the mesosphere in which atomic sodium (Na) is relatively abundant. This region is typically about 5 km in thickness (FWHM), and usually centered at about 90-

95 km altitude. Sodium happens to have a very high oscillator strength, which means that it can readily absorb and re-emit light of the right wavelength. This absorption-emission process is known as resonance scattering. While the absorption profile of a single atom is very narrow (about 10 MHz) the thermal velocity distribution of the sodium atoms shifts the resonance frequency for individual atoms in the rest frame of the observer, resulting in a much broader (about 3 GHz) continuous spectral resonance profile. We deal with the process of resonance scattering in much more detail in the chapter on guide star laser requirements, Chapter 5.

Guide star lasers based on the resonance scattering of sodium are much more difficult to develop, because such lasers have to maintain a particular frequency, and at high power, ideally should cover the entire Doppler-broadened distribution. However, there are some significant advantages to the use of these lasers over Rayleigh beacons. First and foremost, the height of the sodium spot significantly reduces the focal anisoplanatism from that of Rayleigh beacons. Furthermore, the height of the beacon also means there is much less focal correction to be applied in observing the science object. Finally, the spot produced is localized in the mesosphere, removing the requirement that the laser be pulsed and the return be gated. In other words, the guide star can operate continuously.

Chapter 5

GUIDE STAR LASER REQUIREMENTS

For the sodium layer to blaze
With a guide star which shines where we gaze,
We need feedback and gain,
And with legerdemain
We can cause our contraption to lase!

-WTR

To wring as much brightness as possible from the available atoms in the mesospheric sodium layer, it is necessary to understand the sodium atom, especially in the environment in which it exists. We will therefore concentrate on the physics of the sodium atom, followed by its characteristics in the rather cold, rarified conditions of the mesosphere. Next, we will consider the interactions of sodium atoms with the electric field of an optical wave using a semiclassical approach. The chapter concludes with the implications of various optical pumping schemes which help us understand the returns we can expect from different types of lasers.

5.1 The Sodium Atom

Sodium (Na) is a naturally occurring element with atomic number 11, consisting almost entirely of one isotope with a mass of 23 atomic mass units (amu). In its lowest energy state, its electronic structure has fully filled $1s^2$ (2 electrons), $2s^2$ (2 electrons) and $2p^6$ (6 electrons) shells, complemented by a single $3s$ valence electron. Thus, sodium sits at the far left side of the periodic table, among the group 1 alkali metals.

With filled inner shells, the non-valence electrons have very little opportunity to interact with other atoms; however, the lone valence electron is capable of strong interactions, resulting in a volatile hydrogen-like atom. This electron, being least strongly bound to the atom by the Coulomb force, is the prime candidate for optical excitation.

Interaction of low-intensity light and matter is generally an electronic interaction in which an atom absorbs energy from, and emits energy to the electromagnetic field. This process occurs in discrete quanta of the electromagnetic field known as 'photons' and at discrete units of energy associated with each photon. In this quantum description of light-matter interaction, the atom stores the absorbed energy by elevating one of its electrons to a more energetic allowed state. The reverse process also occurs, in which the atom with an energized electron emits this energy to the electromagnetic field.

The most important value associated with the calculation of the energy of an atomic transition is the principal quantum number n , which serves to differentiate among the different eigenvalues and eigenstates that are solutions to the time-independent Schrödinger equation, $\hat{H}\Psi_n = E_n\Psi_n$. In the case of sodium, the valence electron is in the ground state for $n = 3$, so the lowest transition involving the principal quantum number n would be to the $n = 4$ state. This does not, however, represent the lowest energy transition available. Within a single shell (given by a particular principal quantum number n) there are subshells involving different magnitudes of orbital angular momentum. These subshells are designated according to the orbital angular momentum quantum number l which can take on discrete integer values from $l \in 0 \dots n$. Likewise, the orientation of the orbital angular momentum is quantized such that its projection on a particular axis takes on discrete values $m_l\hbar$ which have nominally identical (degenerate) energy eigenvalues. There are $2l + 1$ such orientations, running in integer values from $m_l \in -l \dots +l$. Because of the splitting of this degeneracy when atoms are placed in a magnetic field, the m_l are often referred to

as the magnetic angular momentum quantum numbers. Each electron also has an intrinsic spin s of magnitude $\frac{1}{2}\hbar$. The orientation of this spin, similar to the orientation of the m_l , is quantized according to discrete half-integer values m_s , and can take on values of $\pm\frac{1}{2}\hbar$. Finally, the orbital angular momentum and spin angular momentum of an electron interact resulting in different energy values when these angular momenta are aligned parallel or antiparallel. We designate this spin-orbit coupling (or L-S coupling) and identify its value according to the quantized value $j = l + s$, where j runs from $|l - s|$ to $|l + s|$. The different states of electrons are designated according to 'terms' which follow the convention $n^{2s+1}l_j$. Thus, for the valence electron of a sodium atom in its ground state, with l antiparallel to s , we designate it as $3^2s_{\frac{1}{2}}$.

Transitions of the optically-active electron among the various available states are governed by the transition rules: $\Delta l = \pm 1$ and $\Delta m_l \in 0, \pm 1$ [58]. The first of these rules is a quantum statement of conservation of angular momentum. Since photons have an angular momentum quantum number of $l = 1$, then for the system to conserve angular momentum the atomic transition must enforce a change in the angular momentum of the atom by an equal and opposite amount, -1 . Thus under the stated selection rule, in moving up from the $3s$ ground state ($l = 0$), a single transition must take the system to a p state ($l = 1$) such as $3p$ or $4p$. From a p state, the atom can then transition to either an s state or a d state ($l = 2$), but not to another p state for which $\Delta l = 0$, nor an f state for which $\Delta l = 2$. Thus, we see that from the $3^2s_{1/2}$ ground state, the atom is limited to the $3^2p_{1/2}$ and $3^2p_{3/2}$ transitions in the visible. The next transition to the 4^2p levels occurs at about 2853 \AA in the ultraviolet [3]. This accounts for the fact that few visible lines other than the D_2 lines are seen in the spectrum of sodium, and they are very faint when observed. All other visible lines must result from transitions to and from states other than the ground state, and these are not well populated.

The second quantum selection rule, $\Delta m_l \in 0, \pm 1$, limits the number of available transitions to degenerate states. Without external influences (and for the moment

neglecting spin-orbit interactions), the energies of the optically active electron within a subshell are identical; the m_l values simply serve to identify different spatial orientations of the electron wavefunction that all belong to the same energy eigenvalue. However, the optically-active electron also has an intrinsic spin quantum number with a value of $\frac{1}{2}$, and magnetic spin quantum number of $m_s \in \pm\frac{1}{2}$. The angular momenta of the orbital and spin properties of the atomic system interact, and in such circumstances it is necessary to consider the combined total angular momentum $j = l + s$ and total magnetic quantum number m_j which ranges from $-j$ to j in integral steps. One would anticipate that the energies associated with states in which the magnetic quantum numbers are aligned would be higher than those with states that are opposed, and this is indeed the case. This spin-orbit interaction (or L-S coupling, or Russel-Saunders coupling) accounts for the dominant feature of the $3S \rightarrow 3P$ transition, the separation of the line into the familiar D_1 and D_2 lines of the sodium spectrum. The D_1 line results from the transition $3S_{\frac{1}{2}} \rightarrow 3P_{\frac{1}{2}}$ at 589.593 nm, whereas the D_2 line at 588.995 nm is the result of the $3S_{\frac{1}{2}} \rightarrow 3P_{\frac{3}{2}}$ transition.

A more exact accounting of the energy levels of the sodium atom reveals the so-called hyperfine structure, which results from the electron-nucleus spin-orbit interaction. This in general is the result of aligned and anti-aligned configurations of the electrons' total angular momentum J and the nucleus' total angular momentum I . The resultant total angular momentum for the atomic system is usually designated F , where $F = J + I$. With a nuclear angular momentum of $I = \frac{3}{2}$, and a ground state angular momentum of $J = j = \frac{1}{2}$, the ground states available to the sodium atom correspond to $F = 1$ and $F = 2$ in which the angular momentum vectors are opposed and aligned, respectively. The energy separation of these two states is 1.77 GHz [3], which accounts for the double-humped distribution of energy in the sodium D lines. A similar type of splitting of energy levels into $F = 1$ and $F = 2$ levels occurs for the first excited state with $j = \frac{1}{2}$, the $3P_{\frac{1}{2}}$ state. However the magnitude of the splitting is only 188.6 MHz, nearly an order of magnitude smaller. For the excited

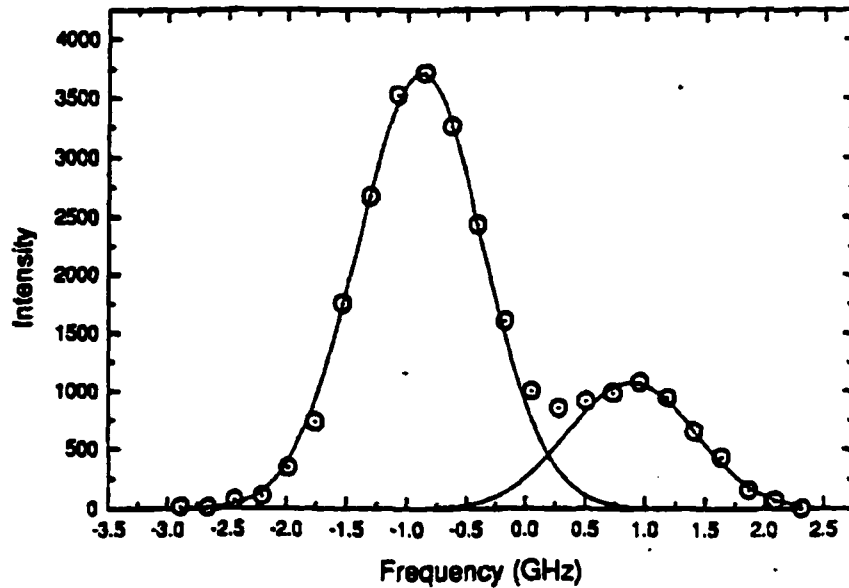


FIGURE 5.1. Spectral response of the mesospheric sodium layer at the MMT for circularly polarized incident radiation. Circular polarization drives the excited atoms to a state in which the second selection rule mandates that they decay to the $F = 2$ level, thereby enhancing the return of that peak over the peak associated with decay to $F = 1$.

level $3P_{\frac{3}{2}}$, the F values range from $0 \rightarrow 3$, separated by a total of 109.3 MHz. Since there are twice as many levels to this transition, we would expect a higher probability of interaction. This gives rise to the observation that the D_2 line is normally twice the brightness of the D_1 line. Analysis of the degenerate states of the two F levels of the ground state reveal that for $F = 1$, then $m_F \in -1, 0, 1$, whereas for the $F = 2$ level, $m_F \in -2, -1, 0, 1, 2$, so that under identical circumstances we would expect the $F = 2$ peak to be about $5/3$ the height of the $F = 1$ peak. This was verified *in situ* by Jacobsen, *et al.* [45], as shown in Figure 5.1.

The lifetime of the sodium atom in the excited 3^2p state is reported to be $\tau_0 = 16$ nsec [70], and it has two very significant consequences for guide star laser development. First, the lifetime determines the rate at which decay from the excited state occurs,

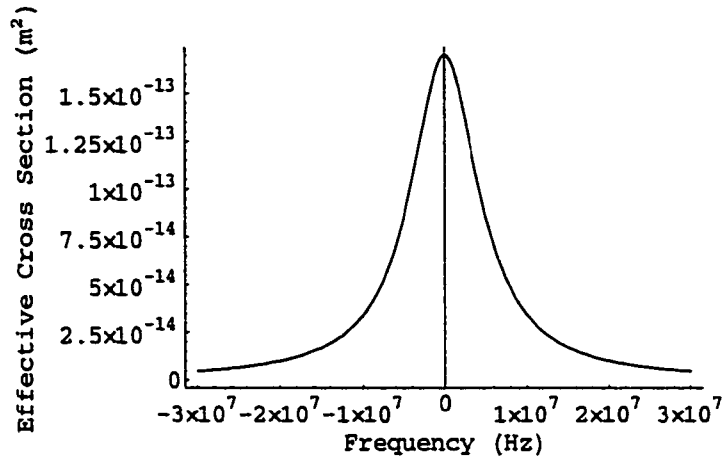


FIGURE 5.2. The effective cross-section of an individual atom is reduced as the stimulating radiation is shifted from the resonant frequency. The result is a Lorentz absorption profile. Here we see the effective cross-section of a single Na atom to stimulating radiation offset from the resonance frequency (Hz).

and thus, along with the absorption cross-section, determines the saturation intensity of the sodium layer. Second, the lifetime broadening dictates the spectral width of a 'velocity class', which determines the number of atoms which can be excited within a given narrow spectral band. It thus determines the brightness of the resulting guide star.

The spectral cross-section of a given sodium atom in the two-level atom model can be derived from the small-signal spectral absorption coefficient $\alpha_0(\nu)$ [98]

$$\sigma_0(\nu) = \alpha_0(\nu)/N \quad (5.1)$$

$$= h\nu \frac{\rho^2}{nc\epsilon_0 h^2} \frac{\gamma}{(\nu_0 - \nu)^2 + \gamma^2} \quad (5.2)$$

a Lorentz function, where γ is the upper level spontaneous decay rate, ρ is the dipole transition matrix element for our two-level atom, and ν and ν_0 are the exciting and resonance frequencies, respectively. The results, normalized to the observed absorption cross section is shown in Figure 5.2.

Derivation of the lifetime broadening of the transition [100] based on this lifetime results in a FWHM line width of

$$\Delta\nu = \frac{1}{2\pi\tau_0} \quad (5.3)$$

$$= 10MHz \quad (5.4)$$

which is represented in Figure 5.2. We can interpret this as an absorption probability function, where the probability that a single sodium atom in a 1 m^2 area will absorb a single photon incident at some point within that same area will be 1.7×10^{-13} if the photon energy is on resonance. Off resonance, the probability drops quickly.

5.2 Thermospheric Sodium

5.2.1 Height and Abundance

Within the earth's thermosphere there is a region of concentrated sodium atoms, with concentrations that usually peak at heights between 90 and 95 km[95][81]. This layer of sodium is thought to be deposited by meteors captured in the earth's gravitational field. This is the region in the atmosphere where considerable aerodynamic heating of falling bodies takes place, providing the opportunity for materials near the surfaces of meteors to be vaporized.

The density of the atmosphere at this altitude is approximately $7 \times 10^{19} \text{ m}^{-3}$ [2]. Through atmospheric LIDAR measurements, Papen *et al.* [95] has reported integrated column densities of approximately $4.3 \times 10^9 \text{ cm}^{-2}$, with layer thicknesses (RMS) of 4-5 km. Our own measurements in the region [36] resulted in an annual mean of $3.7 \times 10^9 \text{ atoms cm}^{-2}$ at Kitt peak and with ranges from 2×10^9 to $6 \times 10^9 \text{ atoms cm}^{-2}$ at Mt. Hopkins.

It is important to note that the column density is quite variable [38] [80] [36]. Average season-to-season variability appears to be a factor of about three, similar

to the nightly variability. The abundance is reported to be higher during the winter months, though the data reported by Ge [36] do not necessarily bear this out.

5.2.2 Sodium Temperature and Doppler Broadening

The mesospheric sodium has been observed to be in local thermal equilibrium at a temperature of approximately 200K [70] [95]. At the low pressures of the atmosphere here, collision broadening and natural broadening of the sodium lines are negligible compared with the Doppler broadening of the thermal population.

Doppler broadening is the result of the motion of atoms in the direction of the laser radiation. An atom moving toward the laser source will have its resonance energy blue-shifted somewhat, while an atom moving away will experience a red-shift. The Doppler-shifted spectrum of a single perfectly narrow resonant line is given by

$$D(\nu - \nu_0) = \frac{1}{\sqrt{2\pi}(\delta\nu)^2} \exp\left(-\frac{(\nu - \nu_0)^2}{2(\delta\nu)^2}\right) \quad (5.5)$$

where $\delta\nu$ is the FWHM of the distribution, given by

$$\delta\nu = \nu\sqrt{2\ln 2}\sqrt{\frac{kT}{Mc^2}}. \quad (5.6)$$

In this last equation, k is Boltzmann's constant, T is the temperature of the sodium atoms, M is the sodium mass and c is the speed of light.

At the thermal velocity of sodium atoms in a gas, this shift can be appreciable. The broadened line of a 200 K distribution of sodium atoms about the $F=2$ ground state peak of sodium is shown in Figure 5.2.2. Here we show the number of atoms that are available per unit frequency of the stimulating radiation, normalized to the total column density of atoms of $4.3 \times 10^9 \text{cm}^{-2}$.

Because the width of the inhomogeneous Doppler broadening exceeds that of the natural broadening by over two orders of magnitude, dominates the profile and

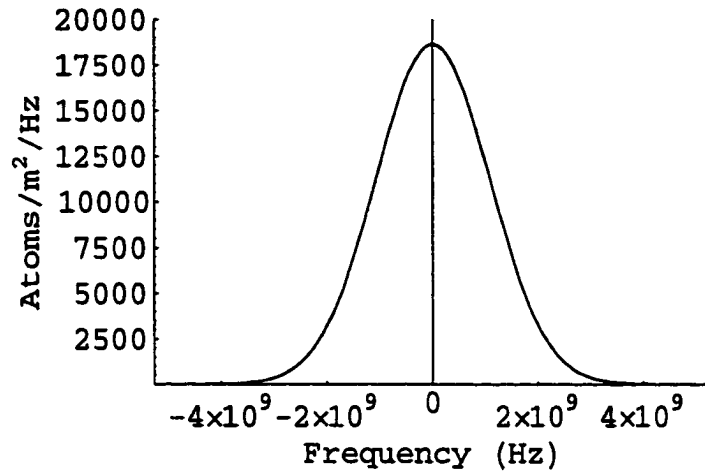


FIGURE 5.3. Spectral distribution of a Doppler broadened spectrum of Na atoms. The atoms are assumed to be in thermal equilibrium with a temperature of 200 K. The number of atoms within a 1 Hz band is displayed along the y axis, while the offset frequency (Hz) is displayed along the x axis.

characteristics of the mesospheric sodium layer. This will play a major role in selection of various pulse formats for guide star lasers, and ultimately in selection of the lasers themselves.

5.3 Sodium Saturation

Without any radiation, all of the mesospheric sodium atoms may be assumed to be in the ground state, so the so-called 'small-signal' absorption coefficient $\alpha_0(\nu)$ to a single photon of frequency ν is

$$\alpha_0(\nu) = \sigma(\nu)Nl \quad (5.7)$$

where N is the number density of absorbers and l is the length of the interaction distance. For this number density, one must consider that the effect of Doppler broadening drastically reduces the total number of atoms available to be excited at

any given frequency ν . The total number of atoms within spectral excitation range, integrated through the length of the sodium layer was presented in Figure 5.2.2. For a laser with an infinitely narrow spectrum operating at the peak of the Doppler-broadened distribution, this integrated number density is about 18000 available atoms per Hz of frequency. Since the broadening $\Delta\nu$ of a single atom is 10^7 Hz, and its absorption cross-section at line center is $\sigma(\nu) = 1.7 \times 10^{-13}$ m², the small-signal absorption probability that results is only 3.0%. Without considering polarization effects, this is the highest efficiency that we can hope for from the guide star laser.

As the incident power increases, there is no longer an infinitesimal number of atoms in the excited state, so the effects of saturation begin to manifest themselves. In this case, we must consider the reduced number of atoms in the ground state which can absorb the incident light, and the increased number of atoms in the upper state which can be stimulated to emit, effectively a process of anti-absorption. If the ground and excited states are labeled a and b with number densities N_a and N_b , respectively, then the general absorption coefficient is given by

$$\alpha(\nu) = \sigma(\nu)(N_a - N_b)l. \quad (5.8)$$

We can establish a saturation intensity I_{sat} which is the intensity at which the absorption coefficient has dropped to half of the initial (small signal) absorption. Using this value, the absorption function can be written

$$\alpha(I) = \frac{\alpha_0}{1 + I/I_{sat}}. \quad (5.9)$$

At low laser intensities the absorption coefficient is essentially the small-signal absorption coefficient, and absorption of the guide star laser is at a maximum (for steady state excitation). As the guide star laser intensity is increased, the absorption of the sodium layer is 'bleached', resulting in less efficient absorption. This elucidates one of the difficulties of artificial guide star generation: the brightness of the guide star is linearly dependent on the number of atoms in the upper state N_b , but to increase

the number of atoms in this state requires more and more power, most of which is wasted through induced transparency of the sodium layer.

From information already introduced, we can easily derive the saturation intensity for specific circumstances. Since the absorption function is half of the small-signal absorption coefficient at the saturation intensity, this then implies that $N_a - N_b$ must be half of N . With $N = N_a + N_b$, then

$$N_b = N - N_a \quad (5.10)$$

$$= N - (N_b + N/2) \quad (5.11)$$

$$= N/4. \quad (5.12)$$

At saturation intensity I_{sat} , the decay rate from the excited state must be

$$\frac{dN_b}{dt} = -\frac{N_b}{\tau_0} - I_{sat}N_b\sigma + I_{sat}N_a\sigma \quad (5.13)$$

in which the first term on the right of the equal sign is the spontaneous emission from the excited state, the second term is the stimulated emission, and the final term is the excitation from the ground state to the excited state. In steady state, $\frac{dN_b}{dt} = 0$, so the resulting solution is

$$I_{sat} = \frac{1}{2\sigma(\nu)\tau_0}. \quad (5.14)$$

With the stated lifetime of 16 nsec and the line-center absorption cross section of $1.7 \times 10^{-13} \text{m}^2$, the line-center saturation intensity is roughly 62 W/m²/sec. At this intensity, the absorption coefficient of the sodium layer is half that of the small signal absorption coefficient, or 1.5%.

5.4 Implications for Guide star Lasers

In general we want the brightest possible guide star we can attain in a given spot of the sodium layer, and that implies avoiding the inefficiency of sodium saturation as

much as possible. Avoiding this saturation can be done in two ways: by increasing the duty cycle of the laser, and optimizing the spectral output of the laser. We deal with each individually here, though in the end, they are often related by Fourier transform; *i.e.* the minimum spectral width is related to the temporal extent of the pulse.

5.4.1 Temporal Considerations

To first order, saturation of the sodium layer is directly dependent on the intensity of the stimulating radiation, not the average power. However, we ultimately care about the power absorbed by the sodium layer. Thus it is in our interest to increase the 'duty cycle' (the ratio of time during which the laser is radiating to the cycle time) as much as possible. In this case, a CW laser with a duty cycle of unity will result in the least amount of saturation, and the greatest efficiency for guide star brightness. This is one of the reasons that the most successful guide star lasers to date have been CW dye lasers.

Unfortunately, this does not bode well for development of solid state lasers based on nonlinear optical frequency conversion techniques. These techniques by definition rely on the nonlinear properties of certain materials that are observable only at very high intensity levels. The preferred way of achieving these high intensities is to concentrate all of the power into short pulses. This is exactly what we wish to avoid in the final output laser. The only other practical method of achieving high intensity in the nonlinear laser elements is to recirculate the lasing power many times in a high finesse cavity, but this is much less common and much more sensitive to minor losses.

There are a few temporal methods of increasing the peak intensity for nonlinear conversion: Q-switching, mode-locking and cavity-dumping. Of these, the most common is Q-switching which uses the lifetime of the gain material to store large amounts of energy. For Nd:YAG, by far the most common high-power solid state

laser, Q-switched pulses are typically around 10 nsec long, and rep rates of 10-50 kHz are possible. From this we can estimate an upper limit to the effectiveness of the laser. Assuming we obtain 10 W of average power at 50 kHz, then each 10 nsec pulse has a peak power of 20 kW. If this power is focussed into a diffraction limited spot of area 0.3 m^2 , then the intensity is roughly 1000 times the saturation intensity. We would thus expect roughly half of the atoms in the velocity class ($10^4 \text{ atoms/m}^2/\text{Hz} \times 10^7 \text{ Hz} \times 0.3 \text{ m}^2$) or 3×10^{10} atoms each to absorb a photon, for a total absorbed energy per pulse of 10^{-8} J. The average absorbed power would thus be 0.5 mW, about a factor of 200 less than that obtained with a 3 W CW dye laser. This is clearly not a viable guide star laser.

Though the duty cycle of Q-switched lasers puts them at a significant disadvantage, they are not necessarily beyond consideration. Short pulses at comparatively low repetition rates offers the opportunity for using multiple temporally interleaved lasers. Such lasers could be fired sequentially, and mechanical systems of rotating mirrors or electro-optical systems of polarization combining by using Pockel cells could be used to align the beams. The sequencing electronics and beam combining optics make the system more complex and, as is often the case, with complexity comes risk. Also, the individual lasers would have to be inexpensive enough to make up for the low duty cycle.

Nevertheless, this concept has a number of advantages which may make it attractive enough to attempt. First, since the individual pulses have already been shown to be well above the saturation level, each of the individual lasers can be operated at a relatively low power, altogether avoiding the problems of thermal lensing, thermal damage, and heat dissipation inherent in high power laser systems. Second, at low power each of the individual lasers can be made much less expensive by using standard laser rods, end pumped by single-stripe diode lasers. The simplicity and redundancy of the design allows for limited supplies of all laser parts to be kept on hand for repair and replacement at low cost. Finally, the redundancy of the system

provides robustness in which failure of one or two of the independent lasers does not significantly hinder the ability of the laser to produce a guide star. The conceptual design of a simple, yet elegant system based on Q-switched intracavity Raman lasers is presented in the concluding chapters.

Mode locking is another way of increasing the intensity of the beam for non-linear conversion, but maintains a rep rate that is many orders of magnitude higher than Q-switching. The pulses obtained from mode locking have a width that is determined by the transform-broadening of the gain width of the laser, and a rep rate determined by the round-trip cavity length. With mode locking, pulses of about 20 psec are common, while pulse repetition frequencies of about 100 MHz are normal[53]. These values indicate duty cycles in the range of 0.1 to 1.0%, significantly higher than the duty cycle associated with Q-switching. The drawback to this is that this greatly reduces the intensity required for efficient nonlinear conversion. While this can be overcome by recirculating most of the power through sync-pumping until there is sufficient intracavity intensity to maintain high efficiency, it requires temporal and spatial overlapping of the pump and recirculating pulses over many orders, and is subject to frustration by even slight cavity losses. Another major drawback to the use of mode-locked lasers for guide star generation is that the transform broadening of the 20 psec mode-locked pulse is on the order of 20 GHz, over an order of magnitude larger than the desired 500 MHz-wide pulse. Without some kind of compensation, the vast majority of the laser energy would be wasted.

Generation of guide star pulses at 100 MHz frequencies opens up some interesting possibilities for guide star studies. At this rate the pulses would be generated faster than the excited sodium atoms can decay, resulting in effects which are expected to be similar to the combination of a CW laser and pulsed lasers [69] [71].

The final method of creating short, intense laser pulses is cavity dumping, in which the lasing energy is stored in the electromagnetic field of a high-Q cavity, and periodically released. Typical pulse widths of about 1 nsec can be created this way,

at repetition rates of up to several MHz [53]. This method of pulse generation may be the best compromise for guide star lasers, though it is the least common of the various pulse generation techniques. The duty cycle is high enough (0.1-1.0%) to generate reasonably bright stars, while the pulse width is properly transform-broadened (500 MHz) to match the width of the peak of the mesospheric sodium line.

The problem associated with using cavity dumping is that the field intensity attains high levels within the cavity for pulses of any appreciable power and all elements within the cavity must be capable of withstanding these intensities virtually continuously. Furthermore, the intensity buildup will be limited at some point by cavity losses such as diffraction, surface scattering or mirror leakage which constrains the power to relatively low levels [63].

In conclusion, the saturation characteristics of the sodium layer complicate the problem for the application of solid-state laser systems. Commonly used nonlinear methods of frequency conversion cannot be blindly applied with respect to creating an effective guide star laser. However difficult these problems are, they are not insurmountable. Cavity-dumped and interleaved Q-switched systems are particularly interesting in their application to the problem, both showing potential for reasonably efficient, bright guide star returns.

5.4.2 Spectral Considerations

Another way of avoiding saturation of the sodium layer is to spread the laser energy into a spectrum significantly broader than the 10 MHz natural linewidth of sodium. At low power, concentration of the energy into a single velocity class tuned to the sodium D₂ peak is advantageous because it allows for the concentration of the power at the peak of the sodium absorption. However, when the absorption begins to bleach, the neighboring velocity classes are still strongly absorbing, so spreading the energy into those velocity classes will continue to brighten the guide star. If the 63% of

the sodium atoms normally in the $F = 2$ state (in all velocity classes) could be made to absorb and emit continuously, they would absorb (and thus emit) a total of 1.7×10^{21} photons per second, or almost 600 W of power over a square meter of sky. Compared with the absorption saturation of 62 W/m^2 for narrow-line excitation, this demonstrates the potential of spectral broadening.

Broadening the spectrum too much, however, results in more inefficiency. With fewer atoms in the tail of the velocity distribution, there is little incentive to put significant amounts of power into these regions. With a total width of about 1 GHz, it is most advantageous for us to concentrate the energy into the central 500 MHz, avoiding the inefficient wings of the distribution. The potential also exists to excite the atoms in the $F = 1$ peak of the D_2 line, possibly with a second laser, but this is only advantageous after the center of the $F = 2$ peak has been saturated.

Fortunately, the nonlinear methods of frequency conversion we are considering add some spectral broadening to the laser output, as already discussed. This broadening can be controlled by controlling the finesse of the laser cavity and internal tuning elements.

The saturation value of 62 W/m^2 derived above was for a single velocity class of the Doppler-distributed sodium response. A Q-switched laser producing peak powers of $6 \times 10^4 \text{ W/m}^2$, would only have about 0.5 mW absorbed, as derived above. However, spreading this energy evenly into a band of 500 MHz (about 50 10 MHz velocity classes) would boost the absorbed power by a factor of about 25¹. Thus we can expect a bit more than 10 mW to be absorbed, which is still nearly an order of magnitude below our ideal dye laser. The low duty cycle of Q-switching continues to plague us. The combination of the interleaved Q-switched laser and spectral broadening begins to approach conditions in which the sodium guide star brightness can exceed the brightness of our ideal dye laser. By using 25 interleaved Q-switched lasers operating

¹the efficiency off-resonance drops because there are fewer atoms in the off-resonance velocity classes

at 10 kHz, each broadened to a spectral width of 500 MHz, we can access a total of $25 \times 10^7 \times 10^4$ atoms 250000 times each second for a total absorption of 6×10^{17} photons/sec/m², or 0.2 W. This is more than twice the power our absorbed from our hypothetical dye laser, and thus in the realm of interesting possibilities.

5.5 Review of Sodium Guide Star Lasers

Work in development of laser guide stars for military purposes has been ongoing for almost two decades, though most of that time the work was performed in secret [33]. The initial idea for a guide star came in 1981 from Julius Feinleib as he watched a LIDAR system probing the sky above the telescopes rimming the Haleakala crater in Maui. It wasn't long before the idea of resonant backscatter from the sodium layer occurred to Happer [41]. The early 80's saw experimentation by the military with both Rayleigh beacons and resonant sodium stars, confirming the rapidly developing theory of laser guide star adaptive optics and validating the approaches. Then, in 1985, Foy and Labeyrie [28] suggested Rayleigh and sodium beacons in the open literature, and the astronomy community began to get involved in laser guide star development.

During these last two decades, several sodium guide star lasers² have been developed and tested at telescopes. A summary of some of the most important work in the area is provided in Table 5.1. Specific findings of these research systems is mentioned in the following paragraphs.

There was significant effort at Lawrence Livermore National Laboratory in the early 1990's directed toward adaptation of their AVLIS laser technology to sodium guide star demonstration and production [4][5]. Their initial efforts projected a pump-pulsed dye laser of remarkable power (1100 W) into the skies above the Laboratory.

²Since almost all of my work has been directed toward development of a sodium guide star laser, we choose to focus on those types of lasers here to the exclusion of the work done in development of Rayleigh beacons.

System	Power(W)	GS Mag	$\Delta\nu$ (GHz)	Duty Cycle
LLNL	1300	5.1	3	.00083
Lick	20	7.0	1.5	.0017
ChAOS	5	9.3	1	.07
UA(Coherent)	2.7	9.85	NA	1
UA(LLNL)	1.7	10.4	$3 \times .01$	1
UA(Spectra)	1.2	12.5	NA	1

TABLE 5.1. Summary of Sodium Guide Star Lasers

The laser is a chain of copper-vapor lasers pumping a dye laser chain in a master-oscillator power-amplifier (MOPA) system. The laser emits pulses of 32 nsec duration at a repetition rate of 26,000/sec, resulting in a duty cycle of 0.083%. To extend the duty cycle of the system, a pulse stretcher was developed which each large pulse into a time-sequenced group of 16 pulses, but the system was never implemented. The output of the system has a spectral broadening of 3 GHz to cover the entire Doppler spectrum. In operation, this system produced a guide star with a magnitude of 5.2, bright enough to be visible to the naked eye. The high power of this laser easily saturated the sodium layer, and the high intensity led to bright excitation of the edges of the spot, generating a sodium guide star of 7 arc sec FWHM.

Soon thereafter, a project to place a 20 W dye laser on the 3 meter Shane telescope at the Lick Observatory began to produce results [79][62][34][30]. This was also a dye laser, pumped by fiber-coupled, frequency-doubled, flashlamp-pumped Nd:YAG lasers. It operates with 150 nsec pulses at 11 kHz, and is electro-optically phase modulated to broaden the lasing spectrum to 1.5 GHz. Though capable of operating above 18 W, normal operation is at 7 W because of the high-power degradation of the beam and associated poor quality of the generated sodium guide star. This reduction in power is reported to cause an improvement in the spot size from 2.97 arc sec to 1.74 arc sec [34]. Under different conditions, they claim to have generated laser spots of ≈ 2 arc sec with astronomical magnitude in the visible band of $m_V = 7.0$ [62].

The only solid-state lasers to be used in generating sodium guide stars are the sum-frequency lasers developed by Jeys at Lincoln Labs [46][96]. These lasers make use of the fortuitous combination of energy in the 1064 nm and 1319 nm lines of Nd:YAG, which when summed generate the 589 nm sodium wavelength. They use QCW laser diodes to pump Nd:YAG slabs which are synchronously mode-locked. The resulting pulses are of the 'macro-pulse-micro-pulse' format which ultimately generate power at a duty cycle of almost 7%. The macro-pulses are approximately 170 μ sec long, and are pulsed at 400 Hz. Because the mode-locking period of 10 nsec is shorter than the sodium relaxation time of 16 nsec, the laser is essentially CW within a single macro-pulse[71]. The most experience with these lasers has been obtained by the AO group at the University of Chicago. Though they claim output power of 8 W in the lab, the best they were able to obtain at the Dunn Solar Telescope was 5 W. Of this, only 1.1 W was projected on the sky, which resulted in guide stars of magnitude $m_V = 9.3 - 10.5$ using circular polarization. One advantage to this system is that the spot size was small, typically 1.3-1.5 arc sec, with a profile that was more sharply peaked than the profile of an actual star[96].

Researchers at the University of Arizona evaluated three CW dye laser systems at the Multiple Mirror Telescope (MMT) in southern Arizona in 1993-1994, and generated sodium guide stars with magnitudes from $m_V = 9.85 - 12.5$ over a period of nine months. Two of the lasers were commercial ring cavities, while the third was a standing-wave z-cavity from Lawrence Livermore National Laboratory. The output power, tuning stability and operational characteristics of the three lasers were significantly different, leading to the choice of a laser based on the design of a Coherent 899 ring dye laser for the MMT operations. These results demonstrated that much lower laser power could be used effectively to produce guide stars comparable to those of much higher power lasers by judicious and efficient use of tuning and duty cycle.

In addition, laboratory lasers have been developed for testing and demonstrating other concepts which hold promise to production of guide star lasers. In 1996, TRW

demonstrated the first Raman laser tuned to the sodium D₂ line. This laser used a 5 Hz long-pulse, 134 MHz mode-locked Nd:YAG laser to synchronously pump an intracavity-doubled Raman laser, based on the 912 cm⁻¹ Raman shift of CaWO₄. Their report claims a Raman conversion efficiency of 14.5%, but the average power output was not reported.

In 1998 Murray *et al.* [74] reported development of an intracavity Raman laser tuned to 1.178 μm and doubled to 589 nm. Their laser made use of a Q-switched Nd:YAG with an intracavity CaWO₄ Raman crystal which generated up to 480 mW in 6 nsec pulses when Q-switched at 10 kHz.

Since then, development has been limited. The Gemini project office put out a request for quotation for a guide star laser, but their requirements were so elaborate that the cost associated with the responses deemed technically qualified were well beyond their budget. Since then, they have awarded small development contracts to demonstrate the feasibility of some concepts, but an actual, new guide star laser has not been developed. Meanwhile, development of a large, complicated dye laser system for the Keck observatory similar to the Lick observatory laser is progressing. These lasers are very expensive though, both in development costs, equipment costs and operational costs. Off the cuff estimates for these systems are reported to be in the range of millions of dollars [29] but even this probably ignores the high development overhead costs associated with the program. Nevertheless, the Keck telescope is progressing with development of this system, demonstrating that the need for a powerful guide star laser has not diminished, and that the well-endowed AO systems are willing to pay dearly to have them.

Part III

Sodium Guide Star Laser Research

Chapter 6

DYE LASER DEVELOPMENT

6.1 Background

Because of its ability to produce some small amount of power at any desired wavelength within a broad continuous band, the dye laser has been a common source for producing a sodium guide star[45][39][32]. It can be tuned to the 589 nm D_2 transition of sodium, and can produce enough power (3 W) to excite a star of roughly 9th magnitude for use as a probe source in AO correction[45].

At the Multiple Mirror Telescope (MMT) we have been using a locally developed dye laser [88]. The gain medium in our dye laser is an organic dye, Rhodamine 6 G, which absorbs strongly in a broad band about 500 nm, and emits in a broad band centered at 590 nm. The dye molecules are carried in a liquid medium of 3 parts ammonyx (soap solution) and 1 part ethylene glycol. The mixture is cooled to near 0 C to minimize the thermal expansion of the dye which limits the pump intensity and also to reduce the tendency of the dye to foam. The cooled mixture is forced through a laminar-flow nozzle by a centrifugal dye pump which operates at pressures up to about 80 psi. The nozzle produces a 140 μm thick dye jet held at Brewster's angle near the concentric focus of the laser cavity. The original Z-cavity laser was developed based on a design from Lawrence Livermore National Labs [45], and was capable of generating 3 W of tuned power at the sodium D_2 resonance. However, cavities making use of a standing-wave resonator suffer from spatial hole burning, limiting the single longitudinal mode output power and causing the laser frequency to run multi-mode, which is less efficient for guide star generation.

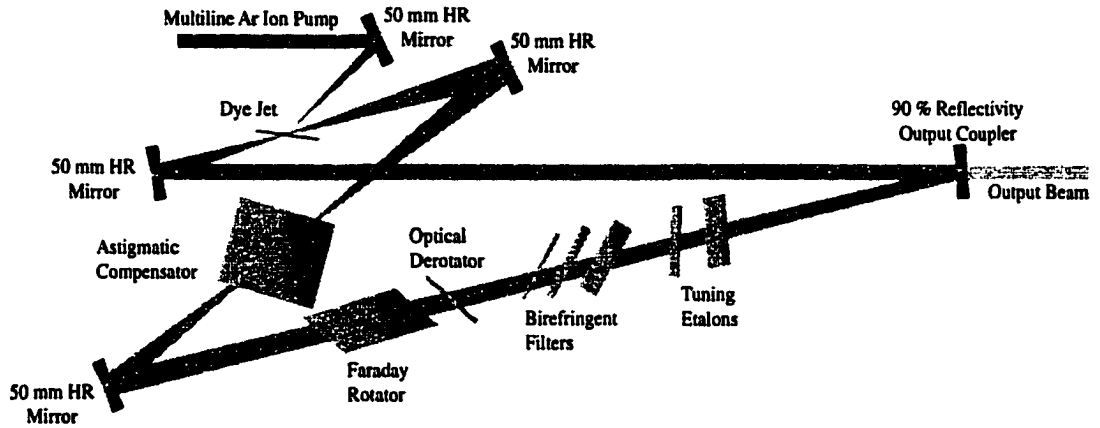


FIGURE 6.1. Ring dye laser layout.

6.2 Ring Laser Development

To counter the problems associated with the standing-wave cavity, we converted our laser cavity to a ring-cavity design, based on the 'bow tie' resonator in Figure 6.1. Ty Martinez did the initial design of this laser by developing a merit function in Zemax which would, among other things, recreate the same wavefront position and curvature on repeated transits of the cavity. The mirror angles were chosen to eliminate the system astigmatism (when the astigmatic compensator is inserted), and the distances were chosen to reproduce the initial Gaussian beam parameters using stock 50 mm laser mirrors. Finally, the dye jet and astigmatic compensator were constrained to be at Brewster's angle to minimize losses of the p-polarized cavity beam. This causes the output beam to be linearly polarized in the horizontal axis.

The laser is pumped with a continuous-wave 30 W argon ion laser. Pumping was initially performed using a side pumping mirror, bringing the pump beam in at an angle of 12 degrees with respect to the cavity beam.

Constraining the ring cavity to oscillate in one direction around the ring is necessary to concentrate the output power into a single direction. Otherwise, two output beams will result at the tilted output coupler. To achieve one-way oscillation we

made use of a Faraday rotator and optical derotator. The Faraday rotator has Brewster surfaces oriented to pass the P polarization losslessly. The glass comprising the rotator has a high Verdet constant, and a 4000 Gauss magnetic field is applied in the glass parallel to the beam propagation direction. This imparts a rotation of about 4 degrees to the polarization about the propagation axis. An equal amount of rotation results from the intrinsic optical activity of the thin quartz optical derotator element. For the quartz element, the direction of rotation is determined by the direction of propagation of the beam, whereas for the Faraday rotator, the direction of rotation is determined by the magnetic field. In this way, the wave propagating clockwise around the cavity first encounters the optical derotator which rotates the polarization by 4 degrees, and then encounters the Faraday rotator which counterrotates the polarization angle for a net zero rotation. A beam propagating counterclockwise encounters the Faraday rotator which rotates the polarization angle 4 degrees, and then encounters the optical derotator which rotates the polarization another 4 degrees *in the same direction* for a net rotation of 8 degrees. With the many Brewster surfaces in the cavity, the losses for the beam with a net rotation are much higher than the losses for the beam with no net rotation. The counterclockwise wave is therefore quickly quenched, making all of the power available to the clockwise rotating wave.

Tuning the ring laser to the sodium D_2 line is generally performed with the same tuning elements used in a typical standing-wave dye laser cavity; three birefringent filters situated at Brewster's angle successively narrow the lasing line. Rotation of the birefringent filters results in a wavelength dependent variable phase delay between the ordinary and extraordinary waves. At the far end of the crystal, the wavelengths for which these waves add constructively pass unattenuated, and thus are preferentially selected in the cavity. A succession of thicker birefringent filters is used to narrow the laser band to about 1.0 GHz. After that, uncoated fused silica etalons of thicknesses 2 mm and 5 mm are used to select a single collision-broadened lasing mode of about 10 MHz width. Spectral monitoring of the output beam is performed by directing

some of the light leaking through one of the cavity mirrors to an optical fiber which feeds an $R=700,000$ echelle spectrograph. For fine frequency resolution, some of this light can be directed into a Fabry-Perot interferometer with a finesse of 30.

The output beam quality of this laser, while adequate, suffered somewhat at high power. The following images were taken at an output power of 3.4 W (tuned to 589 nm) operating the laser near our maximum dye pressure of 80 psi. The pupil and image on the sky are shown in Figure 6.2. The illumination of the beam projector pupil is clearly less than optimum. Some of the light is clipped on the right edge and at the top and bottom of the pupil. However, the far field image was generally good, regardless of the beam projector pupil illumination. The sky image is the result of 6 images from the 6 apertures of the old MMT, superimposed at the image plane. We suspect that the elongation is the result of imperfect overlap of the images. In general, we expect an elongation of about 0.6 arc seconds for a mirror displaced by 2 m from the beam projector, and a sodium layer extending from 80 to 90 km above the telescope. However each mirror would generate an image with an elongation in a different direction, such that when overlapped, the contributions of elongations would be roughly symmetric.

6.3 Power Optimization

Dye lasers are generally designed to work over very wide wavelength ranges, and thus are not necessarily ideal for maximizing the gain and reducing the losses at the specific wavelength required for a sodium guide star. Our efforts were directed toward reducing the most significant losses in the pump beam to maximize the power output for our desired wavelength of 589 nm.

Except for certain high-power pulsed dye lasers funded by classified Department of Defense and Department of Energy programs, there has been little progress in pushing the power of the laser beyond the 3 Watt limit obtainable *in situ*. The upper

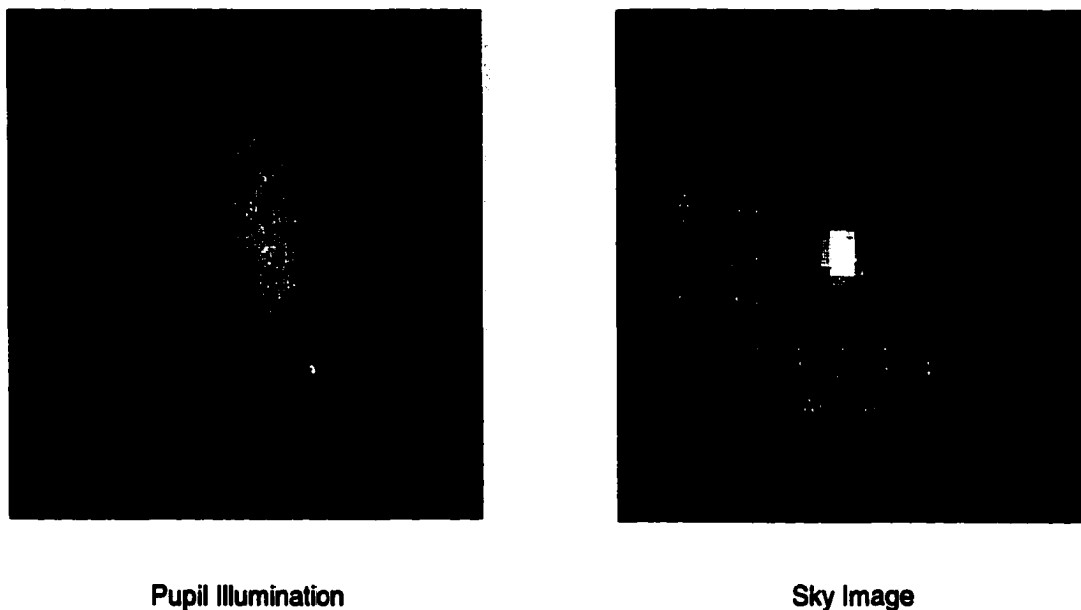


FIGURE 6.2. Pupil illumination pattern (left) and far field image (right) of the dye laser at maximum power. One arc second on the sky corresponds to 60 pixels.

limit to power in a dye laser using Rhodamine 6G was recognized by Jonston[48] as the result of thermal blooming in the dye stream when excited by the Argon ion laser. Quantum losses in the dye result in heat which causes a rapid expansion of the dye solvent (ammonyx-ethylene glycol mixture), spoiling the uniformity of light propagation through it. The expansion of the liquid is greatest in the center, and results in a negative lensing effect which defocuses both the pump beam and the dye beam.

6.3.1 End Pumping

One significant source of loss in the original ring-cavity design results from an inefficient pumping geometry. As was seen in Figure 6.1, the argon ion laser pumps the dye jet at a different angle from the beam angle in the resonator cavity. The minimum angular difference for our configuration is 12 degrees, being limited by the

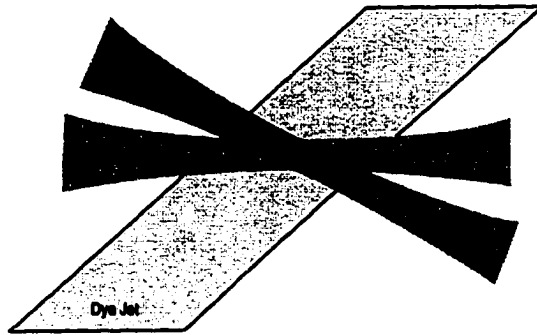


FIGURE 6.3. Area of overlap in dye jet in which pumping is effective.

f-numbers of the mirrors used to focus the pump beam and the cavity beam. This has two deleterious effects. First, since the dye jet is oriented at Brewster's angle in the cavity beam, it thus cannot be at Brewster's angle in the pump beam. This results in a reflection loss of the pump off the front surface of the dye of 0.59%.

Much more serious is the overlap loss which occurs when portions of the argon-ion laser beam pump volume elements in the dye which do not lie within the volume of the cavity beam, as shown in Figure 6.3. This represents the two beams crossing at an angle in the middle of the dye jet. The area of overlap is the only portion of the area in which the pump beam excites the dye, and the volume of excited dye resides within the cavity beam and can thus be stimulated to emit coherently. The resulting loss was estimated by modeling both beams as narrow cylinders with Gaussian beam intensity profiles. The output beam intensity amplification for any particular volume element within the dye jet is linearly proportional to both the pump beam intensity (assuming we are well below dye saturation) and the cavity beam intensity. Thus, the proportional overlap loss can be calculated as

$$\frac{I(\theta)}{I(0)} = \frac{\iint_{-\infty}^{\infty} e^{-2\left(\frac{\sqrt{x^2+y^2}}{r_c} + \frac{\sqrt{(x-[z-t/2]\sin\theta)^2+y^2}}{r_p}\right)^2} dx dy}{\iint_{-\infty}^{\infty} e^{-2\left(\frac{\sqrt{x^2+y^2}}{r_c} + \frac{\sqrt{x^2+y^2}}{r_p}\right)^2} dx dy} \quad (6.1)$$

where $I(\theta)$ is the intensity at overlap angle θ , $r_c = 20\mu m$ and $r_p = 20\mu m$ are the

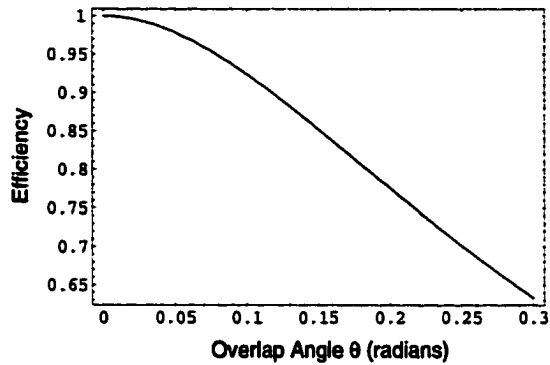


FIGURE 6.4. Argon-ion pumping vs. pump incidence angle.

$1/e^2$ radii of the cavity and pump beams, θ is the angle of the pump beam with respect to the cavity beam, $\alpha = .01\mu m^{-1}$ is the attenuation coefficient of the pump beam through the dye, and $t = 200\mu m$ is the thickness of the dye jet along the cavity beam which propagates in the z direction. The result of this integration is seen in Figure 6.4 where we see that for our nominal input angle of 12 degrees ($\theta = 0.21$) the overlap efficiency has dropped to nearly 75% of its co-aligned value. Thus, there is the potential of 1/3 more power out of the system if a method can be found of aligning the pump and cavity beams.

This was achieved by fabricating a high-quality dichroic mirror for use in the dye laser. The mirror is a high reflector ($> 99.5\%$) at the 589 nm sodium wavelength, but has a transmission of $> 95\%$ at the wavelengths of the argon-ion pump laser (488 nm - 514.5 nm). The mirror is made of fused silica, and because of the concavity of the mirror surface, acts as a slightly negative lens element for the pump beam. The pump beam is focussed through the dichroic mirror by a 100 mm achromat mounted in a 5-axis mount. Because of the fine degree of motion of the output pump beam that is attained with the positioning of this lens, it is used as our primary control over the focus and translation of the pump beam in the dye jet. The tip and tilt axis of the lens are controlled to match the astigmatism of the pump beam to the residual astigmatism (after the astigmatic compensator) of the cavity beam.

The result of this end-pumping arrangement appears to be an approximate power boost of almost 15%¹. Control of the location and focus of the pump beam is significantly simpler with this arrangement, and allows for a wider range and more convenient adjustment than the pump mirror did. One minor drawback of this arrangement is that there is still a residual 5% reflection of the 514.5 nm argon ion pump beam from the mirror surface of the dichroic mirror. This reflection is then refocused through the pump lens to a narrow beam which requires caution.

6.3.2 Faraday Etalon

In any laser system, the cavity power density (and consequently, the output power) varies exponentially with the negative of the losses [99], so minor reductions in the intra-cavity losses can yield substantial gains in the output power. This is especially true for lasers with relatively high degrees of feedback ($> 90\%$). Efficient power extraction requires that the losses of all of the many elements of the laser be driven as low as possible. All mirror surfaces are dielectric high reflectors with the exception of the output coupler. Most surfaces within the cavity, including even the dye jet, are situated at Brewster's angle which effectively minimizes loss for the p-polarization oscillating through the cavity.

In minimizing the losses of the optical surfaces in the laser cavity, it is essential to keep the optics as clean as possible. This necessitated frequent removal and careful cleaning of the optical elements, and maintaining the laser cavity and elements in a sealed box for as much of the time as possible. To maintain a thermally stable, dust free environment for the laser optics as much as possible, picomotor drivers were placed on the tuning elements and the pump lens, allowing us to optimize the cavity while keeping it sealed. Even then, there were scattering losses from many of the

¹The actual power increase is difficult to ascertain because of the adjustment of the cavity that results from changing the pumping configuration. Nevertheless, the peak sustainable power readings before and after using end-pumping are 3.0 W and 3.4 W, respectively.

surfaces which reduced power in the cavity, and ultimately the output beam. The next step was to reduce the number of scattering surfaces.

In all, the cavity consists of four mirrors, a plane-parallel astigmatic compensator, three birefringent filters, two etalons, a Faraday rotator and an optical derotator, as shown in Figure 6.1 . Including the two surfaces of the dye jet makes 22 surfaces in all. The number of mirrors can conceivably be reduced to three (or even two in a standing-wave cavity) but the ensuing astigmatism from highly off-axis mirrors and the difficulty of establishing a workable cavity makes it hardly worth the half-percent loss that the mirror at worst produces.

One method of reducing the number of surfaces was to combine the function of the fine-tuning etalon with that of the Faraday rotator. To achieve this, we needed to make a custom etalon using a glass with a high Verdet constant, as well as excellent internal transmission at $\lambda = 589$ nm. The glass that best fits these two criteria is SF57 from Schott [94]. Its internal transmission is 0.996 over 25mm, with a Verdet constant of 26.2 rad/(T m). The Faraday polarization rotation of the beam in a material with a Verdet constant of $V(\lambda)$ of thickness t is given by

$$\alpha_0 = BV(\lambda)t \quad (6.2)$$

where B is the magnetic field. To generate the magnetic field, we used a NdFeB ceramic magnet which we measured to have a longitudinal B-field strength of 0.38 T.

We desired a thickness for the Faraday etalon that would complement our existing 0.5 mm fused silica coarse-tuning etalon and match the polarization rotation of the quartz optical derotator. This etalon was bare fused silica ($n = 1.46$) working in near-normal incidence, with a single-surface field amplitude reflection coefficient of 0.187. The thickness of the quartz optical rotator was interferometrically measured to be 0.134 mm. With a rotatory power of 21.7 degrees/mm, the rotation of the quartz plate was calculated to be 2.91 degrees. Then, using a yellow HeNe laser and the rotation controller for the birefringent filters, I made three measurements of the

polarization rotation, which averaged to 2.93 degrees ($\pm 5\%$).

The 2.93 degree polarization rotation of the quartz plate dictated that we needed an equal amount of counter-rotation from the Faraday etalon. However, with the magnetic field available this would require an etalon of SF57 of thickness a little less than 5 mm². This thickness in such a high-index material ($n_{SF57} = 1.846$) would not have separated the modes of the etalon sufficiently, so we compromised: less optical rotation and more mode separation. We decided on a 3.5 mm etalon of SF57 glass.

From equation 6.2, this thickness introduces a polarization rotation of 2.0 degrees for single pass of the beam through the material. However, since the etalon works through multiple passes of the beam, and the polarization rotation is relative to the direction of the B-field rather than relative to the direction of propagation, successive passes will increase the rotation. Adding the field amplitudes of successively rotated beams results in a final beam polarization rotation of

$$\alpha_{tot} = \tan^{-1} \frac{\sum_{j=0}^{\infty} \left(\frac{n-1}{n+1}\right)^{2j+1} \sin((2j+1)\alpha)}{\sum_{j=0}^{\infty} \left(\frac{n-1}{n+1}\right)^{2j+1} \cos((2j+1)\alpha)} \quad (6.3)$$

which results in a rotation angle of 2.4 degrees. This amount of rotation will substantially cancel the 2.93 degree rotation introduced by the quartz derotator.

One final factor had to be considered before committing resources to this approach: the rotation of successive reflections in the etalon causes a bit of inefficiency in the coherent addition of the E-fields. A little algebra shows that the resultant intensity, assuming E-field amplitude reflectance of r and single pass rotation of ρ , is

$$|E^2| = E_0^2(1+r^2)^2 \left(\frac{1}{1-r^4} + 2 \sum_{m=0}^{\infty} \sum_{n=1}^{\infty} r^{2n+4m} \cos(2n\rho) \right) \quad (6.4)$$

which converges to 0.999 E_0^2 . Thus, the loss resulting from the imperfect rotation

²The actual value must take into account the addition of multiply reflected fields, as shown shortly. For the rough design, the first-order calculation is sufficient.

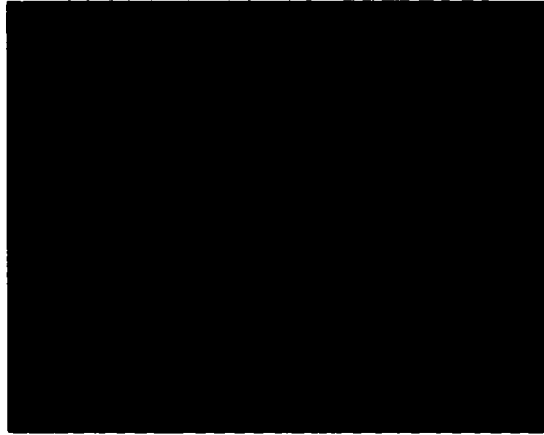


FIGURE 6.5. The Faraday etalons used as Faraday rotators and line-narrowing etalons.

match between successive reflections is much lower than the loss to be expected from surface scattering, and will be considered negligible here.

After locating a small block of SF57, we contracted with Tucson Optical Research Corporation (TORC) in Tucson to make the etalon. Fabrication of the etalon proved to be quite difficult. SF57 is a very soft glass (Knoop hardness of 350, compared to 610 for BK7 [94]), and difficult to polish to a laser-quality finish. The difficulty was compounded by the requirement that the etalon fit in the small opening of the magnet, and that the surfaces be maintained within an arc second of coplanarity. The two etalons that were delivered are shown in Figure 6.5. Unfortunately, they were thinner than we had requested (3.05 mm) reducing the Faraday rotation angle even more. Using this thickness a total rotation of 2.1 degrees is calculated. Measurements of the polarization rotation of the etalon in the magnet resulted in 2.6 degrees, slightly more than expected, and very close to the 2.9 degrees needed to cancel the optical derotator.

The tuning curves for the pair of etalons is shown in Figure 6.6. The thickness and high refractive index of the Faraday etalon reduce its free spectral range, such that it is difficult to get the laser to operate in a single mode. For the previous etalon set,

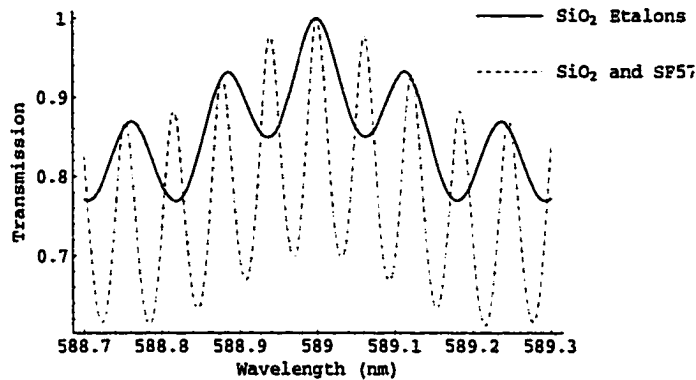


FIGURE 6.6. The results of tuning the cavity using the original configuration of two fused silica etalons (solid line) and using the thin fused silica and thick Faraday etalons (dashed line). The high refractive index of SF57 used in the Faraday etalon narrows and deepens the transmission curve considerably.

the transmission of the first side orders peaked at .93, while for the new combination, transmission in the neighboring orders peaks at .98. The separation of orders is a mere 0.05 nm (43 GHz). The spectral width of each order is much narrower, in part because of the high refractive index of SF57.

Upon placing the Faraday etalon in the dye laser cavity, it was clear from observation that it scattered more than the fused silica etalon. The excessive scattering can even be seen in the scattered light recorded in Figure 6.5. This severely limited the etalon's effectiveness in reducing the intracavity losses, and may have even exacerbated the scattering.

Tuning the laser with the new Faraday etalon was only partially successful. Some work was required to align the cavity before the SF57 and quartz derotator successfully acted as a one-way limiter forcing unidirectional laser oscillation. After that, the coupling of the unidirectional oscillation with the tuning action of the etalon made it very difficult to tune. Finally, and most significantly, the laser power dropped upon insertion from 2.5 W (tuned, but bi-directional oscillation) to a stable 1.4 W of tuned, unidirectional power. Eventually we obtained a total of 2.5 W out of the laser using

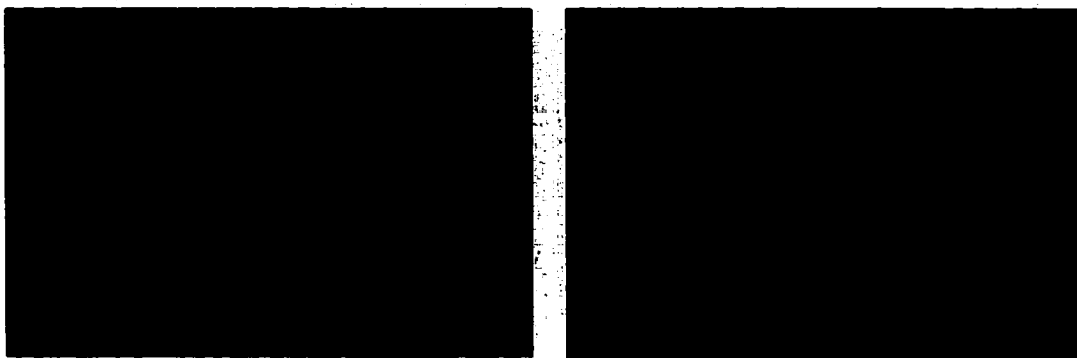


FIGURE 6.7. Scattering of HeNe laser light from the surfaces of the SF57 Faraday etalon (left) and a comparable sapphire window (right). The exposure of both photos is the same. The scattering of the Faraday etalon is clearly greater.

the new Faraday etalon, but never approached our previous power records of over 4 Watts with the fused silica etalon set. We replaced the original Faraday rotator, and used the Faraday etalon without the magnet as a simple tuning etalon, but the output power results did not improve.

We have identified three possible explanations for the disappointing results from the Faraday etalon: (1) the etalon surfaces are too rough, resulting in excessive scattering loss, (2) the thickness of the etalon and the requirement to operate it in the cavity in non-normal incidence results in excessive beam walkoff, and (3) the surfaces are not sufficiently co-planar, resulting in excessive beam walkoff.

Excessive scatter from the polished surfaces of the Faraday etalon was observed to be the case. As shown in Figure 6.7, qualitative comparison of scattered laser light from the Faraday etalon surface is much higher than that from a normal sapphire window. This is expected to be a significant contributor to the disappointing power results. A silicon detector placed 25 cm from the surface at an angle of 45 degrees with respect to the normal recorded 1.83 times as much scattered red HeNe light from the Faraday etalon (after background subtraction) as from a comparable sapphire window. This effectively spoils any advantage to reducing the surface count, though it does not fully account for the reduction in system power.

Excessive non-normal beam walkoff seems unlikely because the reduction in power occurred for all angles of the etalon, even when not properly tuned to the sodium D₂ line. During the course of experimenting with the etalon, at some point the surfaces would have had a proper near-normal path length such that one of the preferred 10 MHz lines would have resonated. At that time, though not properly tuned to the D₂ line, the power would have increased significantly as the feedback forced all of the power into this non-resonant line. Since this was never observed, it is considered a minor contributor to the losses.

To measure the angle between the two surfaces of the Faraday etalon, a helium neon laser was directed onto it at normal incidence, and the front and back surface reflections were observed. After propagating 2.64 m they were separated by 13 mm giving a total divergence angle of 0.28 degrees (17 arc minutes). A reflected angle of θ will be induced by a wedge angle α_0 of

$$\alpha_0 = \frac{1}{2} \sin^{-1} \left(\frac{\sin \theta}{n_{SF57}} \right). \quad (6.5)$$

With $n_{SF57} = 1.846$ and $\theta = 0.28$ deg the surface angle is 0.076 deg or 273 arc seconds.

This is more than two orders of magnitude beyond the specification of < 1 arc second. With a refractive index of 1.846 at near normal incidence, the Fresnel reflection per surface will be about 8.84%. We can make an estimate of how much walkoff occurs from this wedge angle. If the beam is normally incident at the front surface, it will encounter the second surface at the angle α_0 , and propagate back such that the displacement Δy of the reflected beam at the front surface is

$$\Delta y_1 = t \sin 2\alpha_0 \quad (6.6)$$

or 14.7 μm . This is only for the first reflection. Each subsequent reflection encounters the surface at a steeper angle, such that for the n_{th} reflection the angle of incidence

(with respect to the surface normal) is

$$\alpha_n = \alpha_0 + \alpha_{n-1} \quad (6.7)$$

$$= n\alpha_0. \quad (6.8)$$

We are concerned with how the beams add up at the second surface, so looking at even numbers of reflections we get total walk-off amounts of

$$\Delta y_m \approx 2t \sin(2m\alpha_m) + \Delta y_{m-1} \quad (6.9)$$

$$\approx 4t\alpha_0 \sum_{i=1}^m m \quad (6.10)$$

where the iterator m is now over each *pair* of reflections and we have neglected the lengthening of the path of $1/\sin \alpha_0$ between successive reflections. The walkoff amounts for the first five pairs of reflections are 29.3 μm , 88.0 μm , 176.0 μm , 293.4 μm , 440.1 μm . The high index of the etalon guarantees that the amplitude reflected for several orders will be significant, and with this much walk-off the beam constructive interference (and consequently the transmission) is spoiled. This has the potential for explaining the loss of power with the insertion of the etalon. The poor quality of the surface and the poor parallelism combine to result in an overall loss of power in the cavity.

6.3.3 Optical Rotator Etalon

During the development of the Faraday etalon, we began to consider the possibility of finding a material which might also act as an optical derotator as well as the coarse-tuning (thin) etalon. The requirement for this material is that it be roughly the same optical thickness as the fused silica etalon it was to replace (2 mm in thickness or about 2.9 mm of optical thickness), that it have very high transmission at $\lambda = 589$ nm, and that it have sufficient optical activity to counter the Faraday rotation of the other etalon. After considering several crystalline materials, we discovered that TeO_2

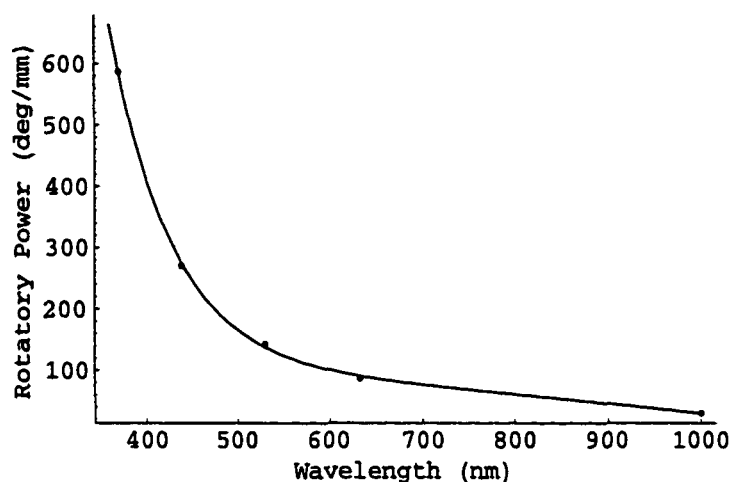


FIGURE 6.8. Fit of rotatory power of TeO_2 to the data points given in Yariv and Yeh [115]. The fit is a linear fit to inverse powers of λ . Based on this, the rotatory power at 589 nm is 105 deg/mm.

appeared to be a promising candidate [115]. The rotatory power of the material is proportional to the refractive index difference between left and right circularly polarized waves, and inversely proportional to the wavelength undergoing the rotation. The values of five data points for TeO_2 found in [115] were fit with a function of inverse powers of λ , similar to refractive index fitting functions. The result of the fit is shown in Figure 6.8. Based on this function, the rotatory power at 589 nm is estimated to be 105 deg/mm.

An optical rotator based on TeO_2 would require that to effect a rotation of 2.6 degrees the thickness of the material be just 25 μm . However, the rotator would also work properly if it produced rotations of $n \times 180 + 2.6$ degrees, where n is an integer. Using the first half-rotation order ($n = 1$) requires an etalon 1.74 mm thick. Given the high optical activity of this material, very accurate polishing and interferometric (or polarization) measurements would be required to get exactly the right thickness. Furthermore, the refractive index of this material is very high ($n_{\text{TeO}_2} = 2.35$ [115]) so that the optical thickness is almost 4.1 mm. At first glance, this thickness does not work well with the optical thickness of the Faraday etalon (5.63 mm). However,

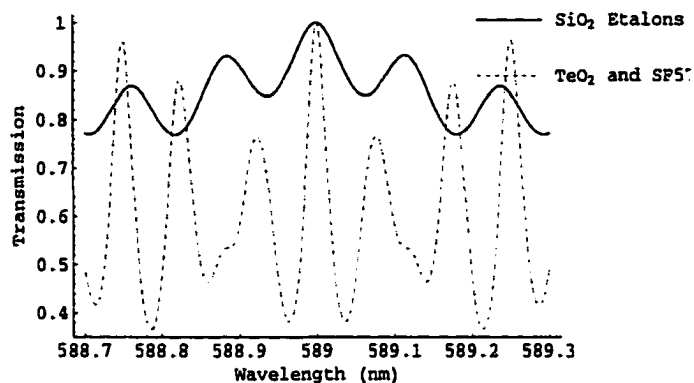


FIGURE 6.9. Transmission of Faraday etalon and TeO_2 etalon pair (dashed line) compared with standard fused silica etalon pair (solid line).

since the refractive index is high, both etalons will have much higher finesse and the transmission stays well below that of the fused silica etalon pair for almost 2 \AA on each side of the peak, as shown in Figure 6.9.

A 10 mm thick sample of TeO_2 was obtained from Commercial Crystal Laboratories, and its transmission was found to be good at 589 nm. However, the crystal sample was deemed too expensive, and the potential power boost too small to continue with fabrication.

6.4 Measurement of Mode Structure

The relationship between the sodium column density and sodium guide star brightness can be firmly established if the conditions of the laser are known very well. Laser tuning, spectral width, spectral (longitudinal) mode, output power and beam quality will all have an effect on the sodium response. If the laser is operating in the small-signal gain region, *i.e.* well below saturation, and if all of the resonant power can be collected on a small group of detectors, then beam quality can be eliminated as a factor, since the total amount of light produced only varies if saturation occurs. Laser tuning is easily confirmed by using a resonant sodium cell, and the total output



FIGURE 6.10. Typical Fabry-Perot image used to monitor frequency and mode-hopping of dye laser.

power is easily determined with a power meter. This leaves the total spectral width of the laser, and its spectral mode structure as the only remaining parameters.

During 1997-8, we firmly established the correlation between sodium column density, as measured by high-resolution spectral absorption of a telluric star, and sodium beacon return [36]. To monitor the spectral purity of the output of the guide star laser during these experiments, I developed a Fabry-Perot interferometer, the output of which is seen in Figure 6.10. The mirror spacing was 10 cm, resulting in an order number of approximately 3.4×10^5 , and a free spectral range of 1.5 GHz.

The input to the interferometer was a small stray reflection off of one of the cavity tuning elements, diffused through some lens tissue paper at the input mirror. The Fabry-Perot output was focussed onto the CCD to reveal a mode spacing of 276

MHz. This output was recorded on a video tape recording at 30 frames per second throughout the duration of the data acquisition. The data revealed the laser to be hopping principally among four longitudinal modes, spending almost 30 percent of the time in each of the central three modes, and the majority of the remainder in a mode separated from the peak by 550 MHz [36]. These data were combined with the continuous monitoring of the laser frequency peak on the high-resolution echelle spectrograph confirmed by the sodium resonance cell and the power measurements made before and after the integration, to establish that we were operating with an efficiency of 82%.³

The sodium guide star return was measured during photometric conditions in sequential sets of frames with integration periods lasting from 3-5 seconds. Typically 10 frames of data were taken during each set, lasting about 3 minutes. During this period, the laser mode was recorded on the Fabry-Perot etalon. Simultaneously, the sodium column density was measured at the same region of the sky by the R=50,000 Advanced Fiber Optic Echelle spectrograph at the 60-inch Center For Astrophysics (CFA) telescope, about 1 km away from the MMT. Column density was obtained by observing the depth of the sodium D₁ absorption line from a bright ($m_V > 3$), early-type star (α Leo, α Aql, β Tau and α And).

These measurements fixed the sodium guide star astronomical brightness at $m_V = 10.1$ for 1 Watt of projected circularly-polarized laser light with the spectral and temporal characteristics of the dye laser, at the mean sodium layer column density of $3.7 \times 10^9 \text{ cm}^{-2}$ at our latitude [35]. These measurements were crucial to the correlation of sodium return with sodium column density, and for establishing the optimum operating requirements for future guide star lasers.

³This is the product of the amount of time spent in each mode and the Doppler-broadened sodium response per mode.

6.5 Conclusions

We have used a dye laser with Rhodamine 6g to produce a sodium guide star at the MMT. By using unconventional end-pumping methods we have increased the pumping efficiency in the lasing mode, resulting in a power increase of over 10%. We developed methods of having the tuning elements in the cavity act simultaneously as the optical diode, limiting the ring cavity oscillation to one direction, thus reducing the number of scattering surfaces in the laser. While the Faraday etalon concept was demonstrated in practice, it did not result in an increase in output power. This was most likely because of the high surface scatter from the poor polish of the etalon surface, and the residual walk-off of the beam within the etalon.

By making careful measurements of the power and longitudinal mode of the laser measured with a Fabry-Perot etalon, we used the dye laser to make the first simultaneous measurements of mesospheric guide star brightness and sodium column density. These measurements were essential to understanding guide star production, and play a role in the development of future laser guide star systems.

Chapter 7

RAMAN LASER DEVELOPMENT

7.1 Introduction

7.1.1 Nonlinear Optics

Raman lasers make use of Stimulated Raman Scattering (SRS), one of the many varied nonlinear optical processes involving the nonlinear response of a material's polarization \mathbf{P} to an applied electric field \mathbf{E} . These two fields are related to one another through the electric susceptibility χ , in most cases allowing \mathbf{P} to be expanded as a power series in electric field strength such that

$$\mathbf{P} = \epsilon_0 \chi^{(1)} \mathbf{E} + \epsilon_0 \chi^{(2)} \mathbf{E}^2 + \epsilon_0 \chi^{(3)} \mathbf{E}^3 + \dots \quad (7.1)$$

The terms $\chi^{(1)}$, $\chi^{(2)}$, and $\chi^{(3)}$ are the first order, second order, and third order dipole susceptibilities, respectively, and are in general tensors of rank $n + 1$ where n is the aforementioned order. For small amplitude electric fields a linear description of the polarization generally suffices, giving rise to the refractive index n and the absorption coefficient α for the real and imaginary parts of P , respectively. For more intense electric fields, the higher order terms in eqn. 7.1 become important. The second order susceptibility $\chi^{(2)}$ gives rise to parametric processes such as second harmonic generation, sum- and difference-frequency generation, and optical parametric oscillation. These are processes in which the material acts as a medium to facilitate the transfer of energy among optical waves. In such processes there is no transfer of energy to or from the medium. Symmetry considerations demand that the even order dielectric dipole susceptibilities vanish in materials with inversion symmetry, so second-order effects are predominantly observed in materials lacking such symmetry¹.

¹When these effects are seen in materials with inversion symmetry, it is a result of the quadrupole expansion terms, which are generally much smaller than the dipole expansion elements.

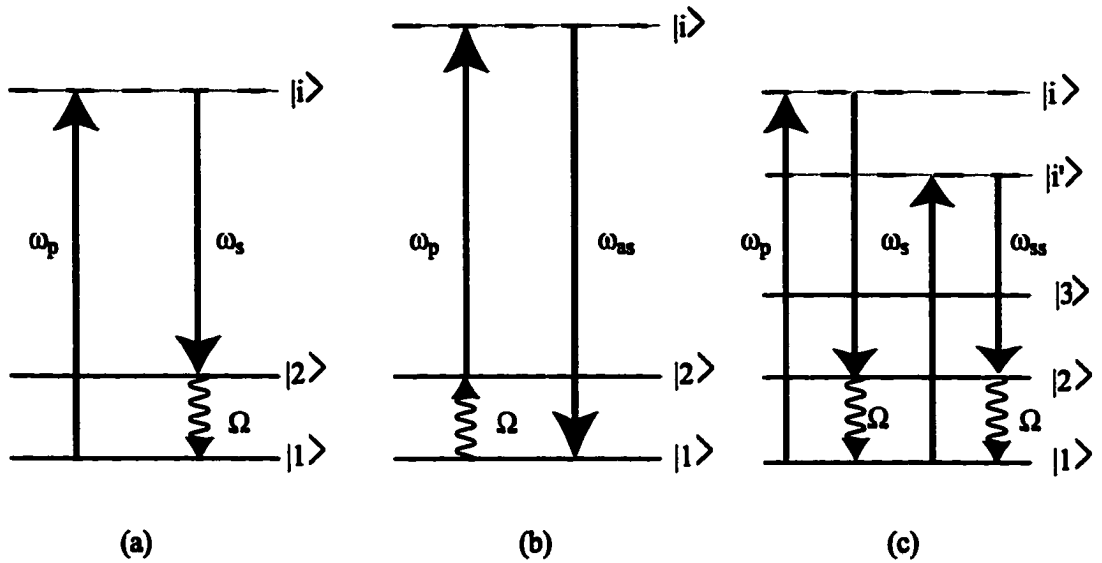


FIGURE 7.1. Energy diagrams depicting various Raman processes: (a) single Stokes shift, (b) anti-Stokes shift, and (c) second Stokes shift.

7.1.2 Spontaneous Raman Scattering

In materials *with* inversion symmetry, an intense electric field then gives rise to a polarization of the type

$$P_{\text{asym}} \approx \epsilon_0 \chi^{(1)} E + \epsilon_0 \chi^{(3)} E^3. \quad (7.2)$$

The nonlinear process is governed by the magnitude of the fourth-rank $\chi_{ijkl}^{(3)}$ susceptibility tensor. In general, materials in which $\chi_{ijkl}^{(3)}$ is negative and purely imaginary have high Raman scattering coefficients.

In the process, an incident pump beam photon of energy $\hbar\omega_p$ and momentum $\hbar\mathbf{k}_p$ inelastically scatter from the medium, generating a Stokes photon ω_s and \mathbf{k}_s and a phonon Ω and \mathbf{K} such that energy and momentum are conserved

$$\omega_p = \omega_s + \Omega \quad (7.3)$$

$$\mathbf{k}_p = \mathbf{k}_s + \mathbf{K}. \quad (7.4)$$

The overall effect is demonstrated in the energy diagram of Figure 7.1(a). The material begins in its ground state $|1\rangle$ and is excited to an intermediate state $|i\rangle$ by the pump photon of energy ω_p . The intermediate state may be either a real state, or a virtual state of the material. From there, it decays to another vibrational state of the system, $|2\rangle$, through emission of a photon of energy ω_s . The resulting Stokes wavelength, λ_s , is lower in energy by the vibrational energy difference between states $|1\rangle$ and $|2\rangle$ of the system. This is the process of spontaneous Raman scattering, and its probability is usually very low, resulting in very small fractions of scattered light for most materials. The reverse process of anti-Stokes scattering, in which the molecule begins in state $|2\rangle$ and ends in state $|1\rangle$ is generally even lower in probability because of the reduced number of molecules beginning in state $|2\rangle$.

It is common for Raman shifts and bandwidths to be expressed in units of cm^{-1} . For a pump laser of wavelength λ_p and a Raman shift of ν_R , the wavelength of the resulting radiation is

$$\frac{1}{\lambda_p} - m\nu_R = \frac{1}{\lambda_s} \quad (7.5)$$

where m is the Stokes order. For a single-Stokes process, $m = 1$, while for second Stokes $m = 2$, etc. For an anti-Stokes process $m = -1$.

Normally, the values comprising the third-order susceptibility $\chi^{(3)}$ are not directly measured; instead the scatter of a material is measured at various angles from the incident beam, and from that the differential molecular cross-section is computed. The value commonly reported for Raman-active materials is $\frac{d\sigma}{d\Omega}$ a measure of the scattering cross-section per molecule into a differential solid angle $s\Omega$. It should be noted that this value is *not* constant with pump beam wavelength; rather the quantity $\frac{1}{\nu_s^4} \frac{d\sigma}{d\Omega}$ is. If we substitute for ν_s using eqn. 7.5 and take the logarithm, we find that

$$\ln \left(\frac{d\sigma}{d\Omega} \right) = -4 \ln \lambda_p + C + 4 \ln(1 + \lambda_p \nu_R). \quad (7.6)$$

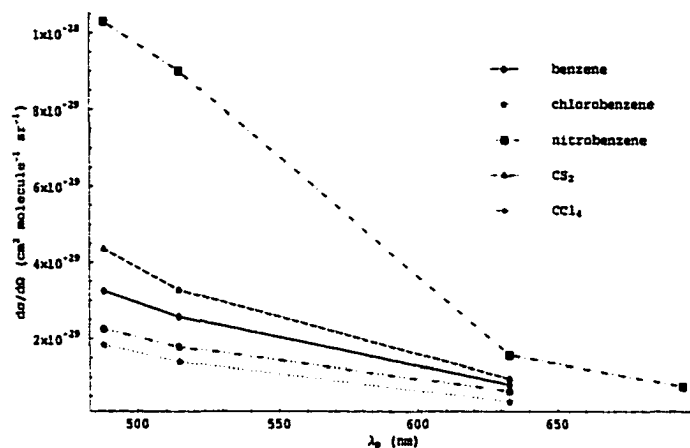


FIGURE 7.2. Variation in molecular Raman scattering coefficient $d\sigma/d\Omega$ for excitation at various pump wavelengths, λ_p .

Because λ_p is so small, it dominates the other terms, so a crude approximation has $\frac{d\sigma}{d\Omega}$ varying as $1/\nu_p^4$.

From data provided in [114], the general dependence of $d\sigma/d\Omega$ on λ_p can be checked. The scattering coefficient per molecule for a few materials at a few laser wavelengths is plotted in Figure 7.2. By using a logarithmic fit to these data, a general trend of cross-section as a function of wavelength can be established. The data points, and the logarithmic functions that fit them best are shown in Figure 7.3. With so few data points, the trends are only general, but nevertheless appear to be reasonably consistent from molecule to molecule and follows a trend of

$$\ln\left(\frac{d\sigma}{d\Omega}(\lambda_p)\right) = -s \ln(\lambda_p) \quad (7.7)$$

where s is a fitting constant that eqn. 7.6 predicts should be close to a value of -4. The values for these fit lines actually vary from -4.9 to -7.7, but are sufficient for the purposes of predicting the general trends.

Note that the scattering cross section is quite low, on the order of 10^{-29}cm^2 . This is many orders of magnitude lower than the stimulated emission cross section for most laser ions which are on the order of $10^{-17} - 10^{-20}\text{cm}^2$.

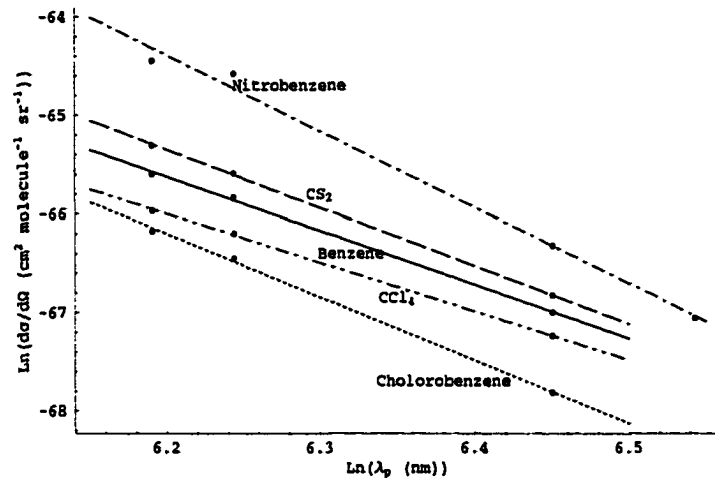


FIGURE 7.3. Fit lines applied to the natural logarithm of the scattering coefficients shown in Figure 7.2.

7.1.3 Stimulated Raman Scattering

When the pump beam has sufficient intensity to drive molecules to the intermediate state $|i\rangle$ faster than they can spontaneously decay, then a population inversion will exist in which $|i\rangle > |2\rangle$, and gain is possible. In this event, the amplitude of the scattered wave E_s , the so-called Stokes wave, grows along the propagation axis z according to the differential equation

$$\frac{dE_s}{dz} = \frac{6\pi\nu_s}{4n_s c} \chi'' |E_p|^2 E_s, \quad (7.8)$$

where n_s is the refractive index of the scattering material at the Stokes frequency ν_s . This leads to exponential growth of the wave in the initial stages where pump depletion is negligible, and get a concomitant exponential growth in the intensity of the Stokes beam, I_s , according to

$$I_s(z) = I_s(0) e^{g_R I_p z}. \quad (7.9)$$

The factor g_R in the exponent above is the Raman running gain, and has the value

$$g_R = \frac{6\pi\nu_s}{n_s n_p c^2 \epsilon_0} \chi''. \quad (7.10)$$

As in the previous section, we prefer to express these values in the more experimentally-grounded Raman scattering coefficient

$$g_R = \frac{4c^2 N}{h\nu_s^3 n_s^2 \Gamma} \frac{d\sigma}{d\Omega}. \quad (7.11)$$

Raman running gain values are typically quite low, on the order of 1 cm/GW, a consequence of the low probability of interaction of the pump photon ν_p with a virtual photon at the Stokes wavelength ν_s . The small running gain implies that efficient SRS will require high $I_p L$ products, where L is the interaction length of the SRS process.

Note that the Raman running gain is proportional to $\frac{1}{\nu_s^3} \frac{d\sigma}{d\Omega}$. Since we have already noted that in general $\frac{1}{\nu_s^4} \frac{d\sigma}{d\Omega}$ is a constant, then the Raman gain increases linearly with pump energy. Likewise, the spot to which the pump beam can be focussed in the material is smaller for shorter wavelength pump beams, so the intensity increases by the square of the photon energy. The result is that the total scattering gain increases by a factor of 8 for Raman conversion at doubled laser wavelengths. Thus, in low-gain materials, it is advantageous to frequency-double the input beam prior to Raman-shifting in order to exploit this gain increase for efficient Stokes conversion. In this case, however, two Stokes shifts are required to effect the same complete shift, whereas only one would have been required had Raman shifting been performed first. In addition, one must realize that not all of the gain increase is realized because the pump beam experiences losses in the doubling process, so its pump intensity may be lower, partially offsetting the gain increase in the exponent of the Raman wave buildup.

It should also be noted that the gain is inversely proportional to the Raman linewidth Γ . Since some slight amount of tuning will generally be required for any process in which tuning to a spectral line is critical, a moderately large Γ will be advantageous. Thus there is a tradeoff to be considered in the final choice of a Raman material, in which larger values of Γ allow more efficient tuning, but simultaneously reduce the Raman gain.

The Stokes wave grows exponentially until it is limited, usually by pump depletion. In that case, the value I_p decreases exponentially, though by then much of the power of the incident pump wave has been converted to the Stokes wave. Once the Stokes wave has built up to sufficient intensity, it too can act as a source to further generate SRS, resulting in a second Stokes shift as seen in Figure 7.1. Multiple Stokes shifts out to many orders have been observed in high-gain materials. In addition to multiple Stokes processes, anti-Stokes processes also occur, in which phonons are annihilated, generating higher energy photons. Because of the requirement for the existence of another particle (the phonon) at the time and place of scattering, the probability for this process is generally significantly lower than for equivalent Stokes processes.

7.2 Review of Potential Raman Laser Candidates

Because of the significant number of powerful lasers, the vast number of potential Raman-active materials and even greater number of scattering transitions available with these materials, the number of combinations to consider quickly becomes very large. In a systematic approach to finding potential candidates for Raman lasers, we have restricted consideration to those lasers which have been demonstrated to produce significant amounts of power (greater than 1 W), and only those Raman materials with relatively high Raman-scattering gains (on the order of 1 cm/GW). In addition to the shifts and bandwidths, other factors are also important, such as spectral transparency, damage thresholds, ease of growth and attainable crystal sizes, but these will be considered after potential shifting candidates are identified.

7.2.1 Raman-active Materials

Many Raman-active materials have been identified and their Raman shifts have been measured and cataloged for use in spectral identification. The amount of Raman scattering is more difficult to measure accurately, and thus is often not reported. Accord-

ing to [86], most molecular gasses have Raman spectra ranging from 600-4150 cm^{-1} whereas most liquids have slightly lower energy spectra ranging from 600-3500 cm^{-1} . At one time solids were not thought to be particularly promising as Raman active materials [12] because most Raman activity was originally observed as rotational and vibrational modes of free molecules. The subsequent discovery of the high Raman-activity of tungstate materials and their shifts in the region of 900-1000 cm^{-1} have made them very popular as solid-state Raman shifting materials. Various Raman active materials, their principal energy lines, and their energy bandwidths are shown in Table 7.1.

Material	Shift (cm^{-1})	Linewidth (cm^{-1})	Source
LiTaO ₃	201	22	[114]
LiTaO ₃	215	12	[114]
LiNbO ₃	250	28	[11]
LiNbO ₃	256	23	[114]
Li ⁶ NbO ₃	266	-	[114]
CCl ₄	459	-	[114]
SiO ₂	464.5	7	[11]
Li ⁶ TaO ₃	600	-	[114]
LiNbO ₃	632	27	[11]
Ba ₃ (B ₃ O ₆) ₂	636	4.5	[11]
LiNbO ₃	637	20	[114]
Ba ₂ NaNb ₅ O ₁₅	650	-	[114]
Ba ₂ NaNb ₅ O ₁₅	655	-	[114]
CS ₂	655.6	0.5	[114]
KYb(WO ₄) ₂	757	15	[11]
KY(WO ₄) ₂	767.4	8.4	[11]
KGd(WO ₄) ₂	768.	6.4	[11]
NaBrO ₃	799.5	2.5	[11]
LaNbO ₄	805	9.0	[11]
LiIO ₃	821.6	5.0	[11]
LiNbO ₃	872	21	[11]
KGd(WO ₄) ₂	901.	5.4	[11]
KY(WO ₄) ₂	905.6	7.0	[11]
KYb(WO ₄) ₂	908	7.4	[11]
KLuW	908	-	[8]
CaWO ₄	911.8	4.8	current work
NaGd(WO ₄) ₂	919	14	[11]

NaClO ₃	937.	4.9	[11]
Sr ₅ (PO ₄) ₃ F	950.3	2.8	[11]
LiPO ₄	951.	7.7	[11]
Ca ₅ (PO ₄) ₃ F	964.7	2.8	[11]
NH ₄ SO ₄	976.5	3.5	[11]
Benzene	992	2.15	[114]
Toluene	1003	1.94	[114]
Ba(NO ₃) ₂	1048.6	0.4	[11]
NaNO ₃	1069.2	1.0	[11]
CaCO ₃	1086.4	1.2	[11]
Diamond	1332.9	2.7	[11]
NitroBenzene	1345	6.6	[114]
NH ₄ Cl	1712.	6.0	[11]
N ₂	2330	-	[53]
CH ₄	2914	-	[53]
Ethanol	2928	-	[53]
D ₂	2991	-	[68]
NH ₄ Cl	3052	85	[11]
HD	3628	-	[68]
HF	3962	-	[53]
H ₂	4155	-	[114]

Table 7.1: Raman shifting materials

7.2.2 High Power Lasers

Lasers which have demonstrated the potential for high power are shown in the following tables. Each table lists the type of laser, principal wavelengths at which significant power can be obtained, and the spectral broadening of the line. The latter is somewhat representative of the tunability of the laser, though the amount of power attainable off center has not been addressed.

Table 7.2 shows various high-power transitions of a few gas and ion lasers. While inefficient and often cumbersome, the technology for these lasers is mature and reliable, they are commercially available, and the powers produced are often impressive. Many lasing lines exist in these lasers, but the ones listed are the most powerful tran-

Laser	Center Wavelength (nm)	Source
Ar	488	[23]
Ar	514.5	[23]
Ar	458	[23]
Kr	647.1	[23]
Kr	743.6	[23]
Cu	510.5	[25]
Cu	578.2	[25]

TABLE 7.2. High power gas/ion lasers

sitions. In addition to these lasers, ion lasers of Xe, Ne, O, and N ions also exist, but they either have wavelengths far from our region of interest (UV or far IR) or inadequate power.

Table 7.3 lists the solid-state crystal lasers which have shown potential for high power. All of them are based on transitions of the optically active electrons in rare earth materials. The insensitivity of these transitions to perturbing crystal fields and the limited number of atoms and transitions that are capable of high gain cause the lasing wavelengths of most of these lasers to be tightly grouped. Some of these materials have not demonstrated the required lasing power, but for other reasons (Q-switching rate achievable, efficiency, economy, etc.) have nevertheless been included.

Most of these materials are homogeneously broadened by interactions of the optically active ion with the phonons in the crystal. This type of broadening allows us to concentrate the bulk of the lasing energy down into a single lasing line which is particularly advantageous for Raman shifting to a particular frequency.

Table 7.4 lists a few of the many lasers in which the Nd^{3+} ion is hosted in glasses. These lasers have potential for very high power because they can be made much larger and with better uniformity than most crystals. The nonuniformity of the glass matrix induces significant broadening so that the gain bandwidth is typically an order of magnitude larger than that of similar crystalline solid state lasers. However, this type of broadening is inhomogeneous, limiting the power available in a particular

Lasers	Center Wavelength (nm)	Linewidth (cm ⁻¹)	Source
Ruby	694.3	0.53	[53]
Nd : YAG	1064.15	0.45	[53]
Nd : YAG	1318.8	0.45	[23]
Nd : YVO ₄	1342.5	1.4	[23]
Nd : YAG	532.08	0.45	[23]
Nd : YLF	1053.0	1.4	[23]
Nd : YLF	1047.1	1.4	[23]
Nd : GGG	1062.1	0.8	[23]
Nd : CeF ₃	1063.8	4	[23]
Nd : LaF ₃	1040.65	2.7	[23]
Nd : CaWO ₄	1064.9	0.8	[23]
Nd : GSGO	1061.2	1.6	[23]
Nd : YALO	930	2.6	[23]
Nd : YALO	1079.5	1.3	[23]
Nd : YALO	1064.5	1.1	[23]
Nd : YVO ₄	1062.5	-	[23]
Nd : YVO ₄	1063.4	0.8	[23]
Er : YAG	862.7	-	[23]

TABLE 7.3. High power solid state lasers

Glass Type	Center Wavelength (nm)	Linewidth (nm)	Source
Q-246	1062	27.7	[53]
Q-88	1054	21.9	[53]
LHG-5	1054	18.6	[53]
fluoroberylite	1046	19	[23]
silicate	1088	34	[23]
germanate	1063	26	[23]

TABLE 7.4. High power glass lasers

lasing line. Thus, these lasers have broad tunability, but exact a significant price in efficiency.

Table 7.5 lists the few tunable solid state lasers, all of which are based on transition metal lasing ions (Cr^{3+} or Ti^{2+}). These lasers have made significant advances in the past decade and have moved from the research lab to commercialization. They all have very broad tunability, but the central wavelengths for all of these lasers is around 800 nm, much farther from 589 nm or 1178 nm than their tuning ranges will allow. As a result, parametric or Raman frequency conversion is necessary for them as well.

Each of these materials has very different properties. Alexandrite can be lamp-pumped, but the other two are usually pumped by other lasers. Alexandrite has been used with a Raman shifting hydrogen cell (4155 cm^{-1}) as a sodium laser for LIDAR systems [20]. Sapphire and chrysoberyl (the host of alexandrite) are both much better host materials than LiSAF for high power lasers because of their excellent conductivity and high thermal fracture limit.

Ti:Sapphire lasers are becoming very common as broadband sources for femtosecond pulse generation. During the last decade they have advanced significantly so that powers of 3-4 Watts can be generated from commercially available lasers. The broad tuning band of these lasers makes them particularly attractive for tuning to a specific line. Unfortunately, the band lies midway between the sodium D_2 line and its double, forcing the use of a frequency conversion scheme and reducing the value

Laser	Center Wavelength	Linewidth	Source
Alexandrite	759	100	[20]
Ti : Al ₂ O ₃	790	180	[53]
Cr:LiSAF	850	180	[53]

TABLE 7.5. High power tunable solid state lasers



FIGURE 7.4. Combinations of solid state lasers and Raman-active materials which produce line centers near the D₂ line of sodium (light line). Combinations which make use of a single-Stokes shift, and double-Stokes shift are represented as dots, in the upper left corner. The dots to the lower right are for anti-Stokes shifts.

of its broad-band tunability.

7.2.3 Potential Combinations

The graphs in this section illustrate the potential combinations of high power lasers and Raman-active materials which result in central shifts² within 20 cm⁻¹ of the sodium D₂ line, or its double wavelength 1177.99 nm. The graphs depict Raman

²By central shift, I mean that the center of the lasing band is shifted by the amount at the center of the Raman-band.

shifts (as commonly listed in cm^{-1}) along the ordinate axis, and laser wavelengths (as commonly listed in nm) along the abscissa. The sodium D_2 and D_1 lines are presented respectively as broad and narrow yellow stripes on the graph as a reference. The shifted values of computed Stokes and second Stokes systems are plotted as red and blue dots, respectively, if they meet the 20 cm^{-1} criterion. Occasionally, an anti-Stokes shift is viable and is plotted on the graph as a green point. On many of the graphs, I have included the Raman and laser linewidths as a black ellipse centered on the dot as a guide to indicate the potential tunability of the system.

The most interesting set of candidates is the set of combinations of Raman materials with the solid state crystalline lasers seen in Figure 7.4. In the lower right corner, a few solid state lasers making use of the ${}^4F_{3/2} \rightarrow {}^4I_{13/2}$ transition of Nd^{3+} (around 1300 nm) in various hosts can be shifted to 1178 nm through an anti-Stokes shift. While they have the potential for reaching the 1178 nm wavelength required for frequency-doubling, these laser transitions are rarely as strong as the $\approx 1064 \text{ nm}$ transitions of the Nd^{3+} ion. The relative inefficiency of the anti-Stokes process in most materials also means that they are less likely to produce significant amounts of power than the other candidates shown in the graph.

Other than the anti-Stokes lines, the remainder of the candidates are principally single-Stokes conversions of the $\text{Nd}^{3+} {}^4F_{3/2} \rightarrow {}^4I_{11/2}$ transition combined with Raman-active materials exhibiting shifts of about 900 cm^{-1} , as seen in Figure 7.5. Clearly there are a number of candidate lasers and Raman materials which meet the initial wavelength criterion. This is fortunate because it allows us to choose from among a set of lasers with different power and temporal characteristics and different Raman materials exhibiting high Raman gain.

Of these candidates, we have chosen to focus on three candidate lasers, Nd:YAG, Nd:YVO₄, and Nd:YAlO₃ (also known as Nd:YAP for Yttrium Aluminum Perovskite), and two candidate Raman-active crystals, CaWO₄ and KYbW. The first two lasers were chosen because they have been extensively engineered and can reliably produce



FIGURE 7.5. Detail of first- and second-Stokes Raman processes resulting in wavelengths near 1178 nm. The ellipse centered on each dot indicates the FWHM linewidth of that particular laser in the horizontal direction, and FWHM Raman linewidth vertically.

dozens of Watts of stable, homogeneously-broadened laser power. The third laser, Nd:YAlO₃, was chosen because of its fortuitous lasing transition which, when shifted with KYbW or KGW lands closest to the sodium D₂ line. The combination of these particular materials is shown in Figure 7.6.

The 912 cm⁻¹ shift of the 1064.15 nm line of Nd:YAG by CaWO₄ puts the peak wavelength nearly midway between the two sodium lines. Since the line separation is only 8.64 cm⁻¹, it appears that the CaWO₄ shift is excessive by about 3 cm⁻¹. Shifting Nd:YVO₄ with CaWO₄ results in a wavelength that is almost equidistant to the short-wavelength side of the line. For shifting with CaWO₄, the Nd:YAP laser is not a very good candidate.

The choice of a Nd:YAG laser is excellent from a laser standpoint. The technology is mature, and has repeatedly demonstrated power levels well beyond our requirements for pumping a Raman laser. However, the 230 μsec lifetime of the Nd³⁺

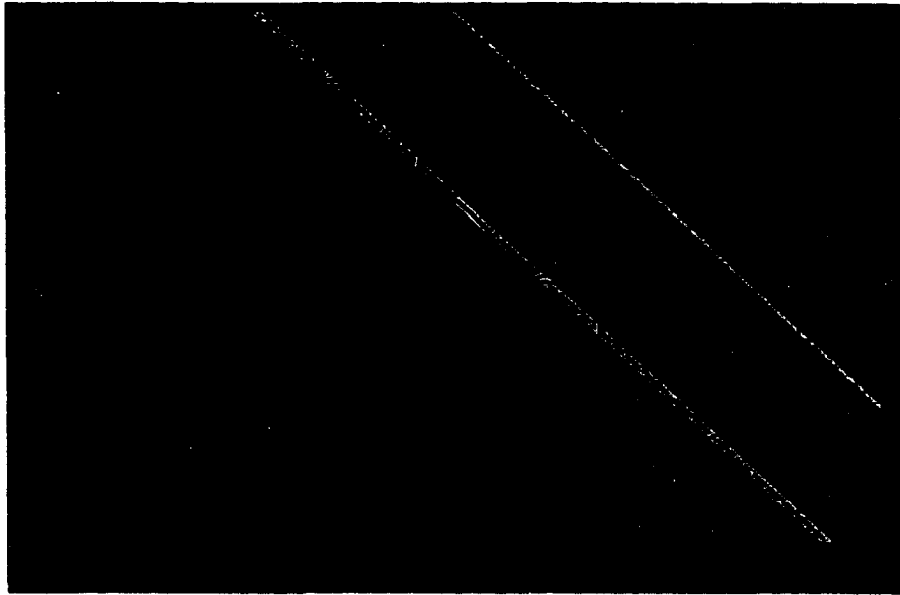


FIGURE 7.6. Shifts of Nd:YAG, Nd:YVO₄ and Nd:YAlO by CaWO₄ and KYbW.

ion in YAG means that a Q-switched system will operate efficiently at about 5 kHz, which is not very good for guide star laser operation. At a rate of 5 kHz, a Q-switched pulse of approximately 20 nsec will result in a pumping duty cycle of 10^{-4} . At even weak average power levels of 1 W the peak power of this pulse would easily saturate the central velocity classes of the mesospheric sodium distribution, resulting in a weak, inefficient guide star.

With its 92 μ sec lifetime, the Nd:YVO₄ laser can efficiently Q-switch at much higher rates. Some manufacturers claim powers of up to 40 W and Q-switch rates of 30-300 kHz with 10 nsec pulses. With duty cycles on the order of 10^{-3} or more, the option of pulsed lasers becomes more attractive.

Considering the Raman shift of KYbW, pumping with a Nd:YAG laser falls short of D₂ resonance, while Nd:YAlO is almost perfectly matched. Manufacturers [102] are claiming power levels exceeding 1 W at the 1064.5 nm line of Nd:YAlO₃ with pulse durations of < 20 nsec at 1-5 kHz. Similar to Nd:YAG, the duty cycle of this system is not very good for guide star laser production.

7.2.4 Previous Work

Raman-shifting lasers for production of coherent radiation tuned to the sodium D_2 line have been attempted by other researchers. Most of these systems were too low in power to be a viable guide star, but demonstrate the capability of SRS in production of the appropriate frequency.

An Raman laser system designed for a guide star demonstration [18] made use of an intracavity-doubled bow-tie cavity with Raman shifting performed by CaWO_4 . This system was pumped with a 5 Hz flash-lamp pumped Nd:YAG yielding 70 μsec -long trains of 350 psec micropulses at a 7 nsec repetition rate. The aggregate duty cycle of the pump laser was 1.75×10^{-5} . The average power of the pump laser was only 1.5 W, yielding a micropulse peak power of about 86 kW. They demonstrated that the Raman spectrum of CaWO_4 is *almost* ideal for shifting the 1064.15 nm output of the Nd:YAG laser to 1178 nm, where it can be frequency doubled to hit the sodium D_2 line. They found the peak of the gain to be at 589.22 nm after Raman-shifting and doubling the Nd:YAG laser. Furthermore, by using an etalon in the Raman cavity they demonstrated that the Raman gain was sufficiently broad that the lasing line could be tuned to D_2 . Their tuning curve is reproduced in Figure 7.7. They speculated that conversion efficiency in this system could be as high as 30% if the pump laser and the Raman cavity were independently tuned for maximum efficiency. The highest conversion efficiency they achieved was 14.5% for the integrated pulse, though it is not stated whether this efficiency was achieved at the sodium D_2 line or at the peak of the Raman efficiency.

Alexandrite lasers have also been developed [20] for lidar systems used to probe mesospheric sodium. The design used a high-pressure hydrogen gas cell as the Raman material ($\nu_R = 4155\text{cm}^{-1}$) for Stokes scattering to 1178 nm from a starting wavelength of 791 nm, or for anti-Stokes scattering directly to 589 nm from a starting wavelength of 780 nm. Unfortunately, alexandrite lasers of more than a few hundred mW are not

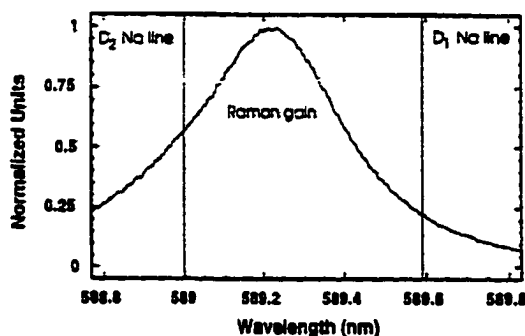


FIGURE 7.7. Gain curve of the TRW Raman laser showing gain as a function of intracavity tuning.

available, so while Raman scattering for LIDAR measurements may be possible with this system, development of an effective guide star are not.

Recently high-finesse cavities have been successful in generating CW Raman lasers operating with 61% photon conversion efficiency [87]. These lasers make use of the Raman shifting of diode laser output at 792 nm in a high pressure Raman cell capped by high reflectivity mirrors. The output at 1180 nm was very close to the frequency-doublable 1178 nm goal. Only 14 mW of power was achieved, but both Raman conversion efficiency and Raman output power are expected to increase with greater pump power. Wide tunability of such lasers has also been demonstrated [65] by using an external cavity diode laser as the source for the Raman laser. In this configuration less than a mW was attained, but continuous tuning from 1174 nm to 1214 nm was demonstrated.

7.3 CaWO₄ Raman-shifted Laser Experiments

7.3.1 CaWO₄ Shifted Nd:YAG

CaWO₄ has a scheelite crystal structure, consisting of 12 atoms per unit cell. The structure is a body-centered tetragonal array with C_{4h} symmetry. This symmetry

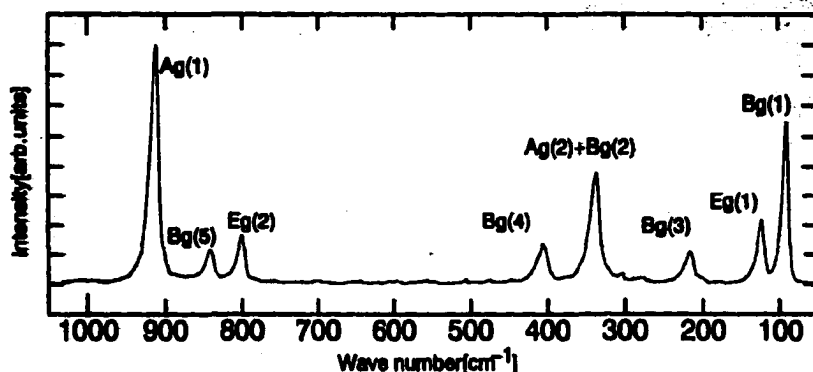


FIGURE 7.8. Raman spectrum of CaWO_4 after [103]. Relative scattering intensity is indicated by the height of each peak, and frequency shift (*i.e.* phonon energy) is indicated in cm^{-1} on the abscissa.

group can be decomposed into direct products of the C_4 and C_i symmetry groups [40]. The former of these is composed of irreducible representations A_1, B_1 and E , the last of which is two dimensional, and thus doubly degenerate. The existence of the C_i group implies that each of the former representations will exist in a direct (*gerade*) and indirect (*ungerade*) form, for a final breakdown of irreducible representations of $A_{1g}, A_{1u}, B_{1g}, B_{1u}, E_g$ and E_u . Of these the *gerade* representations have significant third order electric susceptibility, and are thus Raman-active [12].

The Raman spectrum for CaWO_4 is shown in Figure 7.8 from Suda and Sato [103] with the Raman lines identified according to the representations just described. At room temperature, the strongest line is the A_{1g} line at 912 cm^{-1} (identified in the text of [103]).

Because of our need to precisely center the laser at the peak of the sodium D_2 line, we must be very careful to properly match the accurate laser wavelengths to an accurate Raman shift. In the case of CaWO_4 , this is somewhat problematic because of the general disagreement of the value of this shift found in the literature. The Raman spectrum of CaWO_4 , specifically the energy of the A_g line, has been measured by different groups, with significantly different results. An early spectrum reported

in Eckhardt [26] put the shift at 911 cm^{-1} , although the paper indicated that the uncertainty in the shift may be as large as $\pm 10\text{ cm}^{-1}$. As mentioned above, Suda and Sato [103] identified the energy as 912 cm^{-1} . The measurement of Desgreniers, *et al.* [24] likewise placed the value at 912 cm^{-1} . Recent measurements by Kaminskii, *et al.* [50], place the value at 908 cm^{-1} , while Basiev *et al.* [10] places the line at 910.7 cm^{-1} , claiming a spectral resolution of 0.2 cm^{-1} . In fact, Kaminskii *et al.* claim development of an efficient (40%) all-solid-state laser based on PbWO_4 operating at 1177.0 nm for a harmonic of a sodium laser, though no specifics are given. Furthermore, they claim the production of light at 1178.0 nm based on their reported 908 cm^{-1} shift in CaWO_4 .

To reach the sodium D_2 wavelength, not only must the frequency of the Raman shift be known accurately, but the wavelength of the pump laser must also be known accurately. According to Koechner [53] the dominant lasing transition of Nd:YAG occurs from the ${}^4F_{3/2}$ line to the ${}^4I_{11/2}$ line with a wavelength of 1064.15 nm in air (energy of 9397.2 cm^{-1} in air).³

To determine the required Raman shift, we can subtract half the wave number of the sodium D_2 line (8489.04 cm^{-1}) from the Nd:YAG pump line (9397.17 cm^{-1}) to get a required Raman shift of 908.13 cm^{-1} . The most common wavelength shift cited for CaWO_4 is 912 cm^{-1} which is rather far from the required shift. Because of the variations in the measured A_g line of CaWO_4 we decided to measure the shift ourselves [89]. We set up the laser diagrammed in Figure 7.9. A fiber-coupled set of laser diodes emitting at 808 nm axially pumped a 22 mm long Nd:YAG rod, housed in a copper cooling block. The pump power of 5.11 W generated a CW lasing power of 1.95 W at the nominal 1064 nm line of Nd:YAG. Then the YAG laser was Q-switched to obtain high-intensity pulses required to stimulate the nonlinear processes. The CaWO_4 Raman-shifting crystal was inserted in the cavity as shown to generate the Raman wave. The Raman output was then frequency doubled and fed into an optical

³All energy values and wavelengths quoted in this work will refer to air, unless otherwise specified.

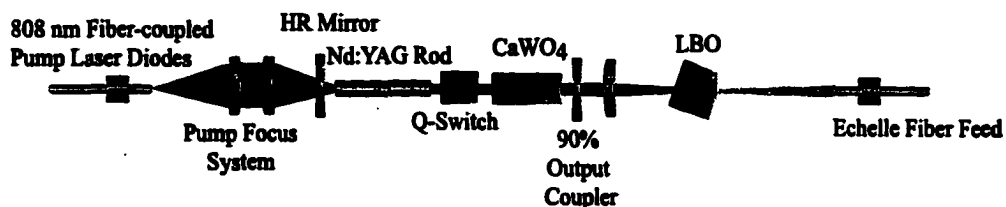


FIGURE 7.9. Experimental setup for establishing Raman shift of CaWO_4 pumped by a Q-switched Nd:YAG laser. The output of the single Stokes shift was doubled using LBO and fed into an optical fiber leading to a high-resolution echelle spectrograph.

fiber running to the slit of a high-resolution echelle spectrograph.

The output of the spectrograph during the experiment is shown in Figure 7.10, in which the slit elongation is horizontal and increasing wavelength is toward the top of the figure. Slightly left of center one sees the sodium lamp reference, split into the D_1 line at the top and the D_2 line at the bottom. The separation of these two lines is almost exactly 6.0 \AA (17.28 cm^{-1}) [78]. The fiber input is on a vertical line just to the right of the spectrum of the reference source, showing the Raman-shifted and frequency doubled output of the laser. The shift of CaWO_4 unfortunately lies nearly midway between the D_1 and D_2 lines. Using the peaks of the sodium lines as a reference, the center of the emission is at $589.25 \pm 0.05 \text{ nm}$. With the output wavelength of Nd:YAG peaking at 1064.15 nm , then the measured shift of the CaWO_4 crystal was 911.8 cm^{-1} .

The spectral width of the gain of Nd:YAG pump laser (about 4 cm^{-1} [53]) barely allows for tuning of the pump laser to shift the doubled output to the sodium D_2 line. However, in doing so there is a significant price to pay in the output of the Nd:YAG pump laser. This power loss is exacerbated by the further reduction in Raman conversion efficiency associated with the reduction in pump intensity.

Varying the shift of the CaWO_4 Raman crystal was also considered. In theory, minor changes in the temperature and pressure environment of the crystal can have

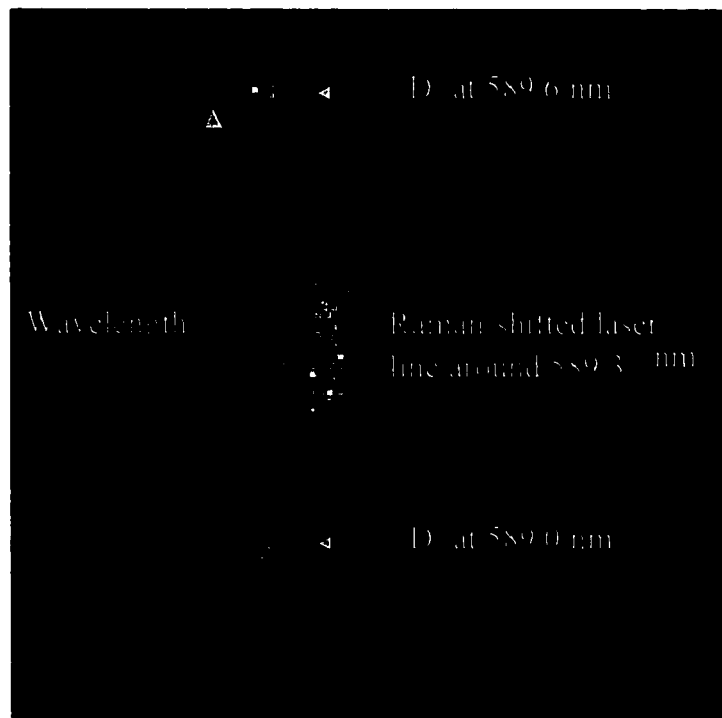


FIGURE 7.10. Echelle spectrograph output comparing Raman-shifted and doubled output of Nd:YAG (right) against D_2 at 589.0 nm (bottom) and D_1 at 589.6 nm (top) lines of sodium reference source. Dispersion of the spectrograph is such that the up direction is longer in wavelength.

a slight effect on the Raman energy, but perhaps enough to affect the required shift. These effects were studied by Desgreniers *et al.* [24], who found that the high frequency Raman active modes are relatively little affected in frequency. The frequency shift of the Raman peak with temperature appears to follow a line of

$$\frac{d\nu}{dT} = -0.0030\text{cm}^{-1}/\text{K} \quad (7.12)$$

which implies a thermal change of roughly 1200 K to achieve line center at the proper Raman shift of 908.3. The required change in pressure is 26 Kbars, also beyond consideration.

A different conclusion was reached by Banishev *et. al* in which they shifted the A_g line of the CaWO_4 Raman spectrum from 912 cm^{-1} to 901 cm^{-1} in going from $T=273\text{ K}$ to $T=1473\text{ K}$. Assuming a linear shift, a temperature of over 500 K would be required to center the Nd:YAG output at 1178.0 nm. In doing so, the spectrum of the CaWO_4 shift would broaden significantly, reducing the Raman gain.

Because of the uncertainty, inefficiency and difficult associated with changing the Raman shift in CaWO_4 , we decided that the best way of shifting the laser to the sodium D_2 peak is to alter the wavelength of the pump laser. This has the advantage of operating near the peak of the Raman gain in the Raman cavity, resulting in a significant increase in conversion efficiency within the Raman laser.

7.3.2 CaWO_4 Raman-shifted Nd:YAG

To effect a room-temperature shift of Nd:YAG to a wavelength which would allow us to take full advantage of the CaWO_4 gain, we considered methods of changing the composition of the YAG host material to shift the energy lines of the Nd^{3+} ion. Changes in composition alter the bond strengths and lattice parameters of the crystal, perturbing the wavefunctions and energy levels of the optically active electrons doping the crystal. By changing the energy levels, the resonance energies of the electrons are also changed.

The number of different ions that can be used in compositional tuning is rather limited however. The resulting crystal must hold true to the general rule of rational composition, in which the composition of the crystal must be ratios of integers. The substitute atoms must be of the same valence as the substituted atoms, and must be nearly the same 'size'. Finally, the overall crystal structure must be flexible enough to accommodate slight variations in the lattice parameter that arise from the substitution.

Gallium meets these requirements for a substitute for aluminum in the YAG structure. Both atoms are in the same periodic group, and consequently it is not surprising that they both prefer the same valence of -3. Situated in the group just below aluminum, gallium is a reasonable candidate to consider because of ionic size. In the garnet structure, pure $\text{Y}_3\text{Al}_5\text{O}_{12}$ has a lattice constant of 1.201 nm, while pure Yttrium Gallium Garnet (YGG) $\text{Y}_3\text{Ga}_5\text{O}_{12}$ is very near that at 1.228 nm [7].

It was previously reported [108] [7] that by replacing some of the aluminum in YAG with gallium, the crystal field is altered to the point that the various ${}^4F_{3/2} \rightarrow {}^4I_{11/2}$ transitions of Nd^{3+} will be shifted to slightly lower energy. Specifically, the line giving rise to the highest branching ratio of the Nd:YAG laser (often listed as the $b \rightarrow 3$ line because it goes from the higher (b) of the two ${}^4F_{3/2}$ lines to the third (from the lowest energy) of the ${}^4I_{11/2}$ lines. The energy of the transition shifts from 9398 cm^{-14} to 9413 cm^{-1} for complete replacement of Al with Ga. To first order, we anticipate the relative amount of shift to be linear between these two values, and interpolating we can derive a target aluminum replacement value. If we add the measured 912 cm^{-1} Raman-shift of CaWO_4 to the desired final energy value of 8489.04 cm^{-1} (relative to vacuum) we obtain a desired vacuum referenced energy difference of 9401.04 cm^{-1} , or 1063.71 nm in air.

⁴Watts and Holton [108] cite different energy values for the energies of the ${}^4F_{3/2}$ lines than more recent books. Indeed, their values appear to be more in line with spectral observations than the lines listed in the aforementioned texts.

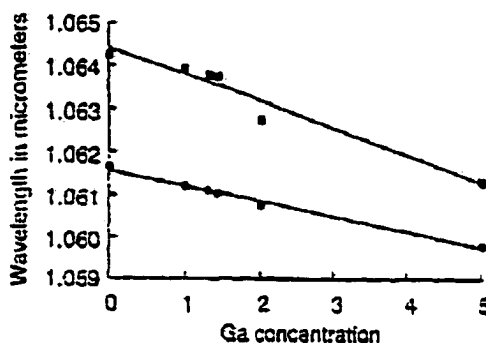


FIGURE 7.11. Lasing wavelengths of host crystals with varying concentrations of Ga replacing Al in YAG. The value of x is the mean number of Al atoms replaced with a Ga atom per unit cell (after Barnes [7]).

The properties of the spectral lines in crystals of $Y_3Ga_xAl_{5-x}O_{12}$ (YGAG) with low x values were reported by Barnes [7]. The results of that study for the 1064.15 nm line of Nd:YAG are shown in Figure 7.11, in which an increase in the percentage of Ga replacing Al shifts the lasing line discernably toward higher energy (shorter wavelength). Interpolating the tuning line to obtain a wavelength of 1063.71 nm results in a desired x value of about 1.1. The Barnes study indicated that the lifetime and emission cross-section of the Nd^{3+} ion remained relatively unchanged over the various x values that they experimented with.

Based on this, we had a crystal of Nd:YGAG grown with a target replacement value of $x = 1.1$. From the clearest portion of the YGAG boule we had a laser rod 22 mm long and 3 mm in diameter made. We observed the bright emission of a sodium lamp through the YGAG rod and it looked clear and uniform. We also used the sodium lamp as a background source for observing birefringence. In this case, a pair of linear polarizers was oriented to completely extinguish the sodium light. The laser rod was then placed between them, and complete extinction was maintained, indicating a lack of birefringence. The rod was then mounted in a copper heat sink and inserted into the lasing cavity used for the previous Raman-shifting experiment.



FIGURE 7.12. Echelle spectrograph output comparing Raman-shifted and doubled output of Nd:YAG (right) against D_2 at 589.0 nm (bottom) and D_1 at 589.6 nm (top) lines of sodium reference source. The peak of the transition is at 589.06 nm.

There was considerable difficulty getting power out of the Nd:YAG cavity with the Q-switch in place. The Q-switch insertion loss in the previous Nd:YAG laser was only about 4% (with no RF power applied to the unit), and introduction of the CaWO_4 crystal reduced the value by another 4%, for a total insertion loss of only 8%. In contrast, insertion of the AOM in the cavity beam of the Nd:YAG laser reduced the power by slightly more than 25% (again, with no RF power). Operating the laser Q-switched resulted in a maximum average power of 0.49 W at 10 kHz.

The spectral result of the Raman-shifted and doubled Nd:YAG lasing rod is shown on the echelle spectrograph output in Figure 7.12. Although significantly weaker, the center of the lasing action is clearly shifted much closer to the D_2 line, peaking at 589.06 nm. By centering the Raman gain there, the Raman laser can be operated near the peak of the Raman gain curve such that tuning to sodium resonance

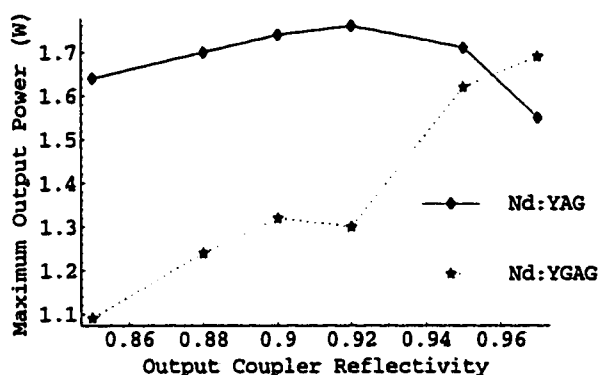


FIGURE 7.13. Curves for Nd:YAG and Nd:YAGG showing output power varying with output coupler reflectivity. The peak of the curve is an indicator of the gain of the system. Peaks at lower reflectivities generally imply more gain. Note that the Nd:YAGG curve continues to increase beyond the highest reflectivity output coupler, indicating low gain in the rod.

can be performed with very little loss of efficiency.

This laser was somewhat lower in power than the Nd:YAG laser previously developed. The highest CW power achieved with this laser was 1.83 W, about 87% of the amount obtained with the Nd:YAG crystal in the same configuration. This was achieved with an output coupler with a reflectivity of 97%, higher than the optimum 92% for Nd:YAG and a strong indication that the gain of the YGAG rod may be significantly lower than that of the YAG rod. To investigate this, several different output couplers were used as end mirrors in the cavity. For each, the cavity was optimized (for the same cavity lengths) and the maximum stable output power was recorded. This experiment was performed using both YAG and YGAG as the lasing crystals. The resulting data in Figure 7.13, known as a Rigrod plot, shows a peak power for Nd:YAG at an output coupler reflectivity of 92%. The output of the Nd:YAGG increases on a steep curve, even at reflectivity of up to 97%, indicating that the laser is probably still overcoupled at this point (*i.e.* a reflectivity of greater than 97% is required to optimize the power). Since the 97% output coupler was the highest reflectivity OC available, an accurate Rigrod analysis cannot be completed.

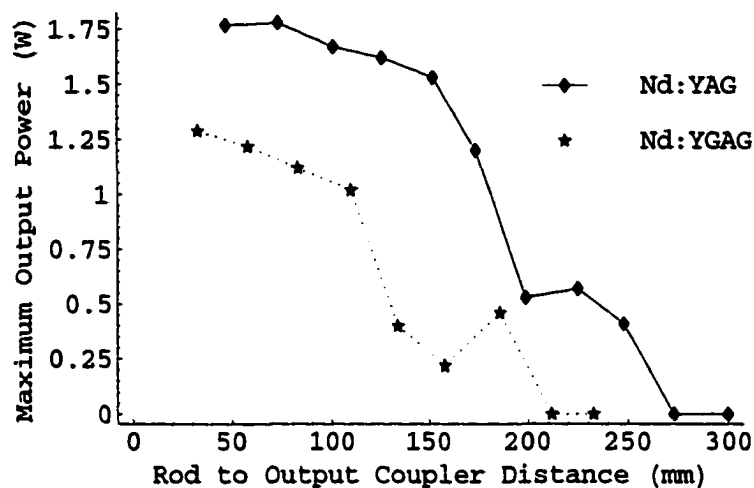


FIGURE 7.14. Maximum attainable power for a 92% output coupler at varying distances from the lasing rod. The curves were obtained for 5.11 W input pump operating CW in the cavity. The last three data points for the Nd:YAGG curve were very unstable.

However, we can make some qualitative observations.

The Rigrod analysis is closely related to the gain and losses in a laser system. It is easiest to understand the type of curve expected from an analysis of the end points. At the low coupling end of the curve, the high transmission of the output coupler does not recirculate enough power to maintain a high efficiency of stimulated emission. As a result, most of the excited atoms decay through spontaneous emission, and little power results from the laser. At the other end, if the reflectivity of the output coupler is very high, it does not allow much of the light out. Thus, low power results. In addition, the recirculating power in the cavity becomes very high, causing other losses such as scattering and diffraction to grow to limit the buildup within the cavity.

For this set of measurements, all parameters were identical, with the exception of the lasing rod. Thus, there is no opportunity for extra losses to interfere with the lasing. Clearly, a laser rod with lower gain will require more recirculation through the cavity to maximize the stimulated emission output. There is also the possibility of

different thermal effects changing the cavity configuration between the two laser rods. If the dn/dT or coefficient of thermal expansion of the two materials are appreciably different, then the cavity mode could be seriously affected. This could have the effect of increasing the losses (especially diffraction losses) in the cavity, or changing the mode volume of the laser. In the latter case, only the Nd^{3+} ions within the mode volume are capable of contributing to the lasing action, so a change in mode volume can have a very great effect on threshold power and output efficiency. To investigate whether this was the case, both the YAG and YGAG maximum attainable power values were recorded for varying cavity lengths. The results of this experiment are seen in Figure 7.14. The last three points for the Nd:YGAG curve were in a lasing condition in which the output power was unstable. The values shown are for the highest recorded power. Note that the power drops off at shorter cavity lengths for the Nd:YGAG rod, an indicator of the thermal effects mentioned above. This laser clearly needs to operate over short lengths, or have a correcting lens inserted for operating at higher powers. This presents a problem, since operation will require AO modulators and a long intracavity Raman-shifting crystal.

This improvement has not been without cost, however. As seen in Figure 7.15, there appear to be two more lines shifted another 0.30 and 0.37 nm shorter in wavelength at 588.76 nm and 588.69 nm. This is troubling because a substantial fraction of the energy of the laser is directed into lines which are too close to the desired transition to remove by reducing the feedback, and too far to be useful in Raman-shifting to the intended line. More importantly, it indicates that the material is probably inhomogeneously broadened. This has far-reaching implications in that the power in the non-resonant spectral parts of an inhomogeneously broadened transition is not available to the remainder of the spectrum. Thus, the laser is most likely seriously limited in power at the 1063.7 nm transition of interest to us. Barnes *et al.* noted that there was a likelihood of inhomogeneous broadening in the sample study they reported. This should be somewhat expected from a compositionally tuned laser.

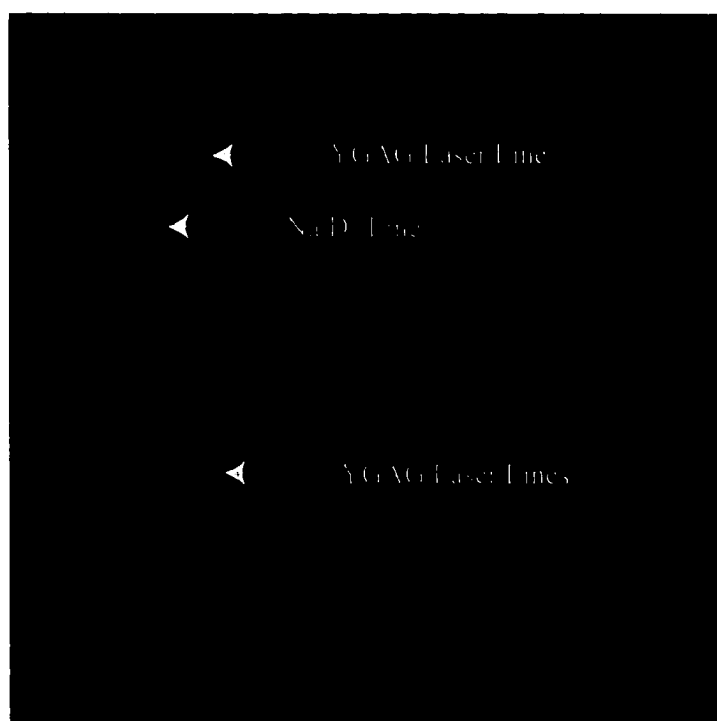


FIGURE 7.15. The Nd^{3+} lines have been broadened considerably by the introduction of extra Al in the melt. The laser also appears to be inhomogeneously broadened with multiple lasing transitions.

The optically active Nd^{3+} ion can go into a site that is coordinated with four aluminum atoms, as in YAG or a site with some aluminum and some gallium. Nd ions in each of these sites would experience different crystal fields, and thus, different energy splittings.

The bright line observed in Nd:YAG is at 1064.15 nm, and appears asymmetric in the spectra because it is actually two separate lines [23]. These two lines are the two nearly-degenerate lines in Nd:YAG that simultaneously give rise to the bright emission at 1064.15 nm and are separated significantly by the new YAG host.

7.4 Conclusion

The guide star laser requirements for tunability to the sodium D_2 line and high duty cycle are relatively difficult problems for solid-state lasers based on rare earth lasing ions to overcome. These ions have very specific, narrow energies in which the optically active electrons resonate, and the outer electrons of the ion screen the external field so strongly that externally induced perturbations are quite limited in scope and magnitude.

The need for high lasing duty cycle to avoid saturation of the sodium layer is also counter to the nonlinear optical techniques required for shifting or tuning the laser to an appropriate wavelength. All of these nonlinear techniques are effective only at very high intensities where the nonlinearities in materials begin to produce noticeable effects. The product of $I_p L$ in the exponent of the gain equation is constant under free-space optical conditions; the intensity I_p can be increased by focussing the pump light using a lower focal ratio, but the interaction length L then decreases by the same ratio, resulting in no improvement. The pump light can be refocussed repeatedly through multiple stages of nonlinear material, but this introduces alignment difficulties and multiple surfaces which add sources of loss. The most common method of raising the nonlinear gain of a system is by Q-switching, which allows the instantaneous intensity

to be increased by orders of magnitude.

Development of a solid-state laser for an effective guide star laser requires a fair amount of luck: in finding the right combination of materials that will produce the correct lasing wavelength, yet has the right combination of high gain and power scalability to operate as a guide star. One such 'lucky' occurrence is the combination of the 1064 nm and 1319 nm lines of Nd:YAG, in which the frequencies of the two lines sum to produce 589 nm directly.

We have shown that several potential combinations of high-power solid state lasers and Raman-active materials exist for producing light near the 1178 nm frequency required for doubling to 589 nm. For each of these combinations though, there must be sufficient tunability to hit the very narrow 3 GHz (0.0036 nm) D_2 line. The narrowness of the line also demonstrates the need for homogeneously broadened lasing materials because of the need to concentrate as much of the lasing energy in this narrow band as possible. For materials like inhomogeneously-broadened Nd:Glass the roughly 30 cm^{-1} (3.4 nm) broadening implies that only about 0.1% of the lasing power can be made useful, which is terribly inefficient, if not completely impractical.

Of the various laser-Raman combinations which might work, we have experimented with the combination of diode-pumped Nd:YAG and CaWO_4 , measuring the Raman shift at 1064.15 nm to be 911.8 cm^{-1} . By doubling the first-Stokes light output of the Raman laser we showed reasonably high Raman conversion and doubling efficiency, though the output would still require intracavity tuning to narrow the output spectrum and center it on the sodium D_2 line.

The output light consisted of 20 nsec pulses at 5 KHz, for a duty cycle of 10^{-4} . At 0.5 Watts average output power, this translates to pulses of 50 kW, well above saturation for the sodium layer, and of little value by itself in production of a guide star. For such pulses, the loss associated with tuning and narrowing the lasing line would not be noticed, affording the possibility of temporally interleaving multiple lasers. Pumped by QCW diode bars, such lasers could be produced in quantities of a

few dozens relatively inexpensively, and combined could operate at hundreds of kHz, linearly increasing the guide star brightness by the number of lasers.

Attempts to tune the pump laser by changing the composition of the host material were successful in shifting the lasing lines from 1064.15 nm to 1063.8 nm. However, the power of the new laser, especially the Q-switched power output, was significantly lower. Q-switching seemed to work best at a frequency of 10 kHz, faster than that of Nd:YAG. However, the output of the compositionally tuned laser was substantially broadened, apparently inhomogeneously so, further limiting the potential of this laser to produce a viable guide star.

While the efforts at generating Raman-shifted pulses were largely successful, an improved method must be found of generating the 1178 nm wavelength which does not suffer from the tuning inefficiency of tuning from the nominal 1064.15 nm Nd:YAG line. This method must still be capable of producing significant power, and maintaining homogeneous broadening of the laser for spectral concentration at the narrow sodium D₂ line.

Chapter 8

THE COLD ND:YAG LASER

8.1 Background

Many of the concepts explained in this work depend on a reliable, high power, homogeneously broadened laser source as an input. Since the mid 1960's the Nd:YAG laser has been a solution for high power, high energy, narrow-line pumping of other lasers such as dye lasers and tunable Ti : Al₂O₃.

The properties of YAG make it an excellent host for the Nd³⁺ ion; it has cubic structure (*O_h* symmetry) which maintains the isotropic field about the Nd³⁺ ion promoting level degeneracy and thus, high gain. The Nd³⁺ ion has a moderately long lifetime in YAG (230 μsec) allowing for high energy pulses through rapid Q-switching at a few KHz. YAG is very hard (Knoop hardness of 1215), and can be grown in relatively large sizes with excellent optical quality. The Nd³⁺ ion can easily replace a Y³⁺ ion in the structure, minimizing lattice strain and eliminating the need for charge compensation. YAG has moderate thermal conductivity, allowing for effective heat removal.

Some of these very properties that make Nd:YAG such a popular high-power solid state laser also result in difficulties for our task. In developing a solid-state laser as a pump source for a Raman system, the operating frequency of the pump laser is just as important as the shift frequency of the Raman material. Unfortunately, the lasing transitions of Nd³⁺ in YAG result in a principal transition wavelength of 1064.15 nm, which is shown to be somewhat off-peak for a CaWO₄ Raman laser. Furthermore, the shielding of the optically active 4f electron by the outer 6s electron makes the lasing wavelength very difficult to alter.

In most laser systems employing Nd:YAG, this is not a major cause of concern.

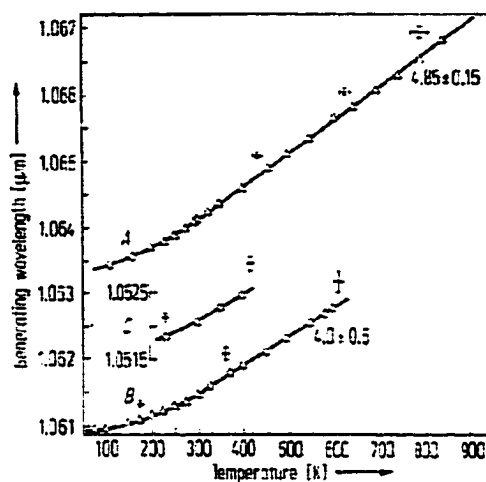


FIGURE 8.1. Shift of various lasing transitions as a function of temperature, after Kaminskii [49]. The temperature for centering the main line of Nd:YAG at 1063.71 nm is approximately -70 C.

Absorption transitions in other optically active systems such as laser dyes or Ti:Al₂O₃ lasers are often broad, so tuning of the Nd:YAG laser is rarely necessary. Some LIDAR systems occasionally make use of fine tuning control, but these are rarely of the high power needed by a guide star system, so tunable lasers and inhomogeneously-broadened lasers will usually suffice.

As discussed in the previous chapter, the energy levels of lasing ions and their associated energy transitions will generally vary as the external environment in which the ion resides is varied. In that case we changed the composition of the host crystal which had a resultant effect on the energy of the lasing transition of interest. Another way of changing that environment is to vary the temperature of the host crystal. Qualitatively, as the crystal is cooled the lattice parameter tends to shrink slightly and the crystal ligands come closer to the lasing ion, influencing the energy levels accordingly.

The shifts of the energy levels of rare-earth ions are minor because of the shielding of the optically active $4f$ electrons from the external crystal field by the outer $6s$

electron. As a result, relatively drastic temperature changes are required to effect even small shifts such as the one required when Raman shifting with CaWO_4 . The degree of shifting required is shown in Figure 8.1 from Kaminskii [49], from which we can interpolate that the proper wavelength should obtain at a temperature of approximately -70 deg C. Power levels were not reported in these lasers, and since power was not the objective of the studies we do not anticipate that they were very high.

8.2 Design

The design of a high-power thermally-tuned Nd:YAG laser poses much more difficult engineering problems than those encountered in the design of room-temperature Nd:YAG lasers.

Recent literature covering the development of high-power lasers reveals many cases in which researchers have developed moderate- to high-power slab lasers [97] [21] [6] [37] [107]. Most of the early slab lasers were liquid cooled, requiring the use of O-ring seals for isolation of the cooled areas from the lasing faces. Maintaining constant uniform crystal temperature in these lasers required the design of complicated plenum chambers to control the flow and mixing of coolant. Some of these designs appear to require more expertise in plumbing than optics, and though they were reported to have success in achieving high power, reliability and maintainability was rarely addressed.

In recent years conductively cooled slab lasers have been designed which remove internal heat through solid-solid contact, minimizing the effort involved in development, fabrication and maintenance of the laser heads. For most such lasers, the goal of the heat removal assemblies is to maintain a constant temperature, or at least to minimize rise above nominal room temperature during laser operation. By keeping the system close to room temperature, differential expansion of materials in the con-

duction system is not a problem, allowing the designer to focus on the goal of efficient heat transport.

Developing a zigzag slab laser to operate stably and efficiently at low temperature increases the difficulty of the problem considerably. First, the entire lasing system must be housed in a thermally and atmospherically controlled environment. Thermal isolation is required to reduce the load on the cooling unit and allow the system to stabilize at very low temperature, while atmospheric isolation is required to limit heat input and to prevent water vapor from condensing on the laser crystal. Optical effects like thermal-stress induced birefringence, pressure-stress birefringence and thermal lensing resulting from temperature nonuniformities in the YAG crystal must be ameliorated for the system to operate at high power. Finally, a method for rapidly and efficiently conducting heat from the YAG crystal must be developed which can continuously operate over a range of temperatures. These difficulties are especially challenging because of the requirement for the system to be thermally-cycled over wide temperature ranges thousands of times.

8.2.1 Zigzag Slab

In common end-pumped cylindrical YAG rods, a radial thermal gradient develops from the preferential deposition of heat from axial pumping of the rod. Each of the absorbed pump photons at 808 nm results in a single lasing photon (under the best of circumstances) at 1064 nm. The remaining energy is deposited as non-radiative losses (heat) into the laser crystal. Fortunately, YAG has good thermal conductivity, allowing the heat to be transported quickly from the rod. Nevertheless, in steady state the system develops a predominantly radial gradient in temperature which results in two 'focusing' effects and one polarization effect. The focusing effects are (1) the differential thermal expansion of the YAG, bowing the flat end surfaces into lensing surfaces, and (2) the increase in refractive index with temperature inducing a slight



FIGURE 8.2. Operation of a zigzag slab laser. The cavity beam enters the slab through the Brewster surfaces on the ends. The beam is refracted toward the TIR surfaces at the top and bottom of the slab where lossless reflection occurs. Because of uneven pumping and cooling through the top and bottom faces, a thermal gradient is established with a maximum at the center of the crystal. However, each portion of the beam propagates equally through each temperature zone, minimizing the thermal distortion to the beam.

gradient index lens throughout the long laser rod. The end result is a pronounced positive lensing effect which increases with laser power. Because the effect varies with power, it is difficult to correct with a fixed optical system. The polarization effect results from a stress-induced birefringence coming from the axial stress in the rod due to uneven heating. This causes a rotation of the lasing polarization which results in significant loss at the polarizing Brewster surfaces.

Slab lasers were developed to minimize these thermal effects. The zigzag slab shown in Figure 8.2 is used in the Guide Star pump laser. It is designed so that an incident planar wavefront enters the slab through a Brewster surface, and is refracted toward the polished lower surface of the slab. There, because of the high refractive index of YAG ($n_{YAG} = 1.82$), the wave experiences total internal reflection directing it toward the upper parallel surface. Reflections from these parallel surfaces efficiently guide the wave to the far end of the slab, where refraction through the second Brewster surface occurs, and the planar wavefront continues on in free space. The length of the slab is chosen so that a longitudinal ray exits the second Brewster surface at the same point where it was incident of the first Brewster surface. The result is that all portions of the laser wavefront travel through all temperature zones of the laser crystal equal amounts, minimizing any thermal distortion to the wavefront.

Cooling of the YAG slab must be performed principally through the TIR surfaces

of the laser so that the thermal gradients established are predominantly uniform with respect to different parts of the propagating beam. Cooling through the non-TIR surfaces would establish a gradient in which the wave propagating close to these surfaces would experience less retardation (because of the cooler temperatures) than those near the center of the slab. As described above, this leads to thermal lensing effects which we wish to minimize.

Pumping the YAG slab may be done either by pumping through the TIR surfaces, or through the non-TIR surfaces on the sides of the laser slab. Earlier pump systems pumped through the TIR faces of the slab, for the same reason that cooling is preferred on these surfaces. In this case, the designs use liquid cooling in which the cooling fluid is in direct contact with the slab TIR surfaces. The much lower refractive index of the cooling fluid (usually deionized water running well above the freezing point) does not spoil the TIR of the slab surfaces, and is transparent at the pump wavelengths to allow for transmission into the YAG crystal. This necessitates a rather large amount of engineering in and of itself. The cooling area must be completely sealed with O-rings from the Brewster surfaces of the slab, and some kind of thin, transmissive window (often sapphire) is usually placed along the top of the fluid channel to protect the pump source from the cooling liquid. As a result, the pump source must pump through several surfaces and materials before reaching the laser gain material.

Cooling is a surface effect, necessitating that it be performed preferentially on the TIR surfaces, as previously noted. In contrast, the absorption of the laser power occurs throughout the volume of the laser crystal, opening up the potential for pumping the sides of the laser slab which are parallel to the plane of propagation of the lasing wave. By pumping from both sides of the slab, near-uniform volumetric heat generation can be obtained throughout the laser slab, reducing the cylindrical lensing effects which might otherwise be associated with side-pumping. By pumping other surfaces than the cooling surfaces, conductive cooling with high-conductivity solid materials is possible, which eases the engineering burden and maximizes the effectiveness of

conduction cooling.

The principal loss associated with side pumping is the need to pump through the roughened side surfaces of the slab. They must be roughened to spoil parasitic losses (gain-robbing laser oscillations propagating along directions that are not consistent with the main laser cavity). With smoothly polished surfaces, AR coatings could be applied to the surfaces to enhance the absorption of the pump radiation; with ground surfaces this is not possible.

8.2.2 Cooling Assembly

Our approach to cooling the YAG surfaces was quite different from this conventional design. Instead of pumping through the TIR surfaces, we chose to pump through the side surfaces, and conduct heat through the TIR surfaces by direct contact to a conducting medium. The engineering associated with this was expected to be simpler and lower in risk by isolating the cooling fluid from the YAG slab. This minimizes the risk of contamination of the Brewster surfaces, and reduces the complexity associated with the O-ring seals which must isolate the liquid from the external environment over a wide operating temperature range, and the development of efficient plenum chambers needed to get even cooling across the top surface of the small YAG slab. Nevertheless, this design entails its own difficulties in development which we managed to solve quite successfully.

The final working design of the cooled YAG slab is seen in Figure 8.3. Because the cooling fluid must have the ability to flow at very low temperature (-70 deg C) we used methanol, cooled in a reservoir by a primary chiller. To boost the cooling power, we inserted the probe of an immersion cooler which is capable of reaching -90 deg C at no thermal load. The chiller probe was inserted into a specially developed cover for the primary chiller. Using this system, we managed to get the temperature of the reservoir of cooling fluid down to -40 deg C at full laser pump power. Measured

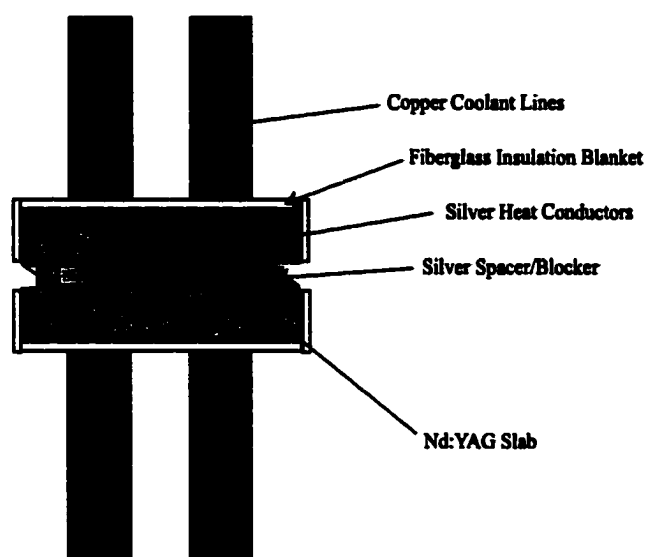


FIGURE 8.3. Detail of assembly for supporting and cooling the zigzag laser slab. Coolant was conducted through the copper lines into a channel cut through the silver cooling assemblies. Contact between the silver and laser slab was maintained by a layer of pure indium. The silver blocking pieces were to hold the slab laterally in place and prevent illumination of the slab ends by the pump diodes.

at the Nd:YAG laser slab, the lowest attainable temperature was -21.5 deg C during operation. The cooling fluid ran through insulated lines to the laser box where they were connected to small copper tubes, which were in turn soldered to special nickel bellows. These bellows function well at low temperature and allow some flexibility in the adjustment and assembly of the system. The thin walls of the bellows and relatively low thermal conductivity limited the heat flow into the coldest parts of the laser. The bellows were in turn soldered to the main cooling apparatus, a sterling silver contact assembly. The silver serves two functions: first, it has extremely high thermal conductivity for transferring heat from the slab to the cooling fluid, and second it has excellent reflectivity in the near infrared for channeling the pump laser light into the laser crystal. The silver contact assembly was made of three thick plates of sterling silver soldered together by Warren Davisson. The bottom plate was a solid rectangle for conducting to the YAG slab, while the middle plate had an elongated

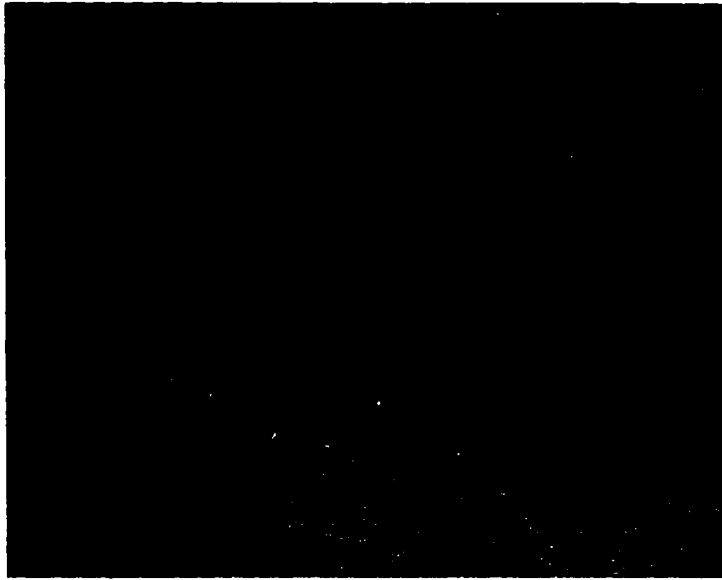


FIGURE 8.4. Photo of silver cooling pieces soldered to bellows and copper coolant lines.

channel cut through it through which the coolant flowed. The top plate had two holes cut into it at the ends of the conducting channel for connecting to the nickel bellows. The contacting surfaces of the silver contact assemblies were polished to a bright, specular mirror finish using jeweler's rouge as shown in Figure 8.4.

8.2.3 Indium Contacting

The naked silver contact assemblies cannot maintain good contact without the YAG slab; the relative inflexibility of both materials makes it likely that they will only contact in a few small places across the slab, so direct thermal contact cannot be guaranteed. Furthermore, the high degree of mismatch in the thermal expansion coefficients creates significant stresses in the YAG if both materials are rigidly fixed with respect to one another. A thin layer of highly malleable material is required to establish and maintain the thermal contact. After reviewing the options, pure indium was chosen to maintain the contact; it has good wetting properties, flows at the lowest design temperatures (-70 C), and has acceptable thermal conductivity (84

W/mK). The coefficients of thermal expansion for YAG and Ag are 7.5×10^{-6} and 18×10^{-6} , respectively, so a temperature change of -100 C (for engineering margin) will create a shear of about 1×10^{-3} .¹ The silver will contract at low temperature more than the YAG, and assuming the best case scenario in which the contraction occurs relative to the center of the 22-mm-long YAG slab, then at the end of the slab the shear would be about 10 μm . In the worst case, the shear would be 20 μm .

With a thermal conductivity six times higher than that of YAG, the thickness of the indium did not have to be held to a minimum. Small sheets of 200 μm thickness were available from the detector lab at Steward Observatory. The actual thickness of the indium layer will be less than this in operation because of the compression used to establish and maintain wetting between the YAG and indium surfaces. After disassembly the 'rut' created by the YAG slab is clearly evident, leading us to estimate that the actual indium thickness is about 150 μm . With this thickness, the indium only has to accommodate a shear of about 4-8 degrees between best and worst cases, which it can easily do.

To assure good wetting and continuous overall contact between the surfaces and the indium, the silver contact assembly must be held against the YAG slab with a moderate amount of pressure. Too much pressure would induce stress birefringence in the YAG, so the minimum amount required to establish wetting and maintain contact was desired. To determine this amount of pressure, we devised an experiment to observe wetting of indium through the spoiling of total internal reflection. The experimental setup is seen in Figure 8.5. A right-angle prism is placed with its hypotenuse down on a thin strip of indium, similar in size, shape and thickness to the strip to be used in the laser. Initially, the indium does not make good contact with the glass, so a bright uniform source can be viewed through TIR from the large flat surface

¹The coefficient of thermal expansion for most materials is not very constant, so the differential expansion between the materials changes as the temperature changes. These are therefore rough calculations at best. Any pretense at accuracy by carrying more than one significant digit would serve only to beguile the reader.

Material	Conductivity ($\text{W m}^{-1}\text{K}^{-1}$)	Expansion ($\times 10^{-6}/\text{C}$)
C (Diamond)	2500	0.8
Silver	429	18
Copper	401	17
Gold	317	14
Antimony	243	9
Aluminum	237	24
Tungsten	174	4.5
Iridium	147	6
Molybdenum	138	5
Brass	110	19
Chromium	94	6
Nickel	91	-
Indium	84	25
Sapphire	46	-
Titanium	22	8.5
StainlessSteel	15	17.3
YAG	14	7.5

TABLE 8.1. Cooling Assembly Materials. Values of thermal conductivity are from [44] and [53] while values of thermal expansion are from [109].

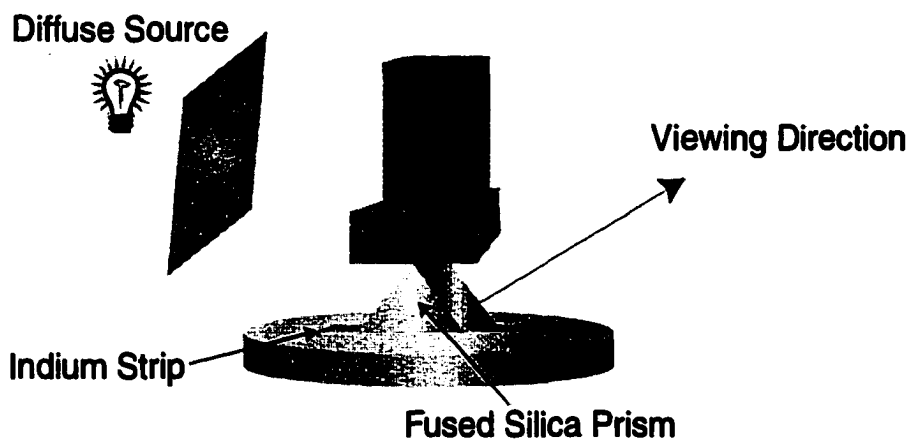


FIGURE 8.5. Experimental setup for measuring contact pressure required for good thermal contact between YAG slab and indium strip. Because a right angle prism of YAG was not available, we made the assumption that the fused silica and YAG were similar regarding the cohesion of indium.



FIGURE 8.6. Image of indium strip contacting the back of the prism and spoiling the total internal reflection. The reflection is the image of the black anodized surface of the structure placed atop the prism for weight.

of the prism hypotenuse. The top ridge of the prism is then weighted (using a fulcrum system with measured weights) until the image of the light source is compromised. This occurs when good contact of the indium with the glass surface allows the coupling of the light waves into the highly-absorbing indium sheet. The amount of force exerted on the prism ridge divided by the contact area between the prism and the indium indicates the minimum pressure required to achieve good contact. Once this contact is achieved, the pressure can be reduced somewhat because of the adhesion of the indium and the silica. We assume that because of the repetitive stresses induced by thermal cycling, this contact will have to be repeatedly established, and so a system maintaining a constant pressure at the minimum contacting pressure is needed.

Weights were placed atop the center of the beam so that the magnitude of the force applied to the ridge of the right angle prism was half the gravitational force of each weight. Previous experiments had shown that if the indium is pre-flattened it will adhere across its surface at lower pressures. After application of a weight, we

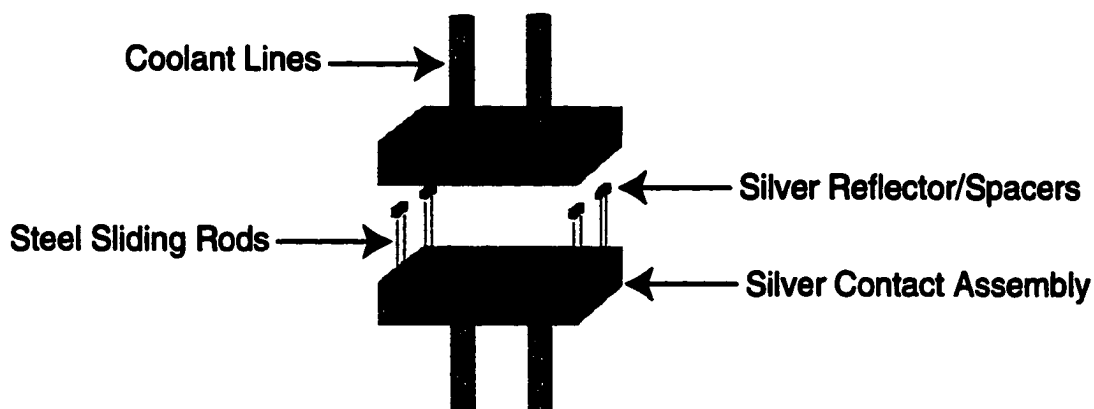


FIGURE 8.7. Exploded diagram of silver contact assembly. The steel rods are mounted into the bottom silver contact, and silver reflector/spacers are slid over these. Finally, the top silver piece slides down on top of the exposed ends of the steel rods. The Nd:YAG slab runs the length of the assembly, loosely held in place between the silver reflector/spacer pieces.

waited for at least two hours for the indium to flow. We obtained good contact across the 1.5×10 mm strip of foil when a total weight of 0.77 kg (including the beam) was applied to the prism, resulting in a required contacting pressure of about 50 g/mm^2 . The weights were applied in approximately 900 g increments², resulting in a ± 450 g margin of error ($\pm 30 \text{ g/mm}^2$).

The weights were then incrementally removed from the bar, waiting several hours after each to observe any release of the indium-silica bond. The bond maintained good contact with no pressure other than the negligible weight of the small fused silica prism, indicating that wetting (adhesion) was in effect. The resulting spoiling of TIR by the small indium strip can be seen in Figure 8.6. In this particular example, the indium strip can be seen better against a dark background, where the indium strip transmits through as a silvery-grey color. Prior to enough pressure being applied, there was no image of the indium strip beneath the prism.

To achieve an even, constant, known pressure of the silver contact assemblies

²The weights were magnetic bases with non-standard weight. Each was weighed independently and used in various combinations to obtain a rough estimate of the required force.

against the YAG slab through the indium, a system was devised in which the YAG was compressed between the silver contact assemblies sliding on eight small steel rods as shown in Figure 8.7. The rods were placed into holes drilled into the bottom silver contact assembly. Each pair of rods in each corner of the assembly also fixed a small silver spacer/reflector in place. This reflector was required to shield each end of the Nd:YAG slab from the pump diodes to prevent a buildup of heat where only one surface of the slab contacts the silver heat sink. These spacer/reflector blocks also served to hold the slab in rough alignment during final assembly and prevent it from sliding off of the small indium strips. After placing these reflectors over the steel alignment rods and placing the Nd:YAG slab in the assembly between the indium strips, the top silver contact assembly was mounted on the steel alignment rods. This made for an assembly that could hold the laser slab in place, but allow for a variable force to compress the indium strips and bond the slab to the silver contact assemblies.

Thin fiberglass insulation blanketed each silver contact assembly, insulating them from a pair of thick, rigid G-10 panels which maintained the whole system in compression with steel spring compression washers as shown in Figure 8.8. The bottom section was fastened to the bottom of the plexiglass box by compression against a very thin stainless steel tube surrounding the lower coolant lines. The thermal conductivity of stainless steel is rather low, and the thin-walled tubing provides rigidity with very little conducting area.

8.2.4 SiO₂ Waveguide Layer

One final layer is required to make the system operate effectively. Direct contact of the indium to the YAG surface would spoil the total internal reflection (TIR) which the slab relies upon for lossless ducting of the laser energy. To maintain TIR, the YAG must be coated with a thin dielectric insulating layer. The layer must have a fairly low refractive index to maintain TIR, and must be thick enough to prevent coupling

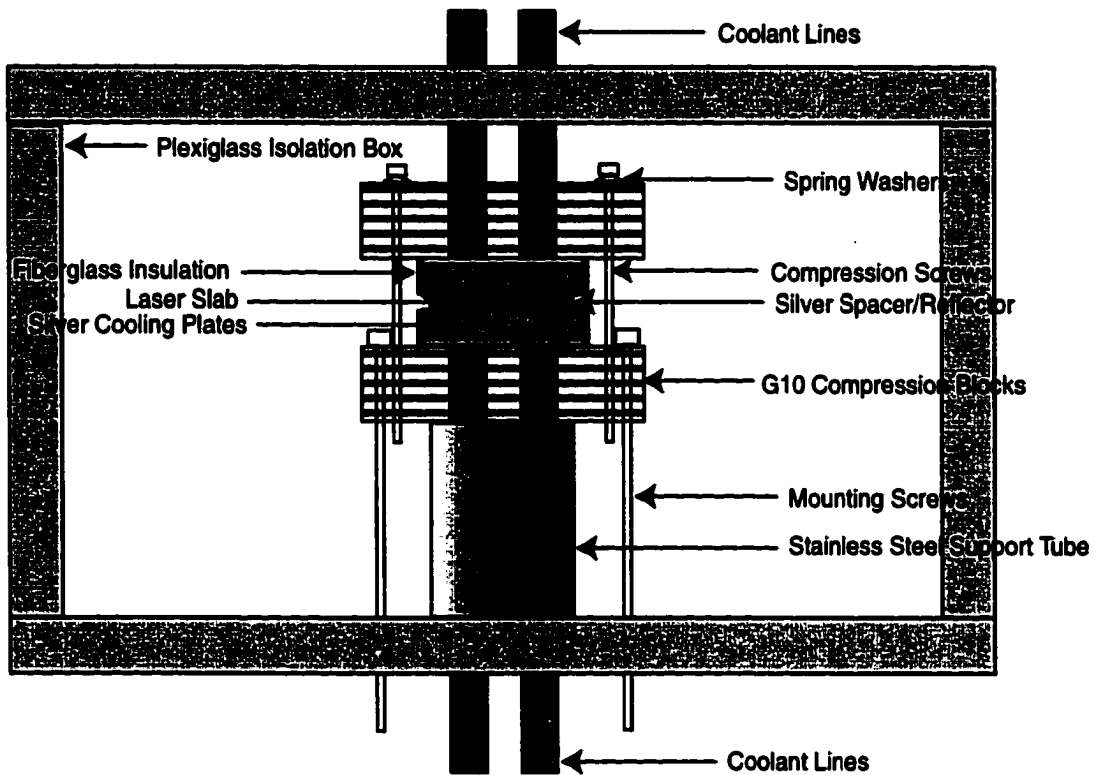


FIGURE 8.8. Side view of the compression assembly inside the plexiglass isolation box. The Nd:YAG slab is held in the center of the assembly by compression applied by the spring washers. The optical fibers from the pump diodes illuminate the two exposed sides of the Nd:YAG slab, reflecting the high-angle light back toward the slab with the polished silver contacts. Not shown are a high-reflector end mirror mounted inside the box just to the left of the slab and a hole with a fused silica Brewster window to allow the beam to exit losslessly in the right side of the box. The laser cavity is then completed with an external warm flat output coupler.

of electromagnetic energy through the layer, but thin enough to facilitate efficient thermal coupling to the indium. As seen in Figure 8.2 the rays of the propagating wave through the slab strike the surfaces of the slab at an angle of 57.58 degrees. The TIR angle in going from a medium with refractive index n_1 to a medium with index n_2 is

$$\theta_T = \sin^{-1} \left(\frac{n_2}{n_1} \right). \quad (8.1)$$

In the case of YAG ($n_{YAG} = 1.82$) in air, the TIR angle is 33.33 degrees, so the slab is well within the TIR condition. By using the incidence angle as the TIR angle and inverting eqn 8.1, we find that the highest refractive index for n_2 for which TIR will still be satisfied is $n_2 = 1.536$. Therefore, any dielectric material with a refractive index lower than this value can be contacted to the YAG slab without spoiling the TIR operation of the slab surfaces. Fused silica (SiO_2) is such a material. With a refractive index of 1.46, it is well below the critical index. Furthermore, it is a very hard material which will resist scratching as it slides over the indium and silver surfaces, and can easily be deposited on most smooth surfaces. Finally, the coatings are usually very robust once applied[93].

A 2 μm layer of SiO_2 was sputtered onto both TIR surfaces of the Nd:YAG slab by Dr. J. H. Ruffner at Sandia National Laboratories. The coated YAG slabs were inspected under a microscope before and after several thermal cycles in the compression assembly. After thermal cycling, some small scratches appeared in the top of the coating running in the longitudinal direction of the Nd:YAG slab, and small sections of the coating had flaked away at the edges of the TIR surface. Since SiO_2 is significantly harder than either indium or silver, we concluded that some of the coating that had flaked away had been dragged across the surface of the slab through repeated thermal cycling, causing the longitudinal scratches in the surface. So if we could eliminate the flaking, we could probably eliminate the scratching.

These initial thermal cycling tests were not performed in nitrogen purged atmosphere, allowing water vapor to condense on the coated Nd:YAG slab. Dr. Ruffner suggested that water vapor could seep under the coating at the edge interface and destroy the integrity of the SiO₂-YAG bond, resulting in flaking near the edges. We performed the thermal cycling tests on a second slab in a nitrogen atmosphere, resulting in almost no flaking or scratching of the coating.

8.3 Testing and Results

8.3.1 Cooling and Nd:YAG Transmission Tests

The laser assembly was housed in a plexiglass box which allowed monitoring of the laser and cooling systems while maintaining thermal and atmospheric isolation. Dry nitrogen was leaked into the box to keep water vapor from entering and condensing on the cooled YAG faces. This pathfinder design was useful in testing some of the thermal and mechanical designs. A damaged Nd:YAG slab³ was used in this setup to assure that the system worked properly.

The cooling system was tested with no power to the laser pump diodes. In this test, the thermal cooler bath attained a low temperature of -49 C and the minimum temperature at the laser slab was -31 C. Dry nitrogen gas was leaked into the housing at a rate of 3 l/min, and effectively kept out all condensation for a period of several hours. A Mach-Zehnder interferometer operating at 633 nm continuously monitored the slab during cooldown and laser operation. With no power to the pump diodes, at a temperature of -31 C, there were 4 horizontal fringes of tilt where the interferometer was otherwise nulled. This indicated a slight degree to which the two Brewster windows were not parallel.

³Damage to the slab had been incurred over many months of testing, cleaning and design. The most obvious damage was chipping of the sharp, brittle corners of the Brewster surfaces, obscuring almost a third of the total surface of the surface. This was also the slab that incurred the bulk of the damage to the SiO₂ coatings. In spite of this damage, the slab was still capable of lasing, as we will describe later.

Absorption of the pump laser diodes was tested at the nominal laser operating temperature to verify good absorption. One set of fiber-coupled pump diodes was assembled on one side of the slab, while on the other side a large-area power meter measured the transmitted light. With 60 W input into the laser slab, 8.0 W registered initially on the power meter dropping to 7.2 W as the slab temperature rose from -31 C to -22 C. The number of tilt fringes on the interferometer increased to 6 horizontal fringes. At this point, the cooling bath temperature setting was set at -50 C, and the temperature began to drop. After 1 hour, the temperature at the laser slab was -27 C, and transmission had continued to drop to a stable 4.7 W, indicating a probable change to the pump diode lasing power and wavelength due to the poor control exercised by the diode laser cooling unit. The maximum absorption of diode power was observed when the diode cooling water was stable at 33 C.

With both sets of fiber-coupled pump diodes illuminating the sides of the laser slab at 60 W each, the interferometer indicated negative cylindrical lensing of focal length -0.4 m was induced in the slab.

8.3.2 Lasing Tests

A lasing cavity was set up around the slab with a 20 cm HR mirror 1 cm from the end of the slab inside the cold enclosure and a flat R=92% output coupler outside the enclosure a distance of 10 cm from the slab. The high curvature of the HR mirror was required to mitigate the negative thermal lens established in the laser slab. In this configuration CW lasing of 8.6 W was obtained with the laser slab at low temperature.

A fraction of the lasing power was directed into the entrance slit of a monochromator, and the spectrum was detected at the exit slit using a large-area Ge detector. The monochromator was scanned over a range from 1060 nm to 1065 nm. The temperature of the bath was then raised slightly (about 2.5 C) and another scan taken. Over a 2 1/2 hour period, the laser operated continuously at high power (6.0 W or

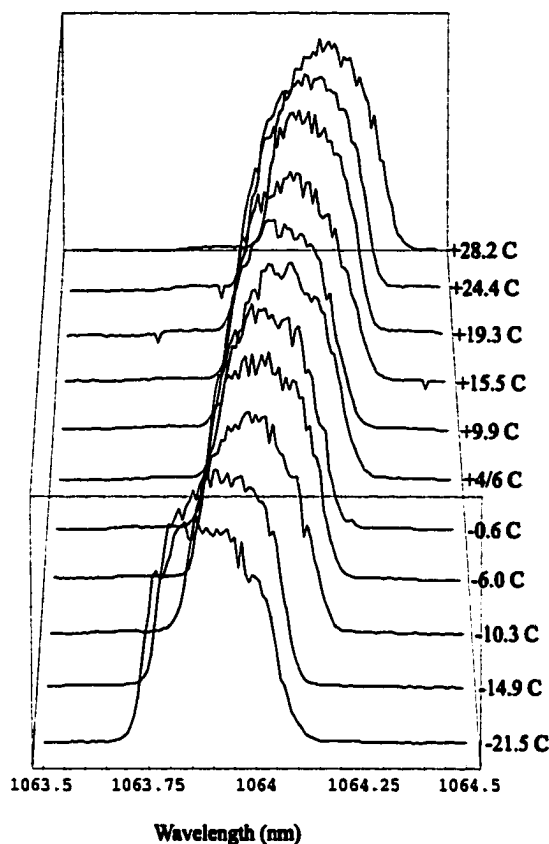


FIGURE 8.9. Lasing output of the cooled Nd:YAG laser as a function of temperature going from -21.5 C at the front to +28.2 C at the rear.

greater) and spectral scans were taken at 29 temperature points. Several of these scans spanning the temperature range from low temperature to high are shown in Figure 8.9. A distinct, linear shift of wavelength is observed.

The laser power as a function of temperature is shown in Figure 8.10. Except for the region between -20 and -10 C where the data were anomalously low, there appears to be a trend to higher power at lower operating temperatures where we wish to operate.

All of these data were taken with the prototype laser, using the damaged laser slab. With such success, we decided to begin operation of the improved version of the laser with a pristine slab. The new laser and housing units were assembled, and

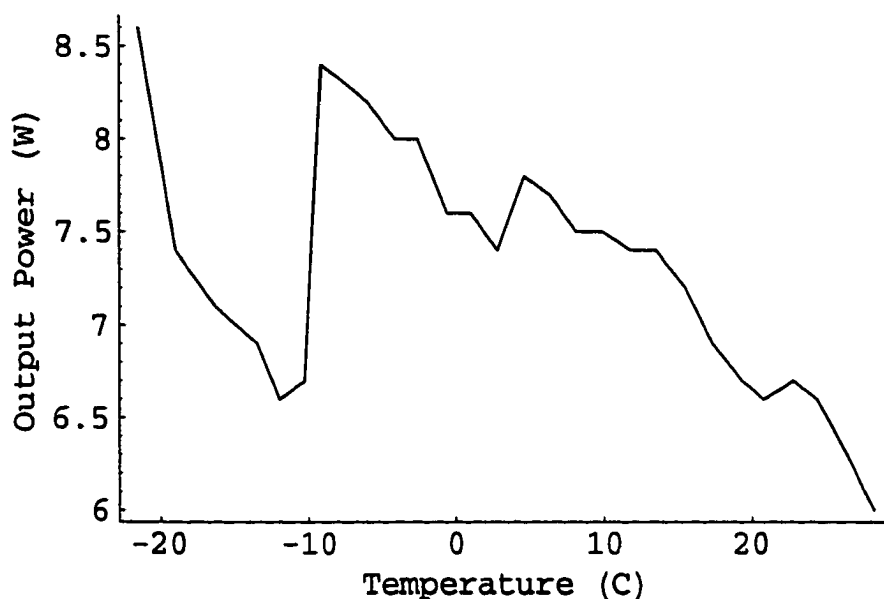


FIGURE 8.10. Output power of the laser as a function of slab temperature.

initial interferometry on the new slab was very promising. It appeared that with full diode power into the slab, a slight bit ($1/2 \lambda$) of spherical lensing and a bit more (4λ) of cylindrical lensing was induced in the slab. We had the laser power up to 4.5 W in this arrangement, but a catastrophic failure of the pump diodes put an end to testing and development.

8.4 Analysis and Conclusions

The power levels attained by the prototype laser design and the clear change of spectrum with operating temperature were very encouraging results for the development of a potential pump laser for a Raman guide star laser based on Raman shifting in CaWO_4 . This laser demonstrated that the engineering problems associated with developing a high power Nd:YAG pump laser which could be shifted to a wavelength for more efficient Raman shifting could be overcome with our design.

Analysis of the spectral data reveals a definite shift similar to that published by Kaminskii [49] as shown in Figure 8.11. To generate this figure, the output of each

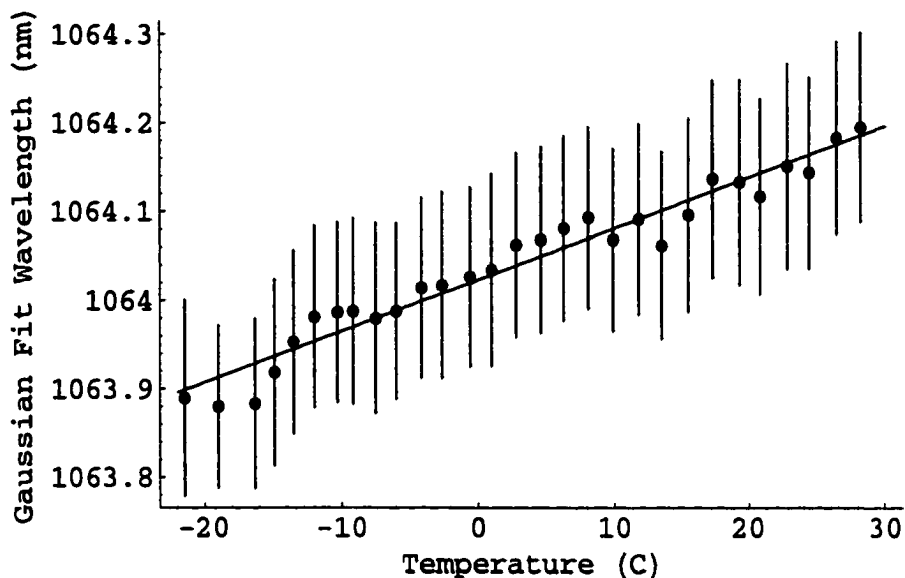


FIGURE 8.11. Peak wavelengths of best fits of data to Gaussian curves as a function of wavelength. The error bars are the width of the Gaussian curve that best fits the spectral curve.

of the 29 spectra were fit using a least-squares fit to a uniform Gaussian curve. The center of each fit function was plotted against the temperature for that spectrum and a linear least-squares fit was applied to generate the slope curve. Based on this analysis, the tuning function for Nd:YAG operating at high power is

$$\lambda_{Nd:YAG}(T) = 1064.02\text{nm} + T5.78 \times 10^{-3}\text{nm/C}. \quad (8.2)$$

Using this trend, we can predict that the operating temperature at which the CaWO_4 shifted wavelength of Nd:YAG is exact for frequency-doubling to the center of the sodium D_2 line is -53 C. Unfortunately we did not have sufficient cooling power to extend the experiment to this temperature. Nevertheless, we demonstrated the operation of the system at high power over more than half of the thermal range required with no indication of degraded performance at the lower temperatures.

There was some concern initially that spectral narrowing of the Nd^{3+} absorption lines would limit the ability of the laser crystal to absorb the pump light resulting

in a power loss at low temperature. This was not observed at the levels at which we were operating our laser; in fact, the highest output power was observed at the lowest operating temperature.

While the results of this experiment have been encouraging for the success of this guide star laser concept, there is much still to be done. Mode-locking of the thermally shifted Nd:YAG laser must be demonstrated, and the power and pulse length as a function of temperature must be measured to understand the thermal effects on the temporal dynamics of the laser system. These temporal characteristics are essential to knowing the future directions in which to move for efficiently generating bright sodium guide stars. Efficient, high-power Raman amplification at 1178 nm has still not been demonstrated. Raman photon-conversion efficiencies exceeding 90% have been demonstrated at low power, but there is no evidence that these efficiencies can hold at multi-Watt levels. Better gain and loss characteristics of the CaWO_4 crystals must be obtained to determine the optimum output coupling for complete Raman conversion. Finally, efficient high-power frequency doubling of the output must be demonstrated. Once all of these individual elements have been demonstrated, they must all be made to work together in order to realize a high-power Raman guide-star laser. Though these tasks are not considered trivial, this work has demonstrated the solution to the greatest technological impediment to the development of this Raman guide star system.

Chapter 9

COLOR CENTER LASER

The very strict tuning requirements of the guide star laser make wide-band tunable lasers a very attractive option; this is the primary reason that almost all guide star lasers in use around the world are tunable dye lasers. However, the difficulties of dealing with a liquid dye, the inefficiency of the cascaded pump/laser system, and the power limitations of dye lasers make solid-state options preferable. What is needed is a material with the ease of use of a semiconductor pumped solid state system, and the tunability of a suspended dye. Color center materials fulfill these requirements, and thus may hold promise for development of a guide star laser.

9.1 Color Centers

Most alkali-halide salts form single crystals of cubic structure. Because of this, they exhibit no natural birefringence and have good crystal-field qualities for hosting lasing ions. They can be made with good optical quality and are typically colorless across a very wide band ranging from the ultraviolet to the mid-infrared. They have relatively high negative thermal dispersion values ($\frac{dn}{dT}$) which tend to balance their relatively high positive coefficient of thermal expansion. Consequently, they are optically insensitive to thermo-optical effects which otherwise result in self-focusing in other laser host materials.

On the other hand, most alkali-halides are quite soft, having Knoop hardnesses a factor of 10-200 times lower than common laser crystals such as sapphire and YAG. Most of them are very hygroscopic, requiring a protective coating for normal operation in air. Most alkali-halides fracture easily, whether from mechanical or thermal shock. Their thermal conductivities are better than glasses, though most are lower than

YAG.

The best of these materials, LiF, is low enough in water solubility for normal use as a laser material, and its thermal conductivity exceeds that of YAG. Like the other alkali-halide salts, LiF is a soft, brittle material prone to thermal and mechanical shock, so care must be taken in using it as a high-power laser material.

The alkali-halide salts will form anionic vacancies within the crystal lattice when irradiated with all types of ionizing radiation (high energy electrons, neutrons, gamma rays, X rays, and hard UV) and also under calcination in alkali-metal vapors. In LiF the vacancy of fluorine atoms serves as a relatively positively charged site which collects free electrons in the material. Electrons localized at such sites tend to behave as if they were bound in a hydrogenic atom. These absorption bands are analogous to the $1s \rightarrow 2p$ transitions in the hydrogen atom, although they have cross-sections that exceed those of optically-active electrons in ions by orders of magnitude. These absorption bands are generally situated in the visible portion of the spectrum, imparting a color to the normally transparent crystal known as an 'F center' (from the German word for color, *Farbe*).

The F center of interest to us is the F_2 center, which forms when two adjacent fluorine atoms are displaced, as in Figure 9.1. Several different types of F_2 centers are possible: F_2^+ when only one electron collects at this site, leaving a net positive charge; F_2 when two electrons collect, leaving the site neutral; and F_2^- when three electrons collect at the site, resulting in a net negative charge. The latter of these is the one of interest to us, because it has a wide absorption band peaking at 960 nm, and a broad luminescence band peaking at 1130 nm[9].

Basiev *et al.* have extensively developed the F_2^- color center laser in LiF for applications in the near infrared requiring high power and tunability. Peak powers of 10^9 Watts with output energy of 100 J over 100 nsec have been obtained in the lasing range of 1.12-1.16 μm [9]. Though the repetition rate for this laser was not reported, the peak power greatly exceeds that required for doubling and projection

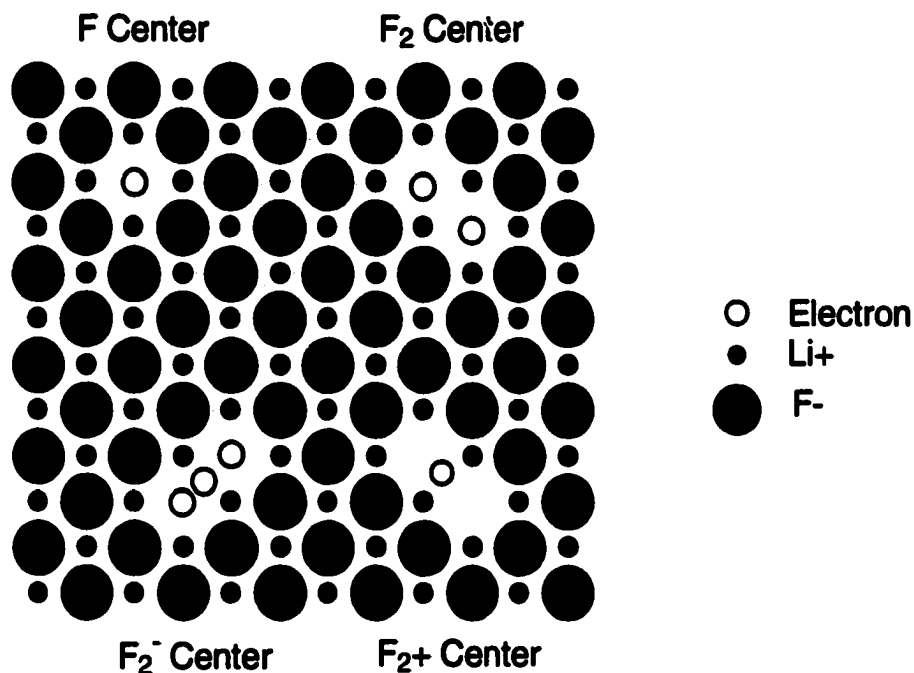


FIGURE 9.1. Sketch of different types of F₂ color centers.

to the mesosphere. Furthermore, the 100 nsec lasing lifetime exceeds the Q-switching lifetime of Nd:YAG by an order of magnitude. In other experiments, they have obtained CW lasing at the wavelengths of interest, but not at the powers that would be required for doubling and laser guide star production.

The electronic transition structure of a typical color center is shown in Figure 9.2. Following the description of Basiev and Mirov [9], absorption occurs in a color center by excitation of an electron at the bottom of the 1s state to an allowed location on the 2p band. Rapid phonon relaxation occurs from this point to the lowest energy point on the 2p band, within 0.1-1.0 ps. At room temperature, the lifetime of the electron in this state has been reported at 104 nsec, when it relaxes through photon emission to the 1s state. Momentum conservation and the offset minima of the bands prevents the electron from making the transition directly to the bottom of the 1s band. Instead, it must decay to an excited level in the 1s band, and decay through

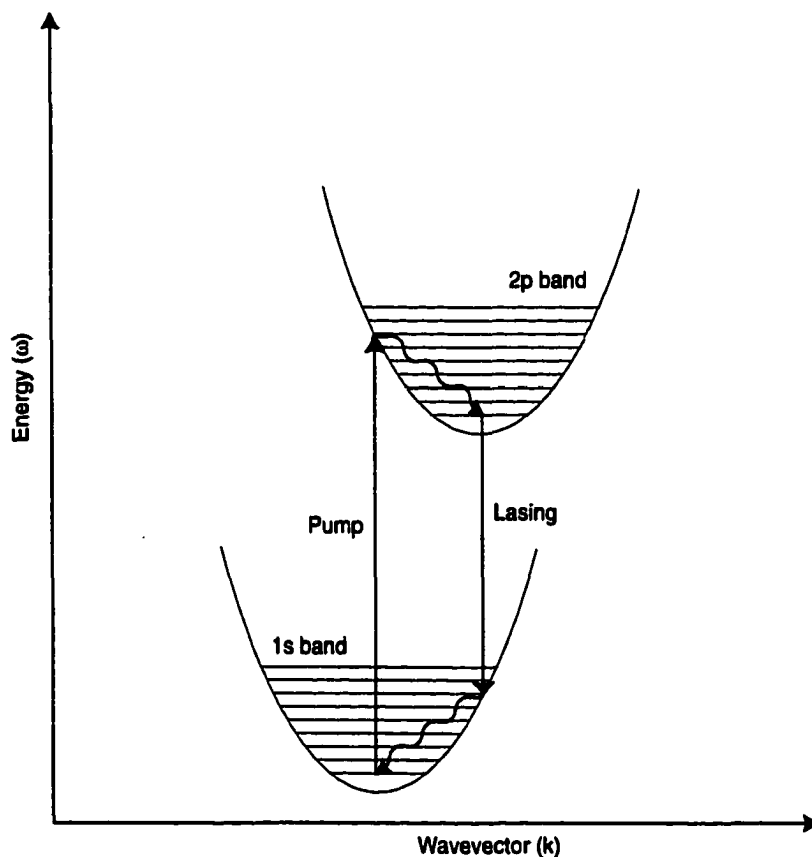


FIGURE 9.2. Diagram of lasing action in color center materials.

further phonon-assisted transitions to the band minimum.

This electronic structure, especially the decay to an excited level of the 1s state makes this a 4-level laser, which drastically reduces the lasing threshold for the material. Even though there are broad luminescence bands for the material, each of the F_2^- color centers is broadened in substantially the same way. Thus, the laser is homogeneously broadened, which ultimately allows almost all of the luminescence to be concentrated into a single narrow line.

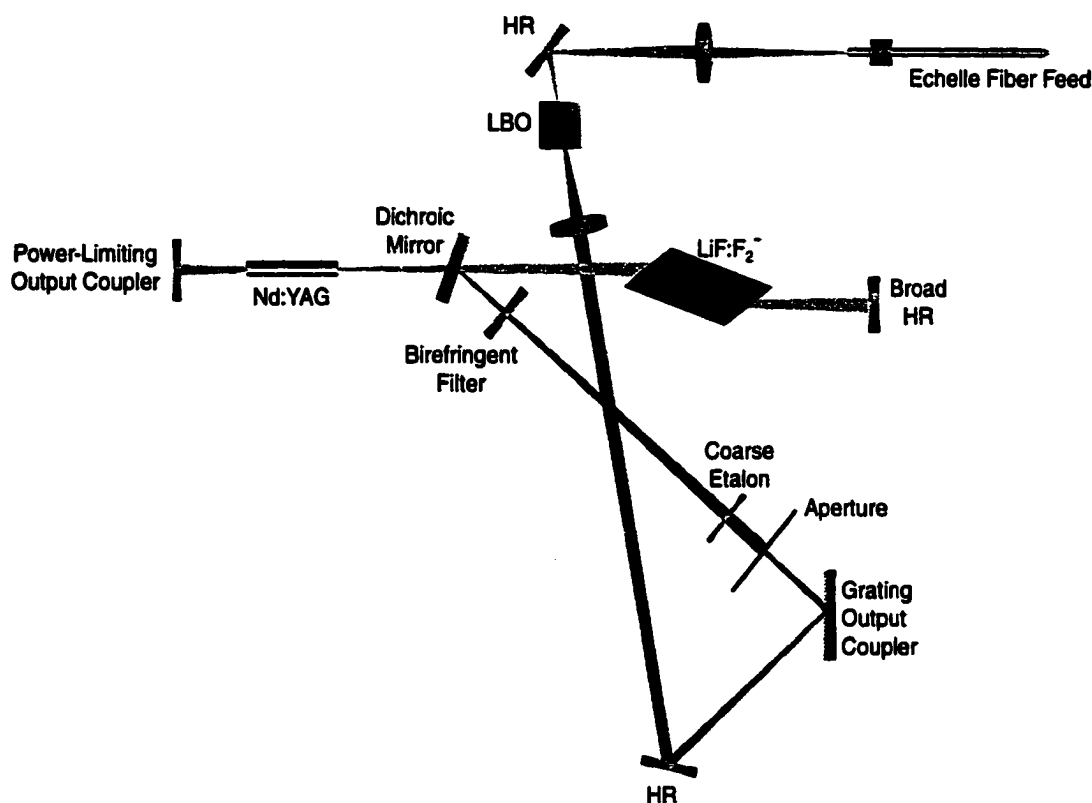


FIGURE 9.3. Diagram of the tunable color center laser. The green beam represents the fundamental wavelength of the Nd:YAG pump laser, while the blue beam represents the 1178 nm lasing of the color center laser. In the portion of the cavity with the color center crystal the two beams are overlapping, represented by a blend of the colors.

9.2 Color Center Laser Development

We obtained a crystal of $\text{LiF} : \text{F}_2^-$ color center material from T. T. Basiev through Lite Cycles, Inc. The material is a reddish brown, opaque (in the visible), glassy material with a physical path length of 88 mm. The faces were cut so that with the laser input at Brewster's angle the beam in the crystal will propagate along the long axis of the parallelogram.

We assembled the overlapping cavity laser shown in Figure 9.3. The color center crystal was placed between a pair of copper cooling plates which are cooled with

flowing water. The Nd:YAG pump laser was a Xenon flash-lamp pumped system generating up to 35 J/pulse at 10 Hz. An R=70% output coupler was placed at the far end of the Nd:YAG laser to limit the power buildup in the cavity and ensure that the color center crystal was not damaged. A flat dielectric mirror was placed between the Nd:YAG rod and the color center crystal. This mirror has high transmission at the 1064 nm YAG wavelength, and is a high reflector at 1178 nm. The dichroic flat was turned until maximum transmission was attained at 1064 nm, maximizing the pumping of the color center material. The output coupler for the color center laser was a blazed infrared grating, operating in the Littrow configuration. The grating is turned to tune the color center laser, and the zero-order reflection from the grating is taken as the output beam. The output was directed to a doubling assembly consisting of an $f=150$ mm lens and a crystal of LBO. The doubled output was then focussed onto an optical fiber feeding a high-resolution echelle spectrograph for monitoring the output wavelength and bandwidth.

Using only the grating for tuning, the total lasing bandwidth observed on the spectrograph was approximately 200 GHz. To narrow the linewidth and direct the energy to the sodium line, we inserted a single thick (fine-adjustment) birefringent filter from the dye laser. For fine tuning, a 25 mm thick etalon was introduced into the cavity as well.

The lasing spectral output is observed in Figure 9.4. This image shows the tuned output of the color center laser as the spot on the right, simultaneously compared with the Doppler-broadened spectrum of the output of the D_2 line of a low-pressure sodium lamp on the left. The lasing spectrum is approximately tuned to resonance, and narrowed to match the line width.

The onset of lasing for this tuned configuration occurred when the Nd:YAG laser was pulsed with 30 J from the flash lamp. At this level, with the color center laser cavity tuned to center the output spectrum at 1178 nm, the average power from the color center laser at 10 Hz was 30 mW (average pulse energy of 3 mJ). Power increased

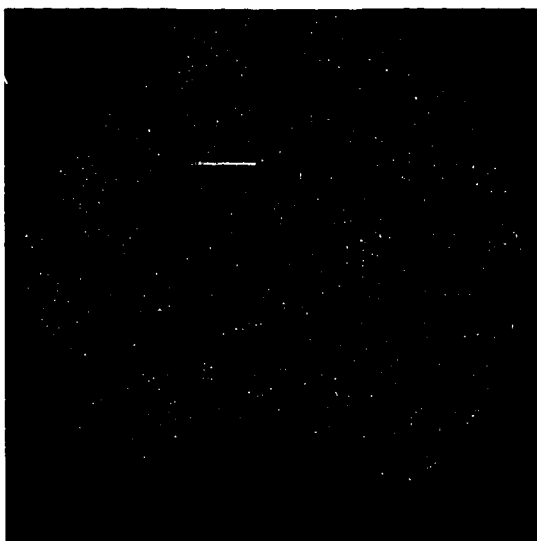


FIGURE 9.4. The spectrum of the tuned and frequency-doubled color center laser output (spot on right) compared with the output of the D₂ line of a low pressure sodium lamp (line on left). The lasing output is slightly narrower than the 3 GHz broadened spectrum of the sodium line.

slightly to 35 mW by pumping the Nd:YAG laser with 32 J/pulse, but subsequently decreased and leveled off at 32 mW with up to 35 J/pulse.

9.2.1 Thermal Defocus Measurements

Among the most significant problems encountered in developing most solid-state lasers for continuous operation at high power are the deleterious thermal effects that arise from high heat generation rates and low thermal removal rates. The optical effects that are often induced are the onset of thermal lensing which affects the cavity configuration and lasing efficiency, and stress-induced birefringence. The obvious mechanical limitations of thermal stress (inducing crystal fracture) are not usually encountered until well after the optical effects are manifest.

The advantage of LiF as a lasing material is that the thermal lensing induced is extremely low. While the coefficient of thermal expansion in the material is moderately high ($\alpha_T = 3.2 \times 10^{-5}/\text{C}$), the refractive index of the material is very low

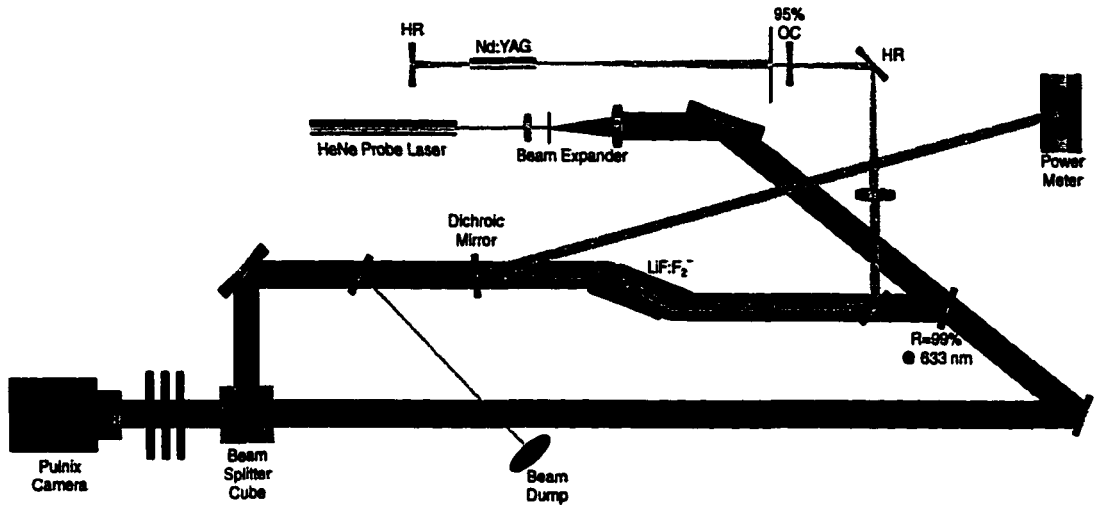


FIGURE 9.5. *In-situ* interferometry experiment in which the thermo-optic effects induced in the color center material can be measured and monitored simultaneously with pumping.

(1.38) minimizing the optical impact of thermal expansion. Balancing this is the negative change in refractive index with temperature, listed as $-1.2 \times 10^{-5}/\text{C}$. The total change in optical path length ΔOPL for a given length L of material over a temperature difference ΔT is given by

$$\Delta OPL = L(n - 1)\alpha_T\Delta T + \frac{dn}{dT}L\Delta T \quad (9.1)$$

which for our case is $\Delta OPL = 1.6 \times 10^{-7}\alpha_T\Delta T$, which is two orders of magnitude lower than most materials.

To verify the optical insensitivity of the color center laser to thermal effects, we set up the *in-situ* interferometry experiment shown in Figure 9.5, in which the optical path length of the material was monitored with a probe beam at 633 nm as the laser was pumped at 1064 nm. The interferometer design is a single-pass Mach-Zehnder interferometer at 633 nm. The absorption of the color center material at 633 nm requires that roughly 99% of the HeNe power be transmitted in the test arm, and 1% in the reference arm to optimize the fringe visibility. A dichroic mirror (actually, a Nd:YAG output coupler) is used to direct the majority of the pump beam

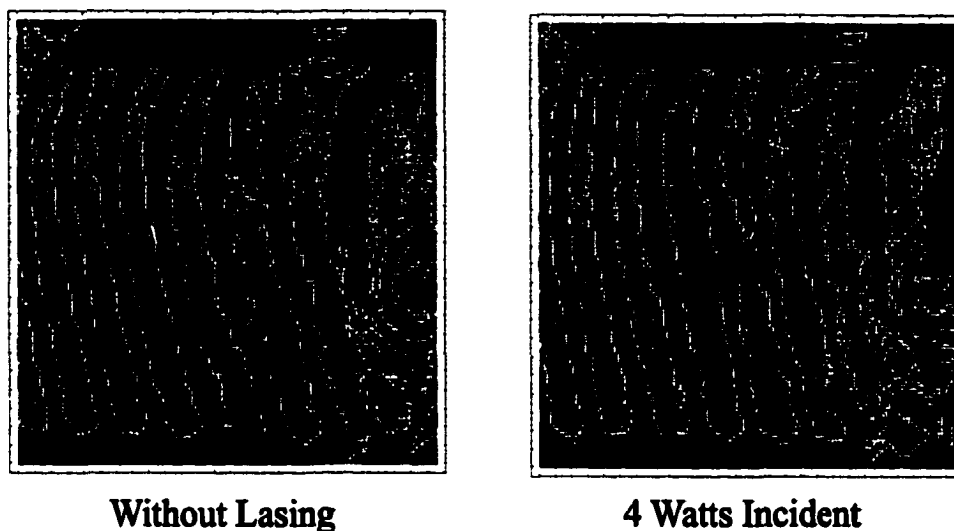


FIGURE 9.6. Interferogram of the $\text{LiF} : \text{F}_2^-$ color center crystal with no Nd:YAG laser pumping applied (left) and with 4 W incident (right). The pump was localized on the area outlined by the black circle. Note that there is a maximum shift of $\lambda/4$ where $\lambda = 633 \text{ nm}$. A shift to the right indicates less path length or negative lensing.

to the power meter for monitoring absorption. Another Nd:YAG laser high reflector is required beyond that to prevent any of the pump light from reaching the camera.

The results of the experiment are seen in Figure 9.6. Tilt fringes were introduced so that the amount and type of thermal lensing (positive or negative) could be measured more readily. The color center crystal was conductively cooled at the top and bottom by contact with water-cooled copper blocks. This cooling introduced a slight thermal gradient in the material resulting in the fringe-bending at the top and bottom of the image. The total length of the LiF crystal (along the lasing axis) is $L = 88 \text{ mm}$. The image on the left is the reference image of the color center crystal without any Nd:YAG pumping applied. On the right the effects of pumping continuously with 4 W of arc-lamp-pumped, Q-switched Nd:YAG at the site indicated by the dark circle are observed. The thermal effects in the crystal are barely noticeable, consisting of a shift of roughly one-half fringe to the right, in the direction of negative ΔOPL . The value of $\frac{dn}{dT}$ accounts for slightly more shift than the crystal expansion, at least at the probe

wavelength of 633 nm. Thermal modeling of the temperature differential of LiF from the center of the pump beam to the cooling block brackets the temperature difference between 40K and 60K, depending on the pump beam size. Assuming a temperature differential of 50K, a crystal length of 88 mm, and a fringe shift of $\lambda_{HeNe}/2$ gives an estimate of the thermo-optic coefficient of $7 \times 10^{-8} \text{K}^{-1}$, approximately a factor of two lower than and in the opposite direction from our estimate. The discrepancy is not unexpected, given the small calculated value and the precision to which the index dependence on temperature is known.

Despite pumping with up to 20 Watts of Q-switched Nd:YAG power, our various color center laser cavities never exceeded 100 mW. The absorption of the color center crystal at the Nd:YAG wavelengths was near optimal (70%), and lasing could be obtained at low threshold intensity. Measurements of the Nd:YAG pump beam reveal an intensity of approximately 1.2 MW/cm^2 , well below the optimum conversion intensity of 80 MW/cm^2 published in [9]. The color center cavity mode was considerably smaller than the pumped volume, resulting in further inefficiency. Finally, we suspect that the high gain of the material results in excessive loss through amplified spontaneous emission (ASE), and parasitic losses, though these were never verified.

9.3 Conclusions

Many of the properties of LiF : F_2^- material are desirable for development of a high power laser tunable to 1178 nm. We have demonstrated the potential of such a laser to be tuned and doubled to produce radiation of the right frequency. Finally, we have demonstrated that it is virtually immune to thermal focus, a highly desirable quality for scaling to high power. The material is capable of very high gain, and can be pumped with any of the high-power lasers employing the Nd^{3+} ion as the lasing ion. With its broad absorption peak at 960 nm, the material is ideally suited for high power CW diode pumping. The broad absorption band, and broad, homogeneously

broadened transition peaked near the double wavelength of 1178 nm make this laser ideal for a guide star application in many ways.

More research is needed to investigate the factors limiting power extraction. The lifetime of the lasing state must be considered more carefully, especially with respect to the potential for Q-switched and CW output. Explanation and mitigation of the poor power performance could ultimately yield a material with high gain and superior tunability for operation as a laser gain material, or as a laser amplifier in a master oscillator power amplifier (MOPA) laser.

Chapter 10

THE APATITE LASER

10.1 Introduction and Background

Several properties of solid-state lasers make them attractive for routine daily use at remote sites such as the locations of most research telescopes. Solid state lasers can be engineered to be very robust, requiring little maintenance and exceptional ruggedness. They can often be made quite compact, and have little sensitivity to orientation so that attaching them to the side of a moving telescope structure is not out of the question. It is often a matter of proper engineering to drive the output power capability of some solid-state lasers into the range of several Watts (at least). Finally, many solid-state lasers are characterized by a high wall-plug efficiency, minimizing the additional overhead of power and cooling that are occasionally at a premium at remote telescope locations.

Given these advantages, it is desirable to find a type of solid-state laser which can be scaled to 10-20 W of output power, and can be coaxed to operate directly at the 589 nm sodium D₂ peak. Unfortunately, there is a dearth of materials with potential lasing lines near this wavelength.

To overcome this deficiency, we consider the potential of solid-state lasers operating in the near infrared. If it were possible to develop a high-power laser at 1178.0 nm, then mature frequency doubling techniques could be employed to efficiently generate an output wavelength of 589.0 nm.

There are entire volumes devoted to the identification of potential lasing transitions of various ions in various materials, and lasers that have successfully been shown to operate at various wavelengths [110]. Yet, perusal of these tomes shows the clustering of lasers around particular wavelengths, leaving large gaps in the spectrum that

cannot be readily accessed with solid state laser materials, among them the spectral regions around 589 nm and 1178 nm.

There are reports in the literature of fluorescence peaks indicative of potential lasing action by the Mn^{5+} ion in apatite-type crystalline materials close to 1178 nm. Laser gain was observed in $\text{Mn}:\text{Sr}_5(\text{PO}_4)_3\text{Cl}$ and $\text{Mn}:\text{Ca}_2\text{PO}_4\text{Cl}$ [17], and actual lasing was demonstrated in $\text{Mn}:\text{SVAP}$ ($\text{Mn}:\text{Sr}_5(\text{VO}_4)_3\text{Cl}$) [66] and $\text{Mn}:\text{BOV}$ ($\text{Mn}:\text{Ba}_3(\text{VO}_4)_2$) [67]. Finally, tuning of the fluorescence band by changing the host material demonstrated a peak fluorescence at 1181 nm in $\text{Mn}:\text{BCAP}$ ($\text{Mn}:\text{Ba}_5(\text{PO}_4)_3\text{Cl}$) [76], very near the 1178 nm line required for frequency-doubling to 589 nm.

With all of these elements in place, we decided to pursue development of a $\text{Mn}:\text{BCAP}$ laser operating at 1178 nm. The initial concept called for development of a guide star laser in which many $\text{Mn}:\text{BCAP}$ lasers are pumped by inexpensive, efficient laser diodes operating in the near infrared. The outputs of these lasers are then combined to produce a bright beam at 1178 nm which would subsequently be doubled and directed into the sodium layer. Unfortunately, $\text{Mn}:\text{BCAP}$ is not readily available¹, so we contracted with a crystal grower² to develop the material, a process which was expected to take several months. In the interim we experimented with natural fluorapatite as a surrogate gain material until the $\text{Mn}:\text{BCAP}$ was ready. Unfortunately, the crystal grower was never able to seed the melt for Czochralski growth, and thus never produced good crystals of $\text{Mn}:\text{BCAP}$. As a result, the majority of this work was centered around the development of the surrogate fluorapatite material as a laser.

¹BCAP actually has been identified in natural form as *alforsite*[75], but it is extremely rare, coming only from the Big Creek mine in Fresno County, California, and the natural form only exists in fine-grained crystals approximately 0.02 mm in diameter.

²The contract was with Scientific Materials, Inc. in Bozeman, MT.

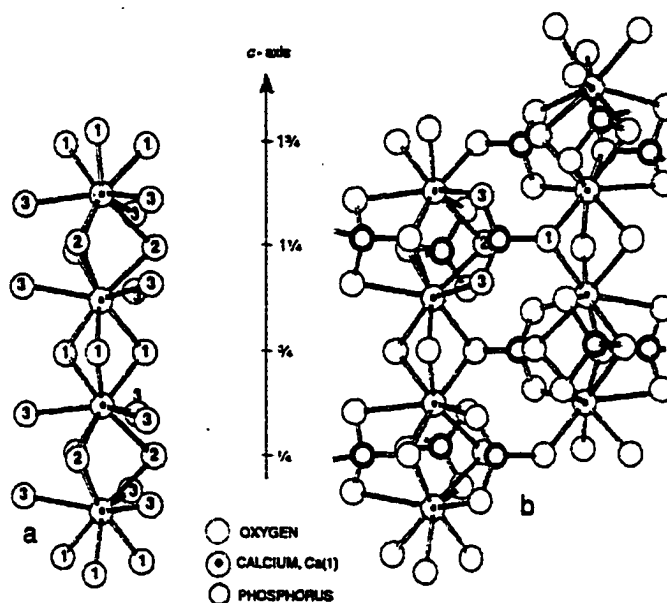


FIGURE 10.1. The molecular structure of fluorapatite after McConnell [64]. Columns of calcium atoms parallel to the optical axis are linked in place with oxygen atoms (a). These separate columns are then linked through phosphorous atoms which make up the PO_4 tetrahedra (b).

10.2 Apatite ($\text{Mn}:\text{Ca}_5(\text{PO}_4)_3\text{F}$)

Apatite is a common mineral of composition $\text{Ca}_5(\text{PO}_4)_3\text{X}$ in which the X element determines the type of apatite. The three common varieties of true apatite are fluorapatite ($\text{Ca}_5(\text{PO}_4)_3\text{F}$), chlorapatite ($\text{Ca}_5(\text{PO}_4)_3\text{Cl}$) and hydroxyapatite ($\text{Ca}_5(\text{PO}_4)_3\text{OH}$), the latter of which is the principal constituent of teeth and bones. The name apatite comes from the Greek *απαταω* (to deceive); the name was coined by A. G. Werner because of its tendency to look like other minerals depending on the composition and density of impurities [27].

The most common mineral form of apatite (and the natural form that we have dealt with) is fluorapatite, the atomic structure of which is seen in Figure 10.1. The basis of the structure is comprised of columns of calcium ions parallel to the optical axis of the crystal. These columns are held together by groups of three oxygen ions

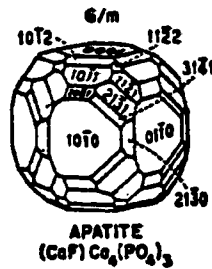


FIGURE 10.2. Facet planes of apatite after Wood[112].

above and below the calcium ions. In addition, each calcium ion is also bonded to three more oxygen ions, coplanar with the calcium ions and normal to the optical axis. These columns of ions are joined by the phosphorous ions which connect three oxygen atoms from one column, to one oxygen ion from the other column. This accounts for all of the phosphorous and oxygen ions. Between these oxygen ions linking the columns of calcium there are large spaces into which the fluorine ions fit. These fluorine ions are surrounded by triangles of the remaining calcium ions which fill out the complete structure of apatite. This structure gives rise to a plethora of crystal planes, as seen in Figure 10.2 taken from Wood [112].

The crystal has C_{6h} symmetry, and is thus uniaxial and slightly birefringent with an ordinary refractive index of 1.6325 [64] and an extraordinary refractive index of 1.635. It is a relatively soft material in comparison with most other gemstones, and is used to define the level 5 on the Mohs hardness scale, comparable to most glasses.

Apatite occurs naturally in many different colors and intensity of color. A very common form is a relatively transparent, blue material from Madagascar (called neon blue in the gem trade) and darker blue material from the Durango mine in Mexico and the Hugo mine of South Dakota. Coming directly from the ground, the apatite exhibits an opaque green color, and is turned blue by heating to temperatures of up to 600 C[47]. The blue color is believed to be the result of absorption by impurities of



FIGURE 10.3. Design of portable infrared spectrometer for observing IR apatite fluorescence.

Mn^{5+} , substituting for phosphorous in the PO_4^{-3} group [47][14][56]. In this site, the manganese ion takes on an unusual +5 charge state which leaves it with two optically active $3d$ electrons. These electrons are not shielded, as the optically active electrons in rare earth elements are, and so their energy levels are very sensitive to variations in the crystal field. Because the Mn^{5+} ion sits in a site that is tetrahedrally surrounded by O^{2-} ions, to first order the perturbations to the field will take on a tetrahedral or T_d symmetry. The lower-order symmetry of the external crystal field of the complete apatite structure will perturb this splitting, but these perturbations are expected to be minor, compared to the T_d group analysis.

Samples of blue apatite were obtained at the Tucson Gem and Mineral Show, and were carefully checked for absorption at red wavelengths, fluorescence yield in the infrared, and fluorescence spectral peaks near our desired wavelength. The latter was performed by observing the fluorescence on a portable IR spectrograph developed

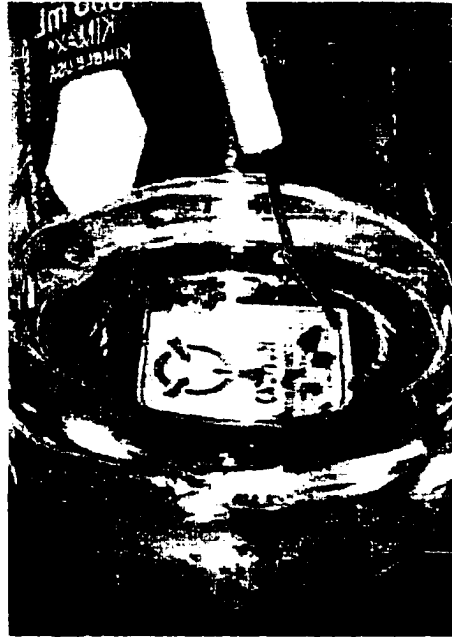


FIGURE 10.4. Rough apatite crystals in beaker of CS_2 .

for the purpose shown in Figure 10.3. The majority of stones purchased were rough stones, so it was not possible to judge their clarity or purity on the spot. In the laboratory, the stones were immersed in CS_2 which has an index of 1.633, and matched the index of the apatite material very well. Upon inspection in the index matching fluid, refraction effects at the surface boundaries disappeared, as seen in Figure 10.4, allowing us to choose the clearest and cleanest samples without the trouble of polishing each. The chosen samples were flattened and polished using a gem-cutter's wheel. A final hand polish of the best samples was performed by using successively finer grades of optical fiber polishing film, which resulted in smooth, clean surfaces on the crystals.

Once polished, the apatite crystals were examined under an Olympus polarizing microscope. Small lines that we believe are tiny fracture planes estimated to be 10-20 μm in length were observed throughout the crystal, as seen in Figure 10.5; similar small cracks were reported for natural apatite by Elliott [27]. For a crystal with



FIGURE 10.5. Microscopic fracture planes in two different crystals of blue apatite. The photo on the left is under direct illumination, and the fracture planes are normal to the line of sight. The photo on the right was taken under dark-field illumination, and is taken at an angle with respect to the fracture plane, showing the oval shape of the fractures.

surfaces polished normal to the plane of cracks, seen on the left in Figure 10.5, the cracks appear at angles of 120 degrees with respect to one another, as one might expect for a crystal with C_{6h} symmetry. When red laser light at 685 nm was directed through the crystal, a principal line of scattering was observed on the output side, aligned normal to the internal cracks. The amount of scattering was variable dependent upon the location of the beam in the crystal, and for the best locations (*i.e.* minimum total scatter) the total integrated scattering appeared to be less than 1%.

The crystal on the left in Figure 10.5 was the crystal on which most of the detailed experimentation was performed. A sample of this crystal was sent away for chemical analysis³ which placed the manganese density at 325 parts per million (ppm). From this we calculated a number density of 1.15×10^{19} atoms/cm³. The analysis also detected the elements B, Cr, Fe, Na and Sr, but did not quantify the amount of each of these.

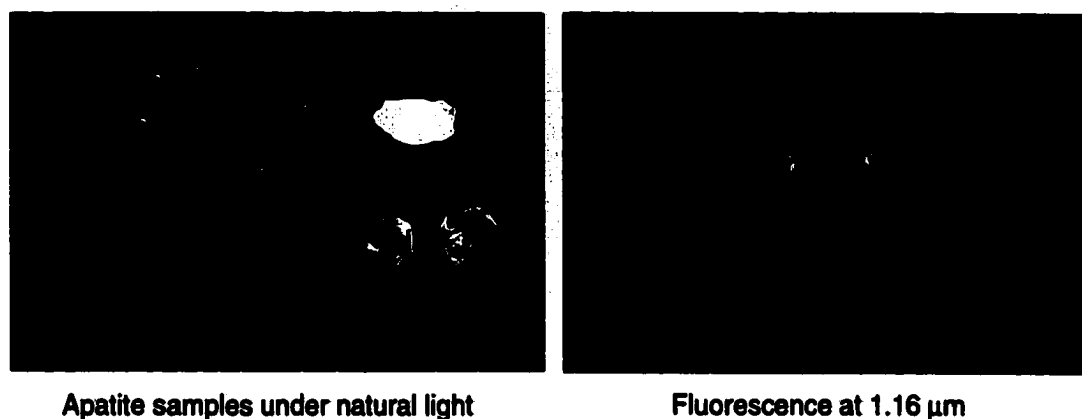


FIGURE 10.6. Observation of various samples of apatite in natural visible light (left) and in the near infrared(right). The infrared image was taken while illuminating the samples with bright red LEDs at 685 nm. All visible and pump light is eliminated from the image by using a polished silicon wafer as a long-pass filter.

10.3 Apatite Fluorescence

As shown in Figure 10.6, the fluorescence of natural apatite can easily be observed using an infrared imager (preferably enhanced to extend the wavelength sensitivity beyond the 1.1 μm silicon detection cutoff). We see that not all crystals purported to be apatite fluoresce well. Under intense illumination by a bank of bright red LEDs, the samples of neon-blue and royal-blue apatite crystals toward the front of the figure appear to glow intensely in the infrared, while other colors of apatite (even deep blue crystals) emit weakly or not at all. Some of the green apatite samples such as the elongated one in the center of Figure 10.6 appeared to be good fluorescent crystals, but had low red absorption, reducing their value as lasing crystals.

All spectral scans of apatite samples were taken with a CVI CM110 grating monochromator. The infrared scans were performed using a grating of 600 grooves/mm, blazed for 1200 nm. The monochromator uses replaceable slits of widths ranging from .125 mm to 2.4 mm. The light at the output slit of the detector was generally detected

³The analysis was an Inductively Coupled Plasma (ICP) analysis, performed by Desert Analytics, Inc. in Tucson.

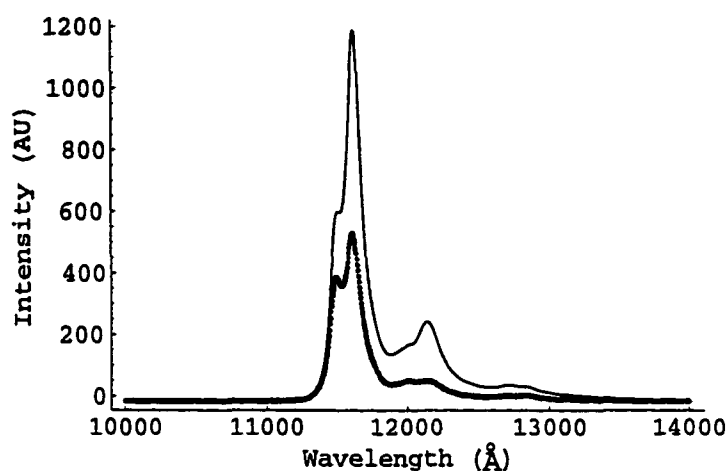


FIGURE 10.7. Fluorescence spectra for natural apatite for π (solid black line) and σ (blue dotted line) polarizations of the apatite crystal.

with a high-gain InGaAs detector (model g3476-05 from Hamamatsu). A low noise transimpedance amplifier circuit with a 200 M Ω feedback resistor was used to send the signal into a 10x operational amplifier for a total transimpedance gain of 2.0×10^9 V/A. The entire operational configuration was controlled with a Windows program written by the author to control the stepping of the monochromator and acquisition of data by the detector. The light source for transmission measurements was a single current-controlled tungsten-filament bulb situated in a thermally massive aluminum housing, typically operated at 7W. A diffuser was placed between the bulb and the sample to randomize the polarization of the source, and to provide spatial uniformity.

Previous studies of the absorption of fluorapatite indicated a strong absorption band from roughly 500-800 nm, which is largely responsible for the blue color of apatite [47]. We used a laser diode at 685 nm near the peak of the absorption band to stimulate fluorescence. The stimulating wavelength and visible background light were completely filtered out with a polished silicon wafer covering the input slit of the monochromator. A Glan-Thompson polarizing prism was placed between the fluorescing apatite stone and the entrance slit of the monochromator to discrimi-

nate between polarization states. The resulting fluorescence profiles are observed in Figure 10.7, and are seen to be significantly polarized. Because the grating efficiency differs for polarizations parallel and perpendicular to the slit, the relative ratios of the two curves are not mutually calibrated. However, the emission at 1161 nm appears to be most strongly polarized.

The emission spectrum exhibits peaks at 1151.4 nm, 1161.2 nm, 1199.8 nm, 1214.2 nm, 1270.6 nm and 1281.6 nm. The latter two are very weak, and are easily skewed by overlapping with stronger neighboring peaks. The location of the peaks between σ and π polarizations are consistent to within 1 nm. The ratios of relative intensities for both curves reveals the possibility that the two sets of peaks around 1210 nm and 1285 nm are Raman-shifted spectra of the principal peaks around 1155 nm. Were this the case, the set of curves around 1210 nm are Raman shifted by about 365 cm^{-1} , while the second set would be Raman shifted by 815 cm^{-1} from the primary lines. Analysis of the Raman-active modes of fluorapatite by Elliott [27] identifies a very strong Raman mode at 963 cm^{-1} , and medium activity at 429 cm^{-1} , 580 cm^{-1} , 591 cm^{-1} , and 1051 cm^{-1} . All other Raman-active modes are listed as weak or very weak. None of these lines are very close matches to our observed hypothetical Raman spectrum, leading us to believe that they are probably real transitions.

For a Mn^{5+} ion with a pair of d^2 electrons in a weak crystal field⁴, the 1D free ion term splits into 1E_g and $^1T_{2g}$ terms, while the 3F term splits into $^3A_{2g}$, $^3T_{1g}$ and $^3T_{2g}$ terms [104] [82]. At higher crystal field strength ($Dq/B > 2$), the $^3T_{2g}$ energy level crosses above the 1E_g metastable level, from which the fluorescence decays to the $^3A_{2g}$ ground state. The E irreducible representation is two dimensional, and thus is doubly degenerate, while the $^3A_{2g}$ ground state is one dimensional, but is a triplet state, and thus triply degenerate. This is fortunate because the higher degeneracy of the ground state reduces the pumping threshold of the material somewhat, partially

⁴Much of the detail of the derivation of the energy levels for a pair of $3d$ electrons in a crystal field is contained in Appendix A.

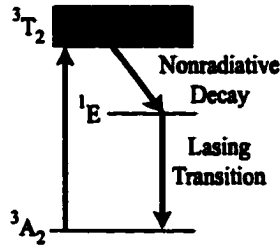


FIGURE 10.8. States of a 3-level atom, in which state 3A_2 is the ground state and state 1E is the metastable lasing state.

mitigating the difficulties of pumping a three-level laser material.

10.4 Lasing Efforts

10.4.1 Three Level Atom Model

Since the lasing transition of Mn^{5+} appears to be from the 1E_g excited state to the ${}^3A_{2g}$ ground state, we must model the laser as a three-level medium, in which (for simplicity) the ground state is labeled as $|0\rangle$, the pump state is $|1\rangle$, and the metastable lasing state is $|2\rangle$ (Figure 10.8). The differential equations governing the populations are given by:

$$\frac{d}{dt}n_0 = -W_{0\rightarrow 1}n_0 + \frac{n_2}{\tau_2} \quad (10.1)$$

$$\frac{d}{dt}n_1 = W_{0\rightarrow 1}n_0 - \frac{n_1}{\tau_1} \quad (10.2)$$

$$\frac{d}{dt}n_2 = \frac{n_1}{\tau_1} - \frac{n_2}{\tau_2} \quad (10.3)$$

in which n_i is the population density in level i , τ_i is the natural lifetime of state $|i\rangle$, and $W_{i\rightarrow j}$ is the pump rate from $|i\rangle$ to $|j\rangle$.

To solve this system of equations, we begin with the consideration of some constraints to the system. First, the lifetime of $|1\rangle$ is infinitesimal compared with that of $|2\rangle$, so we can simplify the system by assuming that the moment an atom enters $|1\rangle$

it decays to $|2\rangle$ so the population of $|1\rangle$ is always zero. Mathematically, $\tau_1 \rightarrow 0$, so

$$\frac{d}{dt}n_1 \approx -\frac{n_1}{\delta} \quad (10.4)$$

in which δ is very small. Here we have assumed that the short lifetime of δ makes this term much larger than the pumping rate from the ground state. Solving this differential equation leads to

$$\ln n_1 = -\frac{t}{\delta} + C \quad (10.5)$$

$$n_1 = Ce^{-\frac{t}{\delta}}. \quad (10.6)$$

In steady state $t \rightarrow \infty$, so $n_1 \rightarrow 0$. Under this condition, the rate of pumping from the ground state to level $|1\rangle$ simply becomes the rate of pumping from the ground state to level $|2\rangle$. In steady state, $d/dt(n_1) = 0$, and since $n_1 = 0$, equation 10.2 can be eliminated to arrive at,

$$\frac{d}{dt}n_0 = -W_{0 \rightarrow 1}n_0 + \frac{n_2}{\tau_2} \quad (10.7)$$

$$\frac{d}{dt}n_2 = W_{0 \rightarrow 1}n_0 - \frac{n_2}{\tau_2}. \quad (10.8)$$

The next constraint to apply is that the total concentration of atoms n must be composed of the concentrations in the aforementioned states, or

$$n = \sum_{j=0}^2 n_j.$$

It has already been determined that $n_1 = 0$, so rewriting $n_2 = n - n_0$ in the first of our differential equations and applying the steady state condition that $\frac{d}{dt}n_i = 0$ results in

$$n_0 = \frac{n}{1 + \tau_2 W_{0 \rightarrow 1}} \quad (10.9)$$

$$n_2 = \frac{n\tau_2 W_{0 \rightarrow 1}}{1 + \tau_2 W_{0 \rightarrow 1}}. \quad (10.10)$$

We can put these in more familiar terms by observing that the pumping rate is just

$$W_{0 \rightarrow 1} = \frac{I\sigma}{h\nu}, \quad (10.11)$$

where I is the pump beam intensity in W/cm^2 , σ is the absorption cross section at the pump wavelength in cm^2 , and the product $h\nu$ is the pump photon energy in Joules. Making the further simplification of uniform pumping across the pump area A , we replace the pump intensity with the ratio of power to area $I = \frac{P}{A}$. Finally, since we are principally interested in the fraction of atoms in each of the states, we divide both sides by the total number density n to get

$$\frac{n_0}{n} = \frac{h\nu}{h\nu + \tau_2\sigma\frac{P}{A}} \quad (10.12)$$

$$\frac{n_2}{n} = \frac{\tau_2\sigma\frac{P}{A}}{h\nu + \tau_2\sigma\frac{P}{A}}. \quad (10.13)$$

10.4.2 Fluorescence Measurements

If we consider that fluorescence is simply the spontaneous emission of the excited state governed by the natural lifetime of the state, then the rate of fluorescence per unit volume must clearly be proportional to the population density n_2 of atoms in the excited state $|2\rangle$. As we continue pumping the crystal, we expect that the incremental fluorescence will drop off as fewer and fewer atoms are available in the ground state for populating $|2\rangle$. At the point where we reach inversion, $n_2 = n_0$, and since we assume that all atoms are in one of these two states, then $n_2 = \frac{n}{2}$. This is achieved when

$$\tau_2\sigma\frac{P}{A} = h\nu, \quad (10.14)$$

or,

$$P\sigma = \frac{Ah\nu}{\tau_2}. \quad (10.15)$$

At this point, the fluorescence should be half of the maximum obtainable fluorescence.

In order to evaluate the unknown parameters of the natural apatite crystal initially used as our laser gain medium, its transmission and fluorescence were measured as a function of incident pump laser power. The laser power at the site of the crystal was initially characterized using a NIST-traceable laser calorimeter and a high-precision HP multimeter. The setup for measuring the transmission and fluorescence of the laser crystal is shown in Figure 10.9. The laser end mirror was included in the measurement system to simulate the amount of pumping that the laser crystal would get in actual use. The pump beam waist was centered in the apatite crystal by observing the fluorescence as the pump focusing lens was translated toward and away from the apatite. When the beam was at best focus, the fluorescence reached a clear minimum, essentially where the absorption saturation of the crystal was at its maximum.

The transmitted red light was then reflected from a polished silicon wafer and focused on a silicon PV detector. The silicon wafer is strongly absorbing at the pump laser wavelength of 685 nm, allowing none of the pump light to register on the InGaAs detector behind it. The real part of the refractive index of silicon is about 3.8 at 685 nm, resulting in a Fresnel reflectivity of about 34%. The actual reflected efficiency, after reflection from the silicon wafer and transmitted through the detector window and collecting lens was measured to be 29.4%.

The silicon wafer has virtually no absorption at the fluorescence wavelengths of 1150-1170 nm however, allowing nearly 55% (after Fresnel reflections) to reach the InGaAs detector.

The fluorescence data are shown in Figure 10.10. The diode power output had been previously calibrated and shown to be almost perfectly linear with respect to input current above lasing threshold of 30 mA. When the beam was not focused in the crystal, the fluorescence increased nearly linearly with diode current. However, when properly focused in the apatite, the fluorescence yield began with the same slope as

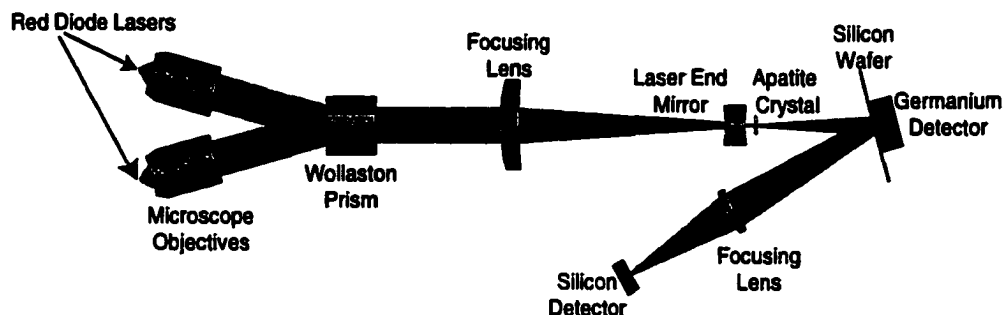


FIGURE 10.9. Setup for simultaneous measurements of fluorescence and transmission of apatite laser crystal. The silicon wafer is used as a dichroic beamsplitter, passing the fluorescence on to the germanium detector and reflecting the residual red pump beam to the lens which focusses it onto the silicon detector.

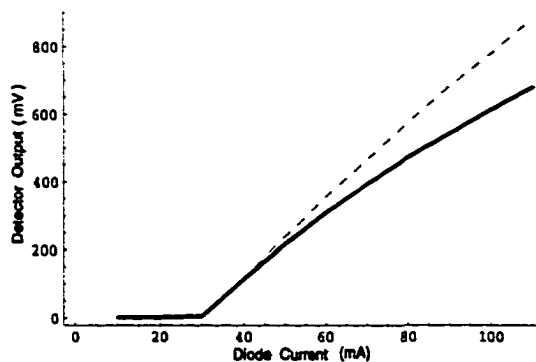


FIGURE 10.10. Fluorescence output from apatite crystal as a function of current to pump laser diodes. Diode output power is almost perfectly linear above threshold. The dashed curve is for the defocused beam in the crystal, while the solid curve shows the rolloff of fluorescence as a result of saturation.

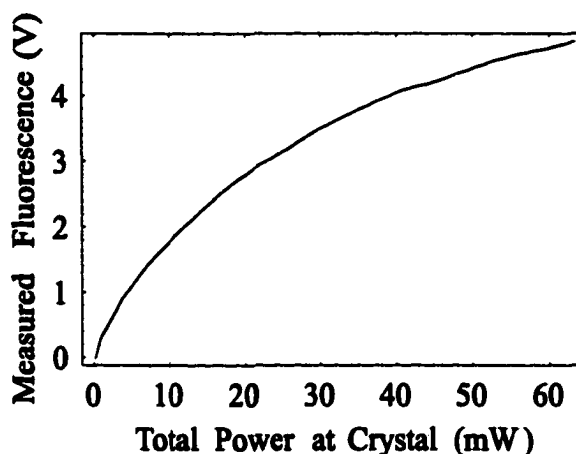


FIGURE 10.11. Measured fluorescence power from the apatite crystal as a function of laser power into the crystal. Data were obtained at maximum focus in the crystal.

the unfocussed case, but rapidly leveled out with increasing power, a clear indication of saturation.

Fluorescence as a function of laser power is plotted in Figure 10.11. This data should take on the same form as indicated in equation 10.13, though we are not yet sure of the scaling parameters to use. To obtain these scaling parameters, consider the slope of equation 10.13,

$$\frac{d}{dP} \left(\frac{n_2}{n} \right) = \frac{h\nu\tau_2\sigma/A}{(h\nu + \tau_2\sigma P/A)^2}. \quad (10.16)$$

With no incident power (i.e. $P = 0$) this simplifies to

$$\frac{d}{dP} \left(\frac{n_2}{n} \right)_{P=0} = \frac{\tau_2\sigma}{Ah\nu} \quad (10.17)$$

By observing the relaxation of the fluorescence from the excited state $|2\rangle$, we were able to determine that $\tau_2 = 550\mu\text{sec}$, the lifetime of the excited state. Direct observation of the pump spot yields a pumped area of $3.0 \times 10^{-5} \text{ cm}^2$. The wavelength of the pump laser is known to be 685 nm, so the only value remaining is the absorption

cross section, σ . Thus, the initial slope of our curve is

$$\frac{d}{dP} \left(\frac{n_2}{n} \right)_0 = \frac{430 \mu\text{sec } \sigma}{(3.0 \times 10^{-5} \text{cm}^2)(2.89 \times 10^{-19} \text{J})} \quad (10.18)$$

$$= 5.0 \times 10^{19} \sigma \text{W}^{-1} \text{cm}^{-2}. \quad (10.19)$$

In our data, the initial slope is 10.16 mV/mW. At the upper end of the power curve, the slope has dropped off to 2.19 mV/mW, a factor of 4.6 lower. Using this information, σ becomes apparent. Solving equation 10.16 for σ we get

$$\sigma = \frac{A}{\tau_2 P} \left(\sqrt{\frac{h\nu\tau_2/A}{\frac{d}{dP} \left(\frac{n_2}{n} \right)}} - h\nu \right) \quad (10.20)$$

$$= 4.9 \times 10^{-19} \text{cm}^2 \quad (10.21)$$

It is now possible to get an estimate of the number density of Mn^{5+} ions by evaluation of the total fluorescence yield of the crystal under pump illumination. For this estimate, we must assume that the fluorescence is isotropic, and that our germanium detector is uniform and standard in its responsivity. There are two paths by which the fluorescence can reach the detector, the direct path and the light reflected by the highly reflective end mirror. For the direct path, the emitted fluorescence must travel a distance d with a total transmission T . For the indirect path, the distance traveled (d') is slightly larger than d , and the transmission T' will be slightly less than T . The efficiency of photon collection, η is then given by

$$\eta = \frac{A_d}{4\pi d^2} T + \frac{A_d}{4\pi (d')^2} T' \quad (10.22)$$

where A_d is the area of the photodetector. The output voltage of the germanium detector for a flux of one photon per second should be

$$V_\gamma = \mathcal{R} G h\nu \quad (10.23)$$

where \mathcal{R} is the detector responsivity (A/W) at the fluorescence wavelength, and G is the detector amplifier gain (V/A). The total number of photons which will be emitted

per second from the apatite crystal under steady state pumping is

$$\frac{d\gamma}{dt} = Aln_2/\tau_2 \quad (10.24)$$

where the product of the pumped area A and length l give the pumped volume.

Combining these factors results in the steady-state voltage on the germanium detector

$$V_{ge} = \eta V_\gamma \frac{d\gamma}{dt} \quad (10.25)$$

$$= \left(\frac{A_d}{4\pi d^2} T + \frac{A_d}{4\pi (d')^2} T' \right) \mathcal{R} G h\nu A l n_2 / \tau_2 \quad (10.26)$$

Substituting for n_2 from equation 10.10 and solving for n yields a solution for the number density of Mn^{5+} atoms in the crystal. With a germanium detector area of $A_d = 0.2 \text{ cm}^2$ responsivity of $\mathcal{R} = 0.55 \text{ A/W}$, gain of $G = 10^5 \text{ V/A}$, transmission values of $T = .39$ and $T' = .34$ and distances of $d = 4 \text{ cm}$ and $d' = 5 \text{ cm}$ we get a detector voltage of 392 mV at a power of 55.5 mW. This results in

$$n = \frac{4\pi (h\nu + \tau_2 \sigma P/A) V_{ge}}{A_d \left(\frac{T}{d^2} + \frac{T'}{(d')^2} \right) \mathcal{R} G h\nu l \sigma P} \quad (10.27)$$

$$= 7.3 \times 10^{18} \text{ cm}^{-3} \quad (10.28)$$

This value is about 35% less than that obtained by ICP analysis, but nevertheless it is good as an approximation based on the assumptions made. To check the fit, comparison of the derived function and the data is shown in Figure 10.12. The fit, while not perfect, demonstrates a general agreement with the observations.

10.4.3 Transmission Data

The values just obtained can now be used to check the degree to which the entire analysis is valid by using them to model the transmission of the pump beam through the laser crystal. Whereas fluorescence is dependent solely on the number n_2 of atoms in the excited state $|2\rangle$, the transmission is dependent on $n_0 - n_1$, the population difference between the excited state $|1\rangle$ and ground state $|0\rangle$ of the pumping transition.

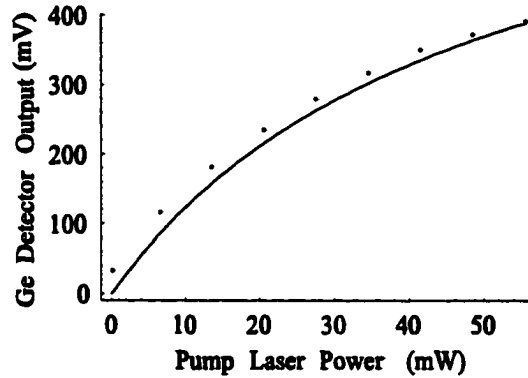


FIGURE 10.12. Comparison of fluorescence data and functional fit.

Since our model maintains that n_1 is always near zero, then the internal transmission (i.e. not accounting for Fresnel losses at the surfaces) is just

$$T_{ap} = e^{-\alpha_0 l \frac{n_0}{n}} \quad (10.29)$$

where α_0 is the small-signal (unsaturated) absorption coefficient, and l is the length of the crystal. The unsaturated absorption coefficient is just

$$\alpha_0 = n\sigma \quad (10.30)$$

so the transmission as a function of power can be written

$$T(P) = e^{-\alpha(P)l} \quad (10.31)$$

$$= e^{-\alpha_0 \frac{n_0(P)}{n} l} \quad (10.32)$$

$$= e^{-n\sigma \frac{h\nu}{h\nu + r_2\sigma} \frac{P}{\hbar} l} \quad (10.33)$$

Thus, taking into account all of the potential losses and response of the silicon detector, it is expected that the silicon response should be

$$i(P) = PT(P)T_{Si}\mathcal{R}_{Si} \quad (10.34)$$

$$= Pe^{-n\sigma \frac{h\nu}{h\nu + r_2\sigma} \frac{P}{\hbar} l} T_{Si}\mathcal{R}_{Si} \quad (10.35)$$

With estimates of $T_{Si} = 0.27$ and $\mathcal{R}_{Si} = 0.4$ A/W we get the curve shown in Figure 10.13.

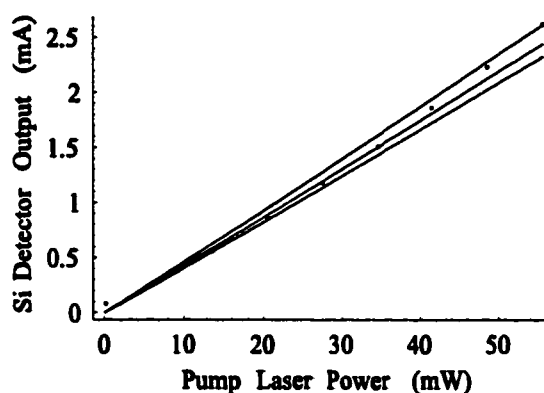


FIGURE 10.13. Comparison of transmission data and functional fit.

The function overestimates the silicon detector response by a factor of about 2.2. This is not surprising given the lack of absolute knowledge of detector responsivity, system transmission at 685 nm, and collection efficiency of the lens. When the functional curve is normalized by this constant, the data can be compared with the functional dependence as shown in Figure 10.13.

10.4.4 Thermal Stress Analysis

All of the work involved in developing an apatite laser is useless for guide star purposes unless a significant amount of power can be wrung from the laser crystal. The power can be limited by several factors, including the 'thermal shock' which the apatite host material is capable of withstanding.

The thermal shock parameter of a laser crystal is a function of the speed with which the heat deposited in the crystal can be conducted away, the thermal expansion and elastic coefficients of the material, and the maximum tensile stress that the crystal can withstand before breaking. This latter parameter, maximum stress, is dependent upon the surface finish of the material, and can vary by factors of 2-3. Furthermore, dislocations and impurities as frequently found in natural crystals can also significantly lower this maximum tensile stress value.

In the analysis published by Koechner [53] a cylindrically symmetric laser rod pumped by a Gaussian beam will experience a quadratically varying temperature profile to the boundary of the rod. Radial, tangential and axial stresses are induced in the rod as a result of the rod's non-uniform thermal expansion. The stress fracture limit (the amount of power that can be dissipated in the rod before fracture occurs) is

$$P_a = 8\pi l R \quad (10.36)$$

where l is the length of the crystal (.118 cm), and R is a "thermal shock parameter" given by

$$R = \frac{K(1-\nu)}{\alpha E} \sigma_{max} \quad (10.37)$$

where K is the thermal conductivity, ν is Poisson's ratio, α is the expansion coefficient, E is the Elastic Modulus, also known as "Young's Modulus", and σ_{max} is the maximum tensile strength of the laser crystal.

With the apatite laser, we lose on several fronts in the laser development. First, the quantum loss is over 40%, so that nearly half of our absorbed power results in heat which must be dissipated. Second, the thermal conductivity of apatite is only $2.0 \text{ W m}^{-1} \text{ C}^{-1}$. The thermal expansion coefficient of apatite is a relatively high 1.0×10^{-5} . Finally, the tensile strength of apatite appears to be significantly less than $2.0 \times 10^8 \text{ Pa}$ (though this number needs to be verified experimentally).

Poisson's ratio for apatite is $\nu = .26$ and the elastic modulus is $E = 115 \text{ GPa}$. Combining all of these yields a thermal shock parameter of $R = 2.65 \text{ W/m}$, less than 1/3 that of YAG. Mind that because of the lack of knowledge of the maximum tensile stress, this is an upper limit. The actual value is likely to be closer to $R = 1 \text{ W/m}$.

The maximum amount of power we can then deposit into the laser crystal is then $P_a = 7.8 \text{ W}$, which means a maximum pumping of around 20W. We are nowhere near

this limit in our experiment, and will not reach it for quite some time using red diode lasers as a pump source.

10.4.5 Lasing Efforts

In trying to get fluorapatite to lase, we were facing several difficult problems at one time. First, the material is identified as a three-level material, raising the pumping requirements significantly above those of a four-level material to reach inversion. Second, we were trying to pump the material with polarization-coupled diode lasers putting a maximum combined power of 80 mW into the crystal. Third, the polarization coupling of the pump lasers meant that we lost that degree of freedom in optimizing pump absorption for lasing. Fourth, the laser diodes were designed to run CW, preventing us from reaching threshold with high-intensity pulses. Finally, the laser material was a natural material, with unknown impurities and internal flaws which scatter the lasing beam. Given all of this, obtaining lasing was 'a long shot'.

To maximize the effectiveness of our rather feeble pump system, we developed a hemispherical cavity just inside the edge of marginal stability. The laser crystal was physically attached to the flat mirror of the cavity with a thin film of high index ($n = 1.65$) epoxy. This produced the smallest possible beam mode, into which we focussed the pump lasers. To minimize the cavity mode further, we used a special high-reflector mirror with a 9.3 mm radius of curvature, which brought the mode diameter down to under 40 μ m, assuming the ability to bring the mirror to within 100 μ m of the stability criterion (Figure 10.14).

To minimize the losses in the cavity, we AR coated the apatite crystal with a two-layer thin film coating designed by the author and applied with the help of Dr. Heidi Ruffner of Sandia National Laboratories to reach zero-reflectance. The coating materials were Al_2O_3 and ZrO_2 , both of which are hard and robust. Laboratory tests confirmed the thickness of the design layers, and measurements of the surface

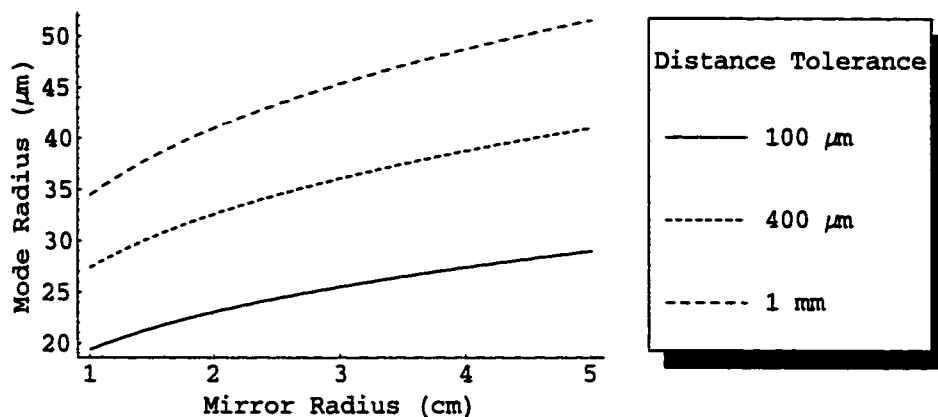


FIGURE 10.14. Mode radius for a hemispherical cavity with a spherical mirror of radius R , assuming alignment to within 1.0, 0.4 and 0.1 mm of marginal stability.

reflectance confirmed the effectiveness of the coatings. We attempted to use cavities in which both mirrors were HR mirrors to eliminate the bulk of the output coupling loss. Spectral transmission characteristics of all mirrors used confirmed their high reflectance nature at the fluorescence wavelengths.

In spite of our best efforts, clear indications of lasing were never observed.

10.5 Discussion and Conclusion

Given the difficulty of the task, it is not surprising that lasing was not observed. Previous successes at getting lasing from the Mn^{5+} ion used pulsed dye lasers for excitation at much higher peak power than our diodes afforded. Furthermore, all of the crystals made to lase were synthetically produced under known quality control conditions. Even then, the 'successful' efforts showed very low slope efficiencies which we later found were most likely attributable to excited state absorption [61]. Manaa *et al.* indicated that the transient absorption that they observed in Mn:SVAP was most likely associated with the transition from the metastable 1E excited state to the upper level 1T_2 and 1T_1 states. While this does not necessarily preclude an apatite laser from lasing, ESA raises the threshold requirement and strongly limits power

extraction from the gain material. While Mn^{5+} in BCAP may not suffer the same fate as these other materials, it appears much less likely that further research into it will be fruitful.

Part IV
The Road Ahead

Chapter 11

NEW SODIUM LASER CONCEPTS

I must go up to the hills again,
To the lonely hills and the sky,
And all I ask is an eight meter 'scope
And a star to steer her by.

-WTR (with apologies to John Masfield)

Throughout the course of this research, and especially during the final phases of analysis and documentation, I have developed some ideas for solid-state guide star lasers which may prove to be of some merit. In addition, in researching the background and development of several of the existing and planned laser systems, I have come across information that may well be worth pursuing in development of an alternative guide star laser. Each of the three concepts presented needs further development to optimize the design, and in some cases experimentation to validate the theory.

11.1 CW fiber laser

A CW fiber-laser-pumped Raman fiber laser, originally suggested in 1997 by James Murray[73], should be revisited at this point because of advances in these technologies driven by the telecommunications industry. These laser systems begin with a 915 nm diode-pumped double-clad Yb fiber laser emitting at 1115 nm. A fiber Bragg grating (FBG)¹ is spliced onto the end of the double-clad fiber. The FBG has a periodic change in refractive index throughout the fiber which is small in magnitude, but multiplied by the small Fresnel reflections of many repeated periods can generate

¹Some authors also use the term Distributed Bragg Reflector or DBR.

high reflectivities at wavelengths determined by the grating period [1]. The grating length determines the spectral bandwidth of the reflector, and the number of periods and differential index variation determine the reflectivity. The output of this fiber laser is sent into a fiber Raman laser which makes use of FBGs at both ends to circulate and stimulate Raman emission at the wavelength of interest, 1178 nm. The output of this laser was to be doubled in a doubling crystal in free-space optics, and projected onto the sky.

Though sound in concept, the idea never gained hold. The problems at the time of conception were (1) writing a FBG with sufficiently narrow spectral reflectivity to generate lasing within the spectral profile of the Doppler-broadened sodium, (2) availability of double-clad fiber lasers, and (3) availability of high-brightness laser pumping systems.

Since that time, the rapid growth in telecommunications has spurred the development of high-brightness pumping systems for double-clad fiber lasers and the development of high-power Raman fiber lasers. An appropriate fiber laser is available commercially from B&W Tek, Inc. [15] [16]. They claim it is capable of over 20 W of output at 1115 nm, with a bandwidth of 2 nm and a center frequency accuracy of ± 2 nm. They are capable of custom work with supplied Bragg gratings, though the delivery time would be extended to 5-6 months.

Raman-shifting using germano-silicate fiber was originally suggested [73], making use of a broad Raman peak centered at 418 cm^{-1} . Shifting a laser at 1115 nm to 1178 nm requires a shift of 479.6 cm^{-1} , which is much closer to the 490 cm^{-1} peak which dominates the Raman gain profile in high average power pumping, as shown in Figure 11.1 [1]. One of the advantages of this laser concept expounded by Murray [73] is the scalability to high power. Indeed, high output power from double clad fiber lasers has already been demonstrated Raman fiber lasers with CW output powers exceeding 1 W have been demonstrated [83] [51] [52], with powers ranging from 20.4 Watts at 1101 nm to 8.5 Watts after multiple Stokes processes to 1472 nm

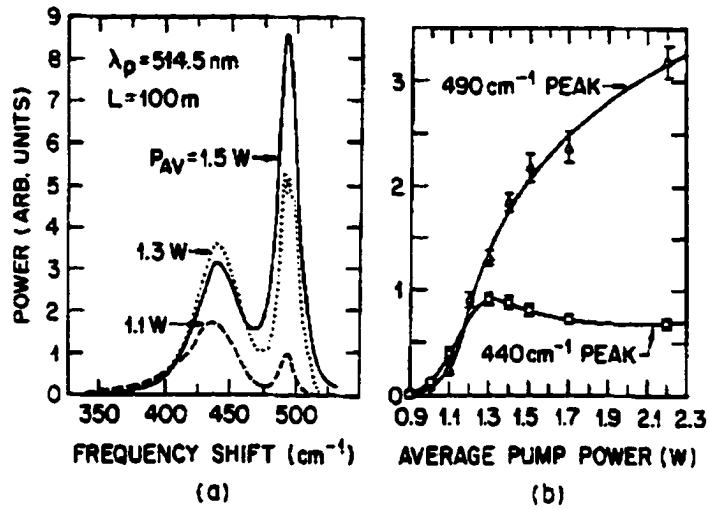


FIGURE 11.1. Raman gain spectrum of a fused silica fiber. At low pump power, the 440 cm^{-1} peak dominates the spectrum, but at higher power the 490 cm^{-1} peak rapidly overwhelms it.

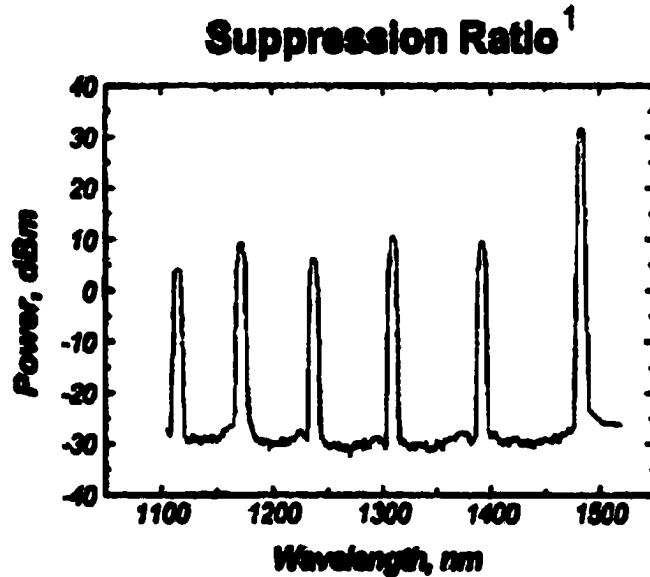


FIGURE 11.2. Spectral output of a fiber Raman laser designed to operate at 1580 nm . The design reflects the intermediate Raman orders back into the cavity, stimulating multiple-Stokes shifts. The output power for the desired 1580 nm line dominates the intermediate orders.

[55]. Since each Raman process necessarily involves a loss of power, higher power would be expected at wavelengths nearer the pump band. Recently B&W Tek, Inc. began selling high-power multi-Stokes-shifted Raman fiber lasers capable of high-efficiency, high-power conversion. To maintain the conversion efficiency, the FBG must recirculate the light out to the desired wavelength, allowing the Stokes waves to multiply cascade. An example of multiply-cascaded Raman laser output, designed to suppress intermediate Stokes shifts out to 1580 nm, is shown in Figure 11.2. Note that the first Stokes shift brings the laser very close to our desired wavelength of 1178 nm. With 20 W of pump power at 1115 nm (1.1×10^{20} photons) resulting in over 5 W of output power at 1580 nm (4.0^{19} photons), a multiply-cascaded photon efficiency of 36% is achieved. Assuming equal losses at each of the five Stokes-shifts implies a potential efficiency per shift of 81%, and an output power at the first Stokes shift of 15 W. Assuming a very conservative doubling efficiency of 40% results in 6 W of CW power at 589 nm.

The most challenging requirement for impressing this technology into service as a guide star laser is matching the spectral width of the sodium line. To restrict the laser output to the narrow 1 GHz band deemed optimum for sodium excitation, the spectral bandwidth of the pump laser and Raman laser must be controlled by the distributed Bragg reflectors constituting the feedback reflectors of these lasers. Using simple scaling arguments, we can estimate the length of the required Bragg reflector; since the mode separation of a laser is given by

$$\Delta\nu = \frac{c}{2L} \quad (11.1)$$

where L is the length of the cavity, we can estimate that for a spectral output bandwidth of 1 GHz, we need distributed feedback over a length of $L = 0.15\text{m}$, or 15 cm. Narrow-band lasers operating at high power are approaching these limits [54]. In one experiment a 10 cm grating was written into a fiber, resulting in a peak reflectivity of 99.5%, and a bandwidth of 0.057 nm (7 GHz). In a similar experiment, a 10 cm

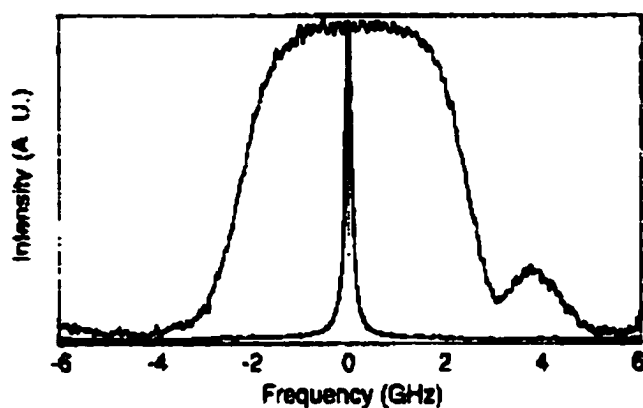


FIGURE 11.3. Spectral reflectivity of a 10 cm narrow-band fiber Bragg grating from [54]. A 3-dB bandwidth of approximately 5 GHz is shown in the outer envelope, and the narrow spectrally-extracted output of a mode-locked fiber laser.

grating with apodization was written, resulting in a reduced 3-dB bandwidth of 0.04 nm (5 GHz) with a 92% peak reflectivity shown in Figure 11.3.

All of this implies that a 6 W CW guide star laser with a spectral broadening of 5 GHz is currently feasible. The power and duty cycle of this laser are very attractive, and can be had at a low cost and with very high power efficiency, reliability, and maintainability. The bandwidth of this laser is still too broad however, wasting most of the power in the wings outside of the sodium resonance lines. Longer FBGs may continue to bring the bandwidth down to more appropriate levels, at which this becomes a most attractive option.

11.2 Interleaved Q-switched Lasers

In Chapter 10 we introduced the concept of using multiple Q-switched lasers, temporally interleaved to generate an effective sodium guide star. Nonlinear laser interactions such as frequency doubling and Raman shifting generally require high intensity pump fields to drive the molecular responses of materials into the nonlinear regime.

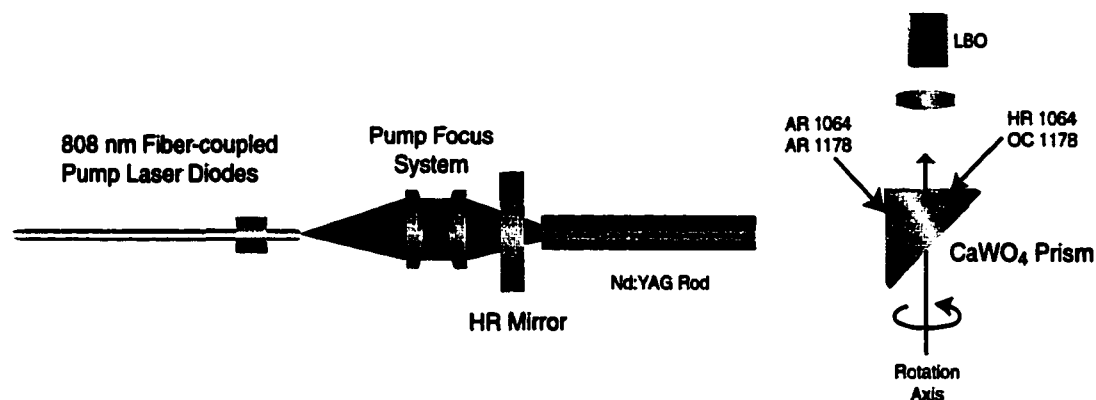


FIGURE 11.4. Conceptual design for Q-switched laser utilizing rotating mechanical Q-switch sequentially accessing multiple laser cavities (side view).

Q-switching allows the laser material to be pumped to high gain levels producing the short (≈ 10 nsec) intense pulses to drive these nonlinear processes. However, because of the relatively low saturation limit of the sodium layer, the very method used to produce light at the right frequency prevents efficient generation of a bright guide star with a Q-switched laser.

A solution to this dilemma is to make use of the abundant 'dead time' between the pulses of a Q-switched laser by firing other Q-switched lasers. By interleaving multiple independent lasers, the brightness of the guide star can be linearly increased by the number of interleaved lasers. Each of these lasers can be held to a particular frequency by injection seeding, obviating the need of redundant tuning control.

My concept for such a system is shown in Figure 11.4. This design hinges on a mechanical Q-switch system in which the output coupler is a right-angle prism made of CaWO_4 to generate an intracavity Raman wave. The vertical face of this prism has an antireflection coating applied to prevent losses at the fundamental 1064 nm Nd^{3+} frequency as well as the shifted Raman frequency at 1178 nm. The horizontal top surface of the CaWO_4 prism has an output coupler coating applied to it which recirculates the Nd^{3+} frequency and couples out a fraction of the 1178 nm light. The high refractive index of CaWO_4 (1.82 nm) assures that the total internal reflection

from the hypotenuse of the prism is lossless. Q-switching of the cavity is performed by rapidly rotating the prism so that it occasionally aligns with the remainder of the cavity, creating the high-Q situation which allows the laser pulse to fire.

Multiple laser cavities can be aligned radially about the Q-switching element, such that each fires in turn as the prism comes into alignment with that cavity (Figure 11.5). The number of lasers which can be temporally interleaved in this way is limited only by the cavity design and the interference of mounts for adjacent cavities. In the diagram of Figure 11.5 we envision 25 separate laser cavities. All of these cavities are held to the same spectral line by an injection seeding system in which a small amount of the tuned output of the previous laser is reflected back into the subsequent laser by a partial reflector or pick-off mirror.

The rotation rate of the Q-switch prism is limited only by the efficient Q-switching rate of the various gain materials used. Nd:YAG operates well when Q-switched at 5-10 kHz, so these rotation rates are desirable. Modern DC brushless motors are capable of speeds of 50,000 to 150,000 rpm, resulting in Q-switching rates of 1000-2500 Hz. Multiple output prisms could ultimately be used to increase this Q-switching rate, but this adds alignment complexity and moment of inertia to the rapidly rotating portion of the system, and should not be attempted in the early stages. Possible electro-optical multiplexing of the output beams of multiple systems could be used to increase the duty cycle further in later stages.

This design has several notable advantages. It can operate near the temporal regime appropriate for efficient Q-switching of Nd:YAG lasers. The mechanical interleaving design is simple in principle as well as in practice; no sequencing electronics are required, nor are synchronization systems for aligning a rotating mirror to the rapidly-fired lasers. The system can be made economically; the expensive specialized Raman prism output coupler is common to all of the lasers, while the common Nd:YAG laser rods, pump laser diodes and HR mirrors take advantage of economies of scale. Through the redundancy of much of the cavity, some degree of fault-tolerance

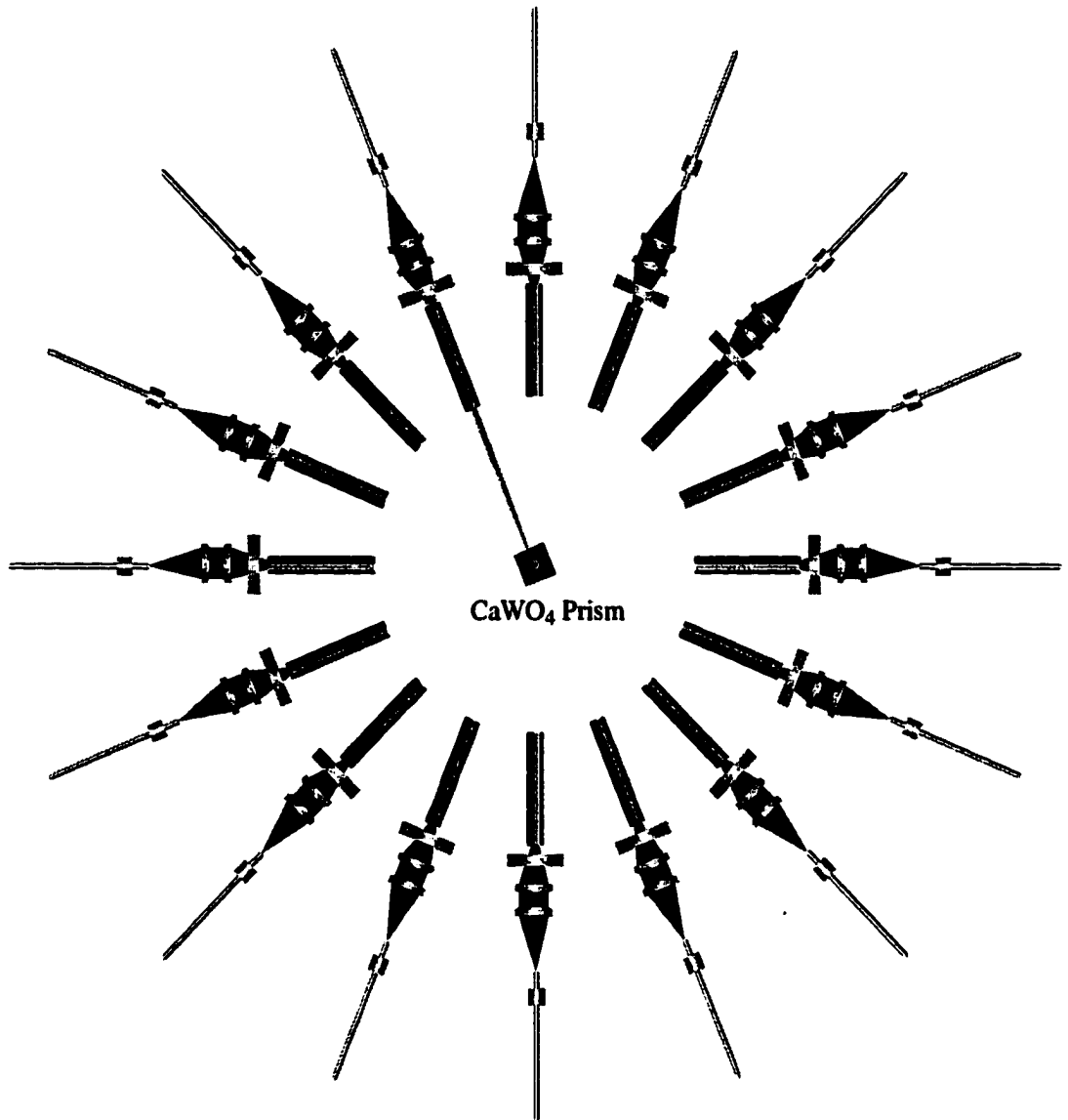


FIGURE 11.5. Conceptual design for Q-switched laser system employing multiple cavities (top view). The output coupler and Raman crystal are in the center, and Q-switch the output of each of the individual lasers sequentially through rotation about an axis normal to the page. The output of each beam is aligned with the prism rotation axis.

is achieved such that if a pump diode dies the system will still operate efficiently and effectively until the part can be replaced. Finally, each of the individual lasers will provide high-intensity Q-switches which will saturate the sodium layer, so each can be reduced in power, relieving issues of thermal lensing and birefringence with which they must otherwise contend.

This laser constitutes a rather 'brute force' approach to development of a guide star laser. The technology it employs is not particularly new, and because of the still-low duty cycle, far from optimum. However, it can be developed with existing parts, and be expected to work reliably. Proper scaling of this laser system might result in approximately 50,000 pulses per second, each of which is approximately 10 nsec long and saturates the sodium layer. By projecting this into a 2500 cm² spot, with full saturation we would excite about 10^{12} atoms with each pulse. For 50,000 pulses per second, roughly 5×10^{16} photons per second would be absorbed, or on the order of 20 mW, considerably less than our dye laser. Thus, to be considered viable, a method of higher-order interleaving of pulses must ultimately be employed for such a design.

11.3 Diamond Color Center Laser

In 1985 S. C. Rand and L. G. DeShazer of Hughes Research Laboratory developed the first diamond color center laser, using natural diamond samples with radiationally-induced H3 color centers [84]. The properties of H3 color centers in diamond, in combination with the advantages of diamond host material make this laser particularly exciting in its potential application to sodium guide star lasers.

Natural diamonds exist in a number of colors because of the variety of impurity atoms and color centers that they contain. Of particular interest to the laser community are color centers based on the most common form of diamond impurity, nitrogen. One of the potential color centers is the H3 color center, which forms when nitrogen

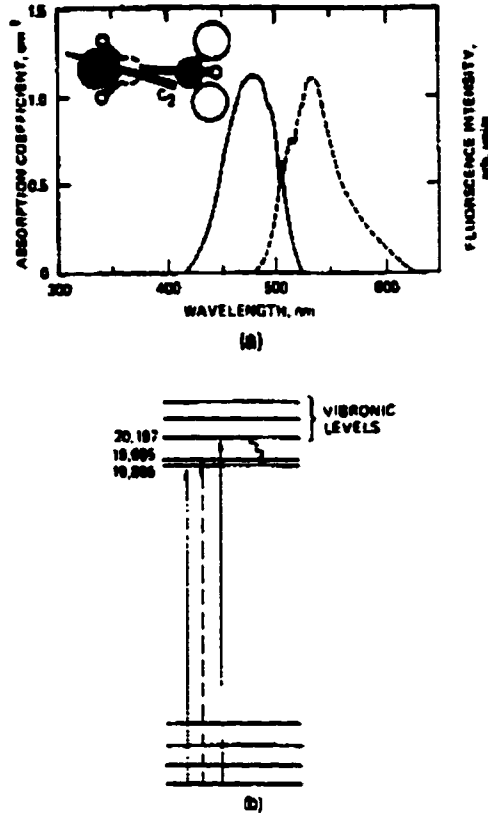


FIGURE 11.6. Absorption (left) and emission spectra of the H3 color center in diamond (a), and the associated pump and emission energy levels (b)(after [84]).

atoms replace carbon atoms in the diamond structure. These color centers can be generated in high concentrations in diamond by exposure to 1-2 MeV electrons and subsequent high-temperature (1200 K) annealing [84].

The absorption and emission bands of a natural diamond sample with induced H3 centers is shown in Figure 11.6. The broad absorption peak at 480 nm makes it ideal for pumping with the 488 nm line of Ar⁺, while the broad fluorescence curve indicates the potential for this laser to be tuned between wavelengths from 500 nm to beyond 600 nm. At 589 nm the fluorescence intensity is about 20% of the peak fluorescence intensity found at 531 nm.

In their experiments with diamond samples, Rand and DeShazer noticed that

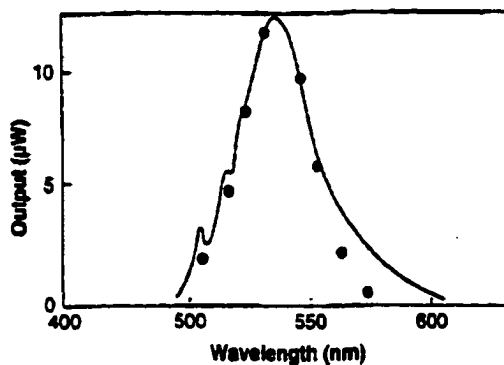


FIGURE 11.7. Spectral data points for tuned diamond color center laser (points) compared with H3 color center fluorescence spectrum.

when pumping with 4 nsec pulses from a $\lambda_p = 480$ nm coumarin dye laser, up to 171 μJ of laser emission at 530 nm occurred as a result of feedback from Fresnel reflections between the flat, uncoated surfaces of the sample. The pump intensity required to reach threshold was reported to be 8 MW/cm^2 for their 1.85 mm thick sample, with a slope efficiency of 13.5% just above threshold. The lasing occurred at room temperature (295 K), in contrast with the requirement of many alkali-halides for low temperature operation. They further calculated that the threshold inversion should be $\Delta N = 9.8 \times 10^{15} \text{ cm}^{-3}$ in a cavity with only 4% loss, allowing CW argon ion laser pumping.

Since this initial report, there has been little progress on diamond color center lasers. A few articles expounding the potential of this material for replacing high-power dye lasers have been published [85] [111]. In unpublished experiments, researchers at Itami Research Laboratories of Sumitomo Electric Corporation in Japan generated high densities of H3 color centers in natural and synthetic diamonds, and used these to obtain yellow lasing output (reported in [85]). In an unpublished master's thesis (reported in [85]), G. Taylor at the University of Strathclyde obtained CW lasing of synthetic H3 diamond color center material by pumping with up to 2 W of argon ion laser power, and tuned the output from approximately 505 nm to

570 nm, though the slope efficiency was disappointingly low (6.6×10^{-4} %). The tuning data from Taylor are reproduced in Figure 11.7. The researchers at Sumitomo have reportedly made synthetic H3 diamonds with very bright photoluminescence, but lasing of these samples was not reported [85].

The properties of diamond are ideal for development of a high-power laser material. The hardest of all natural materials (Young's Modulus 1.05×10^6 N cm⁻² [77]), it is impervious to scratches once it is lapped and polished. The clarity of good diamond crystals and extremely broad transmission band (0.25 μ m - 80 μ m [43] permit the use of diamond in many optical situations. The space group of diamond has T_d symmetry, so no birefringence is observed in the crystals.

However, where diamond really stands out as a material is in its thermal properties, which are essential for scaling a system to high power. Diamond has the highest thermal conductivity of any known material (2000-2500 W/m K or about 5 times that of copper [31]) allowing for extremely rapid heat removal from the pumped crystal. The high conductivity will prevent a substantial thermal gradient from forming in the material, even at high pump powers. With an extremely low thermal expansion coefficient of 0.8×10^{-6} /K and low dn/dT of 4.04×10^{-6} /K, any minute thermal gradient that exists will have no significant thermal lensing effect.

Clearly this laser is much less mature than the others described. A complete understanding of the gain material through pump-probe measurements should be undertaken to gauge its suitability for lasing at 589 nm. However, because of its potential to lase directly at the desired wavelength, its broad tunability from green through red, the availability of powerful pump sources, and its inherent scalability to high power, this laser may ultimately be one of the best prospects for a good guide star laser. It would operate continuous wave, and can be tuned across the entire transition of sodium. Its lasing bandwidth can be tailored to the sodium Doppler spectrum.

The diamond color center laser may have a development edge over the other tech-

nologies because of its potential for use in many other fields in which high-power tunable visible lasers are necessary. The astronomy community is neither affluent enough, nor large enough to be a significant driver in development of new laser materials. However, femtosecond spectroscopy, LIDAR systems, effluent monitoring systems are, to mention just a few. The prospect of a laser system with the tunability of and R6G dye laser, but free of the disadvantages of the carcinogenic, liquid dye gain medium would be of considerable interest to these and other users of dye laser systems. Demonstration of the concept could ultimately drive the development of high power diamond color center lasers, allowing the astronomical community to reap the benefits with relatively little research expenditure.

11.4 Conclusions

The research presented in this dissertation has resulted in information which will help to ultimately choose from among the several paths accessible to development of a sodium guide star laser. We have demonstrated a few technologies which, with sufficient resources and funding, will ultimately be capable of producing a useable sodium guide star. In addition, we have shown that some of the technologies considered are *not* good candidates, at least in their current state of development.

The research on Raman lasers operating in the infrared has shown the potential for production of a good sodium guide star. The intracavity Raman laser demonstrated with CaWO_4 shifting the fundamental 1064 nm line of Nd:YAG has been shown to be viable for production of light which can be doubled and tuned to the sodium wavelength. We have shown that the tuning can be minimized by thermal tuning of the Nd:YAG laser. While thermally and mechanically difficult, we have developed a Nd:YAG laser design which has been shown to operate continuously at power greater than 6 W over a wide range of temperature. The result is that the demonstrated shift of intracavity CaWO_4 would be centered at 1178 nm, significantly boosting the power

available for doubling to sodium guide star wavelengths. The compositional tuning of the Nd:YAG laser was disappointing in its results, resulting in energy spread over the spectrum which would ultimately be unavailable for concentration at sodium guide star wavelengths.

Color center lasers offer an attractive alternative to currently available guide star lasers. Color center lasers based on the F_2^- color center in LiF have high gain in the infrared, and can be tuned to 1178 nm in a manner similar to the tuning of dye lasers. We have shown the ability to tune and double the output of a Q-switched color center laser, resulting in light at the 589 nm sodium wavelength. Combined with the potential for high average power shown by other researchers, this is a very attractive option for guide star laser development. A less mature, but potentially exciting color center laser based on H3 color centers in diamond could operate directly at the 589 nm sodium wavelength, obviating the need for pulsing to drive nonlinear processes. The advantages of diamond as an optical material for scaling to high power are ideal, making experimentation with this material a recommended priority. A potentially high power solid state laser, tunable over a wide range of visible wavelengths, has applications far beyond guide star production, offering the possibility of leverage from other sources for advanced laser development.

Appendix A

ATOMIC LEVELS OF Mn^{5+}

A.1 Theory of the Mn^{5+} Free Ion

First we need to understand the Mn^{5+} ion free of any external perturbing field. The ion is comprised of a filled argon shell and two $3d$ electrons; the filled shell tends to act as a spherically symmetric nucleus of effective charge Z_{eff} , with zero spin and zero angular momentum. This leaves us free to concentrate on the properties of the $3d$ valence electrons.

A single $3d$ electron has principal quantum number $n = 3$, orbital angular momentum quantum number $l = 2$, and spin angular momentum quantum number $s = \frac{1}{2}$. The actual angular momentum of an electron is a vector \mathbf{L} which has strictly quantized magnitude and direction limitations. The angular momentum operator must therefore be a vector operator, and is defined by

$$\hat{\mathbf{L}} = e_x \hat{L}_x + e_y \hat{L}_y + e_z \hat{L}_z \quad (\text{A.1})$$

in a three-dimensional Cartesian basis (e_x, e_y, e_z) .

Measurements of the square of the magnitude of the orbital angular momentum for a single electron in an angular momentum state l yields

$$\hat{L}^2 |l\rangle = l(l+1)\hbar^2 |l\rangle \quad (\text{A.2})$$

where \hat{L}^2 is the angular momentum magnitude (squared) operator and $|l\rangle$ is an eigenstate of the system in Dirac notation. For the d electron with $l = 2$, we obtain a result of

$$\hat{L}^2|2\rangle = 6\hbar^2|2\rangle \quad (\text{A.3})$$

In other words, measurement of the orbital angular momentum of a single d electron yields a value of $\sqrt{6}\hbar$.

Furthermore, this single eigenvalue can be obtained for $(2l + 1) = 5$ different, independent, orthogonal eigenfunctions. Each of these independent eigenfunctions 'belongs' to the same eigenvalue, and correspond to different orientations of the angular momentum vector with respect to some given direction, commonly the \hat{z} axis.

Thus, a complete description of the orbital angular momentum of the $3d$ electron must include another parameter to distinguish among these five distinct but degenerate eigenfunctions. Such a parameter is afforded by measuring the projection of the orbital angular momentum vector onto the \hat{z} axis. The operator for doing this is commonly referred to as \hat{L}_z , and the results of this measurement can take on the values

$$\hat{L}_z|l, m_l\rangle = \hbar m_l|l, m_l\rangle \quad (\text{A.4})$$

where $m_l \in \{-l, -l+1, \dots, l-1, l\}$. In addition to an orbital angular momentum \mathbf{L} , the electron has an intrinsic spin angular momentum \mathbf{S} , the orientation of which relative to \mathbf{L} will affect the eigenstates and eigenvalues of the system. This spin angular momentum, while distinct from the orbital angular momentum, nonetheless acts in much the same way. Its magnitude (squared) is obtained from the \hat{S}^2 operator, and similar to the eigenvalues obtained from \hat{L}^2 , give a magnitude of

$$\hat{S}^2|s\rangle = s(s+1)\hbar^2|s\rangle \quad (\text{A.5})$$

with a spin degeneracy of $(2s+1)$. The degenerate eigenfunctions, similar to those of orbital angular momentum, can likewise be distinguished by operating with a \hat{z} projection operator \hat{S}_z , resulting in

$$\hat{S}_z|s, m_s\rangle = \hbar m_s|s, m_s\rangle \quad (\text{A.6})$$

where $m_s \in \{-s, -s+1, \dots, s-1, s\}$.

One significant difference between orbital angular momentum \mathbf{L} and spin angular momentum \mathbf{S} is that, while l values are restricted to integer values (and so, likewise must be m_l values), the s values can take on either integral or odd-half-integral values (i.e. $\frac{1}{2}, \frac{3}{2}, \frac{5}{2}, \dots$). The former case is true for particles for which the wavefunction is symmetric under the exchange operator $\hat{\Xi}$, or ¹

$$\hat{\Xi}|\varphi_S\rangle = +1|\varphi_S\rangle \quad (\text{A.7})$$

while the latter case is true for particles with wavefunctions which are antisymmetric under exchange:

$$\hat{\Xi}|\varphi_A\rangle = -1|\varphi_A\rangle. \quad (\text{A.8})$$

In the case of an electron with spin $s = \frac{1}{2}$, the spin degeneracy is $(2(\frac{1}{2}) + 1) = 2$, corresponding to spin states $m_s = \pm\frac{1}{2}$. Thus, for a single $3d$ electron we might expect five-fold degeneracy from the five $|l, m_l\rangle$ eigenstates, and two-fold degeneracy from the two m_s values at each of these eigenstates for a product of 10 degenerate eigenstates. However, in so assuming, we have neglected any interaction between the orbital and spin angular momenta of the electron. This interaction, known as L-S coupling or

¹Here we use the symbols φ_S and φ_A to represent eigenfunctions which are respectively symmetric and antisymmetric under exchange.

Russell-Saunders coupling, actually does affect the energy levels of the electron. One may think of the energy differences as resulting from situations in which \mathbf{L} and \mathbf{S} are aligned principally parallel or antiparallel.

This spin-orbit interaction leads to new levels which correspond to different combinations of the \mathbf{L} and \mathbf{S} vectors for the electron. This is studied by creating a new general angular momentum vector \mathbf{J} which is the vector sum of the individual orbital and spin angular momentum vectors. It is this \mathbf{J} operator which will be of primary importance in establishing the eigenvalues and eigenfunctions for the time-independent Schrödinger equation.

As we did before for orbital and spin angular momenta, we can determine the magnitude of the electron's total angular momentum by operating with the \hat{J}^2 operator, to get

$$\hat{J}^2|j\rangle = j(j+1)\hbar^2|j\rangle \quad (\text{A.9})$$

where $j \in \{|l-s|, |l-s+1|, \dots, |l+s-1|, l+s\}$, and the \hat{z} projection operator

$$\hat{J}_z|j\rangle = m_j\hbar|j\rangle. \quad (\text{A.10})$$

Since $\mathbf{J} = \mathbf{L} + \mathbf{S}$, then

$$\hat{J}^2 = \hat{L}^2 + 2\mathbf{L}\cdot\mathbf{S} + \hat{S}^2 \quad (\text{A.11})$$

so the magnitude of $\mathbf{L}\cdot\mathbf{S}$ is given by

$$|\mathbf{L}\cdot\mathbf{S}| = \frac{1}{2} \left(\hat{J}^2 - \hat{L}^2 - \hat{S}^2 \right) \quad (\text{A.12})$$

which will be useful later in evaluating the spin-state splitting.

We now have a set of angular momentum operators $\{\hat{J}^2, \hat{J}_z, \hat{L}^2, \hat{S}^2\}$ which all commute with one another, and also commute with the Hamiltonian \hat{H} . Thus, they all have overlapping sets of eigenstates. In other words, there exists at least one eigenstate for each operator that is simultaneously an eigenstate for one or more of the other operators.

For the single $3d$ electron with $l = 2$ and $s = \frac{1}{2}$, j can take on values $j \in \{\frac{3}{2}, \frac{5}{2}\}$. Because there are two values, we call the state a doublet state, and the two states are labeled ${}^2D_{\frac{3}{2}}$ and ${}^2D_{\frac{5}{2}}$ according to 'term notation' ${}^{2S+1}L_j$ in which the value of $(2S + 1)$ is the spin degeneracy, L is the orbital angular momentum state, and the j subscript identifies the combined angular momentum state.

The energy levels associated with these two states are determined through a perturbation solution to the energy eigenvalue equation, also known as the time-independent Schrödinger equation. Without taking spin-orbit coupling into consideration, we can write down a zero-order approximation to the electron Hamiltonian

$$\hat{H}_0 = \frac{\hat{\mathbf{p}}^2}{2m} + V_n(\mathbf{r}) \quad (\text{A.13})$$

in which the first term on the right is the kinetic energy of the electron and $V_n(\mathbf{r})$ is the Coulomb potential of the nucleus. Note that $\hat{\mathbf{p}}$ is the generalized vector momentum operator and does not imply any particular coordinate system. In the case of the free ion, there are no external perturbation fields to consider, so the system is in a condition of spherical symmetry. Thus, we will find it useful to solve the eigenvalue equation in spherical coordinates. In this case, the Hamiltonian \hat{H}_0 can be written in radial and angular parts

$$\hat{H}_0 = \frac{\hat{p}_r^2}{2m} + \frac{\hat{L}^2}{2mr^2} + V_n(\mathbf{r}) \quad (\text{A.14})$$

$$= -\frac{\hbar^2}{2m} \left(\frac{1}{r} \frac{\partial}{\partial r} r \right)^2 + \frac{\hat{L}^2}{2mr^2} + V_n(\mathbf{r}) \quad (\text{A.15})$$

$$= -\frac{\hbar^2}{2m} \left(\frac{2}{r} \frac{\partial}{\partial r} + \frac{\partial^2}{\partial r^2} \right) + \frac{\hat{L}^2}{2mr^2} + V_n(\mathbf{r}). \quad (\text{A.16})$$

Substituting this into the Hamiltonian equation (A.13) above, and using that in the energy eigenvalue equation gives

$$\hat{H}_0|\varphi\rangle = -\frac{\hbar^2}{2mr^2} \left(\frac{1}{r} \frac{\partial}{\partial r} r \right)^2 |\varphi\rangle + \frac{\hat{L}^2}{r^2} |\varphi\rangle + V_n(\mathbf{r}) |\varphi\rangle. \quad (\text{A.17})$$

The well-known solutions to this equation can be found in virtually any elementary text on quantum mechanics as the solution to the 'hydrogenic' atom. The full solution to the zero-order energy eigenvalue equation

$$\hat{H}_0|\varphi_{nlm}(r, \theta, \phi)\rangle = E_n|\varphi_{nlm}(r, \theta, \phi)\rangle \quad (\text{A.18})$$

is found through the technique of separation of variables. Indeed, this is why the momentum operator was arranged as shown above into separate radial and angular functions. The solution eigenfunctions are the products of the various separable eigenfunctions², given by

$$|\varphi_{nlm}(r, \theta, \phi)\rangle = R_{nl}(r)Y_l^m(\theta, \phi) \quad (\text{A.19})$$

where $R_{nl}(r)$ is the radial function consisting of the associated Laguerre polynomials, and $Y_l^m(\theta, \phi)$ is the angular distribution expressed in spherical harmonics. For completeness, the radial solution is

²It is typical in quantum mechanics to specify the solution basis functions by $|\varphi_{nlm}\rangle$ (pure eigenfunctions of the Hamiltonian) and the general solution to the time-dependent Schrödinger equation by $|\psi\rangle$.

$$R_{nl}(r) = \left(\frac{2Z_{eff}}{a_0 n} \right)^{\frac{3}{2}} \sqrt{\frac{(n-l-1)!}{2n [(n+l)!]^{-3}}} \rho^l e^{-\rho/2} \sum_{i=0}^{n-l-1} \frac{(-1)^i [(n+l)!]^2 \rho^i}{i!(n-l-1-i)!(2l+1+i)!} \quad (\text{A.20})$$

in which a_0 is the Bohr radius, Z_{eff} is the effective nuclear charge, and $\rho = \frac{2Z_{eff}}{a_0 n}$ is a scaled radius. The angular solution is

$$Y_l^m(\theta, \phi) = \sqrt{\frac{2l+1}{4\pi} \frac{(l-m)!}{(l+m)!}} P_l^m(\cos \theta) \quad (\text{A.21})$$

where $P_l^m(\cos \theta)$ are the associated Legendre polynomials

$$P_l^m(\cos \theta) = \frac{(-1)^m}{2^l l!} (\sin^2 \theta)^{m/2} \left(\frac{\partial}{\partial \cos \theta} \right)^{m+l} (-\sin^2 \theta)^l. \quad (\text{A.22})$$

These eigenfunctions are all associated with the same set of energy eigenvalues

$$E_n = -\frac{z^2 \mathbb{R}}{n^2} \quad (\text{A.23})$$

where $\mathbb{R} = \frac{\hbar^2}{2\mu a_0^2}$ is the Rydberg constant and $a_0 = \frac{\hbar^2}{\mu e^2}$ is the Bohr radius.

Note that at this level of approximation the energy is solely a function of the principal quantum number n ; while the angular momentum quantum number l and its orientation, the so-called magnetic quantum number m_l affect the orbital shapes, only the radial potential from the effective nucleus affects the energy levels.

A.1.1 L S Coupling

As mentioned earlier, the relative orientation of the \mathbf{L} and \mathbf{S} vectors is expected to affect the energies of the various eigenstates of the single electron atom through spin-orbit coupling. The orbital angular momentum of the electron about the nucleus of

the atom results in an apparent magnetic field in the reference frame of the electron. Thus, the spin-induced magnetic moment of the electron will tend to the lower energy state in which it is more closely aligned to parallel to the induced magnetic field. The quantization of the orientation of spin states ($\pm\frac{1}{2}\hbar$) results in only two potential spin states which we refer to as parallel and anti-parallel to the induced magnetic field. This results in a splitting of the individual E_n derived earlier in eqn. (A.23). The magnitude of the energy splitting can be determined by adding a perturbation term \hat{H}'_{LS} to the zero-order Hamiltonian \hat{H}_0 , in which

$$\hat{H}'_{LS} = \frac{Z_{eff}e^2}{2m^2c^2r^3} \hat{L} \cdot \hat{S} \quad (\text{A.24})$$

This includes the relativistic 'Thomas factor' of $\frac{1}{2}$, and assumes that the nuclear Coulomb potential is completely radial, arising from a point charge of $Z_{eff}e$. Since we have changed the Hamiltonian, we should expect that the eigenfunctions and eigenvalues previously expected are probably no longer valid. However, we assume that the magnitude of energies included in the perturbation Hamiltonian \hat{H}'_{LS} are much smaller than those of \hat{H}_0 , and that the eigenfunctions of \hat{H}_0 approximate those of the total Hamiltonian \hat{H} . With that assumption, the new eigenvalue equation is

$$\hat{H}|\varphi_{nl}\rangle = (\hat{H}_0 + \hat{H}')|\varphi_{nl}\rangle \quad (\text{A.25})$$

$$= E_n|\varphi_{nl}\rangle + E'_{nl}|\varphi_{nl}\rangle \quad (\text{A.26})$$

from which we can work out the perturbation energy values E'_{nl} . Using eqn. (A.12) in the perturbation Hamiltonian (eqn. (A.24)) results in the perturbation eigenvalue equation

$$E'_{nl}|\varphi_{nl}\rangle = \hat{H}'_{LS}|\varphi_{nl}\rangle \quad (\text{A.27})$$

$$= \frac{Z_{eff}e^2}{4m^2c^2r^3} (\hat{J}^2 - \hat{L}^2 - \hat{S}^2)|\varphi_{nl}\rangle. \quad (\text{A.28})$$

By using the distributive property of operator mechanics, and equations (A.2), (A.5) and (A.9), we can generate the result

$$E'_{nl}|\varphi_{nl}\rangle = \frac{Z_{eff}e^2 \hbar^2}{2m^2c^2r^3} \frac{1}{2} [j(j+1) - l(l+1) - s(s+1)] |\varphi_{nl}\rangle. \quad (\text{A.29})$$

To determine the energy shift of the states, we calculate the expectation value of the energy operator (Hamiltonian) over all of the unperturbed eigenstates of the zero-order Hamiltonian.

$$\langle E'_{nl} \rangle = \langle nlm_j | \hat{H}'_{LS} | nlm_j \rangle \quad (\text{A.30})$$

$$= \langle nlm_j | \frac{Z_{eff}e^2 \hbar^2}{4m^2c^2r^3} [j(j+1) - l(l+1) - s(s+1)] | nlm_j \rangle \quad (\text{A.31})$$

$$= \frac{Z_{eff}e^2 \hbar^2}{4m^2c^2} \langle nlm_j | \frac{1}{r^3} | nlm_j \rangle [j(j+1) - l(l+1) - s(s+1)] \quad (\text{A.32})$$

$$= \frac{Z_{eff}e^2 \hbar^2}{4m^2c^2} \frac{Z_{eff}^3}{a_0^3 n^3 l(l+s)(l+1)} [j(j+1) - l(l+1) - s(s+1)] \quad (\text{A.33})$$

The solution to the integral above (*i.e.* $\frac{1}{r^3}$) was obtained by radially integrating the product of $1/r^3$ and the radial wave equation. By substituting in the Bohr radius and rearranging, we can rewrite the perturbed energy eigenvalues as a function of the unperturbed energy eigenvalues E_n (eqn (A.23)),

$$\langle E_{nl}' \rangle = E_n^2 \frac{n}{mc^2 l(l + \frac{1}{2})(l+1)} [j(j+1) - l(l+1) - s(s+1)]. \quad (\text{A.34})$$

Since we are dealing with an electron which has spin $s = \frac{1}{2}$ and we know that j can take on values from $l+s$ to $l-s$ in unit increments, then we can reduce $j(j+1) - l(l+1) - s(s+1)$ to l for the case of $j = l + \frac{1}{2}$, and $-(l+1)$ for the case of $j = l - \frac{1}{2}$. Thus, the perturbation energies resulting from the spin-orbit interaction are

$$E_{nl}'^+ = E_n^2 \frac{n}{mc^2 (l + \frac{1}{2})(l+1)} \quad (\text{A.35})$$

$$= E_n^2 \frac{2n}{mc^2 (2l+1)(l+1)} \quad (\text{A.36})$$

and

$$E'_{nl} = E_n^2 \frac{n}{mc^2 l(l + \frac{1}{2})} \quad (\text{A.37})$$

$$= E_n^2 \frac{2n}{mc^2 l(2l + 1)}. \quad (\text{A.38})$$

The perturbation energy is of the order $\frac{E_n^2}{mc^2}$. Since for the hydrogen atom E_n is of order 10 eV, but for an electron the rest mass is 0.5 MeV, we find that $E'_{nl} \ll E_n$, justifying the perturbation approach.

A.1.2 Relativistic Corrections

Rigorous estimation of the atomic levels of ions also requires that the relativistic correction for electron mass be considered. Since these corrections are of the same order as the corrections for LS coupling, perturbation solutions from the zero-order energy eigenvalues will also be sought. We have previously written the zero-order Hamiltonian function as a function of the classical momentum \mathbf{p} . However, in making the relativistic correction, we must replace the classical kinetic energy of the electron with the relativistic energy which includes the rest-mass term, or

$$\frac{p^2}{2m} \rightarrow \sqrt{p^2 c^2 + m^2 c^4}. \quad (\text{A.39})$$

Since we are interested only in the kinetic energy of the electron, we subtract the rest mass of the electron from the total energy term and apply the binomial series expansion

$$T = (m^2c^4 + p^2c^2)^{\frac{1}{2}} - mc^2 \quad (\text{A.40})$$

$$= mc^2 \left(1 + \frac{p^2}{m^2c^2}\right)^{\frac{1}{2}} - mc^2 \quad (\text{A.41})$$

$$= mc^2 \left[\left(1 + \frac{1}{2} \frac{p^2}{m^2c^2} - \frac{1}{8} \left(\frac{p^2}{m^2c^2}\right)^2 + \dots\right) - 1 \right] \quad (\text{A.42})$$

$$\approx \frac{1}{2} \frac{p^2}{m} - \frac{1}{8} \left(\frac{p^4}{m^3c^2}\right) \quad (\text{A.43})$$

The first term in the brackets on the right hand side is the familiar classical kinetic energy term, while the second is the first-order relativistic energy correction term. The perturbation Hamiltonian then becomes

$$\hat{H}'_r = -\frac{\hat{p}^4}{8m^3c^2} \quad (\text{A.44})$$

which gives the energy correction term

$$\langle E'_r \rangle = -\frac{1}{8m^3c^2} \langle nl | \hat{p}^4 | nl \rangle \quad (\text{A.45})$$

$$= -\frac{1}{8m^3c^2} \langle \varphi_{nl} | \hat{p}^2 \hat{p}^2 | \varphi_{nl} \rangle \quad (\text{A.46})$$

$$= -\frac{1}{8m^3c^2} \langle p^2 \varphi_{nl} | p^2 \varphi_{nl} \rangle. \quad (\text{A.47})$$

With the integral in this form, since $\hat{H}|\varphi_{nl}\rangle = \left(\frac{\hat{p}^2}{2m} - V(r)\right)|\varphi_{nl}\rangle = E_n|\varphi_{nl}\rangle$ we can rewrite $\langle p^2 \varphi_{nl} | p^2 \varphi_{nl} \rangle$ in integral form as

$$\langle p^2 \varphi_{nl} | p^2 \varphi_{nl} \rangle = \int (2m(E_n - V(r))\varphi_{nl})^2 d^3r \quad (\text{A.48})$$

$$= 2m \int_0^\infty (E_n - V(r))^2 R_{nl}(r) r^2 dr \quad (\text{A.49})$$

where the purely radial potential function allows us to limit the integration to the radial part of the wave function. The result of these integrals are inserted into (A.45) to obtain

$$E'_r = -\frac{E_n^2}{2mc^2} \left(\frac{8n}{2l+1} - 3 \right). \quad (\text{A.50})$$

This is clearly of the same order as the spin-orbit coupling perturbation, validating this approach. By combining the zero-order energy eigenvalues with the spin-orbit perturbation results (A.35) and (A.37) and the results of (A.50) we obtain the first order solution to the energy levels of a single electron in a hydrogenic atom,

$$E_{nlj} = E_n + E'_{LS} + E'_r \quad (\text{A.51})$$

$$= E_n - \frac{E_n^2}{2mc^2} \left(\frac{8n}{2j+1} - 3 \right). \quad (\text{A.52})$$

A.1.3 Two 3d electrons

With an understanding of a single 3d electron in the Mn^{5+} ion, we can proceed to extend this to two electrons. The full term designation for the Mn^{5+} ion is $1s^2 2s^2 2p^6 3s^2 3p^6 3d^2$. The complete filling of the lower n and l orbitals allows us to abbreviate this $[\text{Ar}] 3d^2$ which implies two 3d electrons about a filled argon shell.

Since $n = 3$, the orbital angular momentum l for each of the valence electrons can take on values of $l_i \in \{0, 1, 2\}$ so two electrons can have a total angular momentum ranging from $l_{tot} \in \{|l_1 - l_2|, \dots, |l_1 + l_2|\}$ which for our purposes becomes $l_{tot} \in \{0, 1, 2, 3, 4\}$. Likewise, addition of the spin angular momentum vectors of the two electrons results in a total spin of $s_{tot} \in \{0, 1\}$. As before, we combine the spin and orbital angular momenta to produce the general angular momentum vector j_{tot} with values $j_{tot} \in \{|l_{tot} - s_{tot}|, \dots, |l_{tot} + s_{tot}|\}$ or $j_{tot} \in \{0, 1, 2, 3, 4, 5\}$. Likewise, we know that there are $(2l_1 + 1)(2l_2 + 1) = 25$ independent states which are solutions to the energy eigenvector equation. Putting aside wavefront symmetry arguments for the moment, review of the various configurations of these s_{tot} , l_{tot} and j_{tot} terms reveals that the possible states of this two-electron ion are all either singlet or triplet states.

The potential singlet states are $\{^1S_0, ^1P_1, ^1D_2, ^1F_3, ^1G_4\}$ whereas the triplet states are $\{^3S_1, ^3P_{2,1,0}, ^3D_{3,2,1}, ^3F_{4,3,2}, ^3G_{5,4,3}\}$.

To determine which of these are actually viable configurations, we must consider the Pauli exclusion principle which precludes two electrons from having identical quantum numbers. Another way of stating this is that the allowed states for two electrons in an ion must be antisymmetric under the exchange operation. If we consider the coupled representation in which the radial wave function R is a linear combination of the radial wavefunctions of the individual electrons (R_1 and R_2), then the coupled representation can be either symmetric in which

$$R = R_1(1)R_2(2) + R_1(2)R_2(1), \quad (\text{A.53})$$

or antisymmetric in which

$$R = R_1(1)R_2(2) - R_1(2)R_2(1). \quad (\text{A.54})$$

Of these terms, only the ones in which l_{tot} is even and s_{tot} is even, or in which l_{tot} is odd and s_{tot} is odd have proper wavefunction symmetry such that the exchange integral is non-zero. These occur for the $s_{tot} = 0, l_{tot} \in \{0, 2, 4\}$ (i.e. $^1S, ^1D$, and 1G terms) and the $s_{tot} = 1, l_{tot} \in \{1, 3\}$ (i.e. $^3P_{2,1,0}$, and $^3F_{4,3,2}$ terms).

To identify the ground state among these, we turn to Hund's Rules. These are

1. The lowest energy term is the one with the maximum allowed multiplicity.
2. Among these, the lowest energy term is the one with the largest combined orbital angular momentum.
3. In this term, if the valence shell is less than half filled, the lowest energy multiplet is the one with the lowest value of total angular momentum. Otherwise, the lowest energy multiplet is the one with the highest value of total angular momentum.

For our situation, rule (1) requires that a triplet state be the ground state. Of the 3P and 3F states, the latter has the largest combined orbital angular momentum, so rule (2) indicates that the ground state will be among these triplet states. Finally, the valence shell has two of ten places filled, the lowest value of j is 2, so the ground state is the 3F_2 state.

Appendix B

RAYLEIGH BEACONS

Rayleigh beacons have been used with some success in the creation of guide stars for adaptive optics. They have been developed and used by the military for over two decades at various imaging sites [33]. In addition, Rayleigh beacons have been implemented with some success by astronomers as well [105].

Rayleigh beacons have several distinct advantages over sodium beacons. First and foremost is the ability to use the beacon at any wavelength and over any spectral bandwidth. Relaxation of the requirement to hit a particular atomic resonance line opens the field of potential lasers remarkably, including many well-developed, mature, high-power lasers of varying designs.

This is not to say that the laser wavelength is irrelevant in a Rayleigh beacon. The magnitude of Rayleigh scattering (in power) is proportional to λ^{-4} , and thus it is generally beneficial to go to shorter wavelengths in order to increase the scattered power. This is true down to the wavelength where scattering becomes so large that the transmission of the atmosphere severely limits the power available at a particular height. There the scattered return from the Rayleigh beacon begins to drop off rapidly. In addition, ozone absorbs heavily at certain wavelengths limiting the transmission even further. Finally, to avoid potential hazards of startling or dazzling pilots and to minimize the aesthetic impact of the guide star beacon on the natural beauty of the night sky from the mountaintop environment, it is desirable to consider a beam which is invisible to the naked eye.

The main reason that Rayleigh beacons have not been developed further is that they are significantly limited in their effectiveness by focal anisoplanatism, the so-called 'cone effect'. Rayleigh beacons are dependent upon the existence of significant

numbers of scattering molecules (N_2) at the height of interest. Since the number of scattering sites drops off rapidly with increasing height, the Rayleigh guide star rapidly gets dimmer at higher altitudes, which limits the accuracy of the guide star position determination on the CCD. Thus, it is difficult to get a Rayleigh beacon to work well at scattering altitudes of over 30 km. However, light from a low-altitude beacon traverses a path that differs significantly from that of light from the science objects at infinity. The problem is exacerbated for turbulent atmospheric layers that are high above the telescope. In these cases, the light from the Rayleigh beacon may transit an entirely different patch of the turbulent layer from the light from the science object. Obviously in this case, the ability of the AO system to sense the effects of the turbulent layer, much less correct for it, is severely hampered. The problem is magnified even further when one considers that the areas in which the cone effect is the worst is at locations toward the edge of the pupil where the light collecting power is greatest. Thus, in the trend toward development of larger and larger telescopes, the Rayleigh beacon becomes less and less useful in AO systems.

A second, but less important reason for the trend away from Rayleigh beacons is that they must be gated in order to work. Whereas the height of a sodium beacon is limited because of the isolation of sodium atoms in the mesosphere, the height of the Rayleigh backscatter is only limited by the length of the laser pulse, and the integration of the shutter of the camera viewing the beacon. Thus, the apparent length of the Rayleigh beacon is the convolution of the laser pulse length and the camera integration time. By increasing one or both of these, the number of atoms available to scatter the light increases, increasing the brightness of the returned guide star. However, the length of the beam also increases, and when viewed from off-axis the laser spot appears elongated. While the tangential wavefront error estimation improves (from the improvement afforded by a brighter guide star), the radial wavefront error estimation gets worse.

The problem of the cone effect can be effectively resolved by using multiple

Rayleigh beacons. Since Rayleigh beacons have been shown to be quite effective for smaller apertures, then it is easy to see how breaking up a larger aperture into a set of smaller ones, each with its own Rayleigh beacon, can result in marked improvements. In addition to the amelioration of the cone effect, there are additional advantages to be reaped as well. Whereas in previous systems a single beam was used and the return was collected by sub-apertures, we can now effectively use the reverse of the system in which each sub-aperture is a projector, and the entire aperture is used to collect the light. From a physics standpoint, this is not much of an advantage. Since we have the same number of sub-apertures in either system, and since Rayleigh scattering is not subject to saturation, then the same advantage could be gained by increasing the power of the laser by the number of sub-apertures. In doing so, the scattered brightness increases by the number of lasers added together, offsetting the loss by using smaller sub-apertures. However, from an engineering standpoint there are difficulties with linearly scaling the power of a laser; thermal effects and medium saturation tend to limit the laser power at some point. Thus it is much easier to realize a system with multiple lasers.

The main potential advantage to using multiple Rayleigh beacons exists in the potential it affords for performing atmospheric tomography. With a single guide star, especially CW sodium guide stars, there is no simple way of determining the height of the turbulent layer. We are thus limited to sensing the wavefront in a single plane (usually the pupil plane) and correcting it in a conjugate plane. However, by tracking multiple guide stars through all altitudes using the entire aperture of the telescope, we can determine the height at which the turbulent layer scattered the (known) emitted array of beams. Furthermore, by tracking the array of guide stars at various heights, we can also determine when multiple turbulent layers exist, and perform the corrections at their conjugate surfaces.

In deciding which types of lasers might be optimal (or even suitable) candidates for a Rayleigh beacon, a simple model of atmospheric scattering is quite useful. In

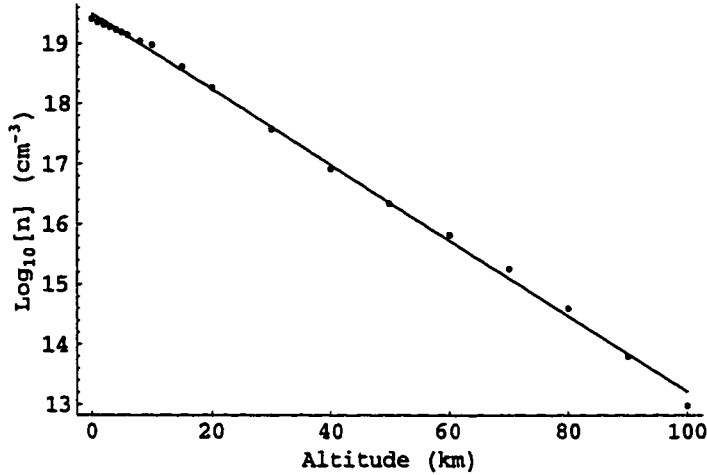


FIGURE B.1. Comparison of atmospheric molecular number density tabulated in [2] with modeled exponential number density.

developing this model, we had to consider the effects from atmospheric transmission and scattering dependent on both altitude and wavelength. First, the relative density of the atmosphere must be considered. We performed a linear fit to the profile of the \log_{10} molecular number density tabulated by Allen [2] at various altitudes. The data, and the modeled distribution are shown in Figure B.1.

The spectral scattering coefficient per molecule was derived to be

$$s(\lambda) = 1.0410^5(n(\lambda) - 1)^2/\lambda^4 \quad (\text{B.1})$$

where $n(\lambda)$, the index of refraction of air at sea level is given by

$$n(\lambda) = 1 + 2.87610^{-4} + 1.62910^{-6}\lambda^{-2} + .13610^{-8}\lambda^{-4}. \quad (\text{B.2})$$

In addition, because of the strong absorption of ozone in the UV, a simple model of ozone absorption was also incorporated. The model was derived empirically to fit the two main absorption bands of concern in ozone listed in [2]. The function is

$$\alpha_{\text{ozone}}(\lambda) = .04254e^{-160(\lambda-0.6)^2} + 97.3587e^{-1300(\lambda-0.255)^2}. \quad (\text{B.3})$$

The ozone spectral absorption values in Allen, and the empirical model used to approximate it are seen in Figure B.2. The ozone was assumed to be concentrated in a

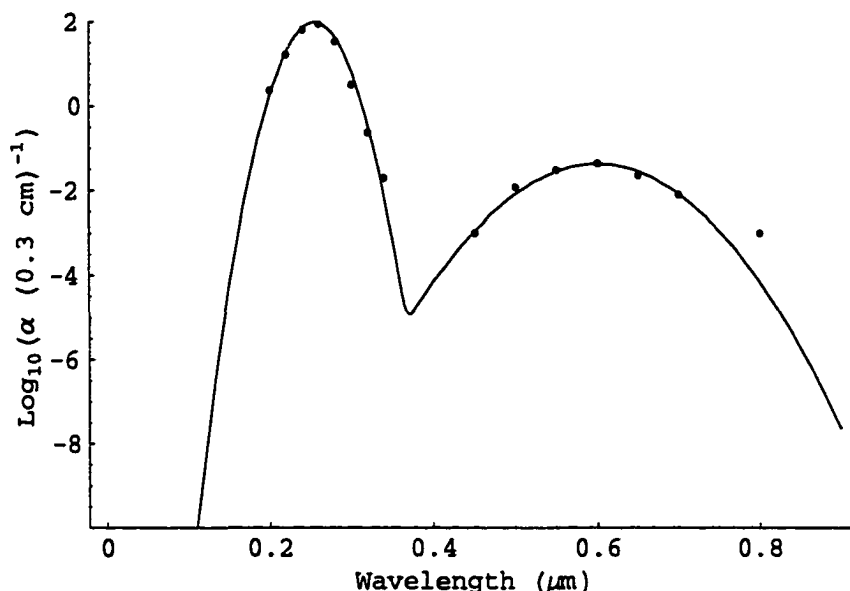


FIGURE B.2. Comparison of spectral absorption values of ozone listed in [2] with empirical function used in the model.

band with a Gaussian density profile in height, centered on 20 km altitude.

Assuming no particulate or aerosol contributions to scattering, we can use this model to predict the best possible atmospheric transmission to various altitudes as a function of wavelength. This is plotted in Figure B.3

Because of the reduction of transmission at the short-wavelength end of the spectrum, and the reduction in Rayleigh scattering at the long-wavelength end of the spectrum, we anticipate that there must be a maximum operating point to maximize the photon return from a Rayleigh beacon. This is, indeed, the case, as we see in Figure B.4 We see that the maximum photon return is obtained right at the blue edge of the visible band. Operating in this range is quite favorable for a number of reasons. First, there are several candidate high-power lasers which can be used at these wavelengths including XeCl excimer lasers (351 nm) and frequency-tripled Nd:YAG lasers(355 nm). Situating the telescope at higher altitudes (generally the case for research telescopes) has the effect of reducing the total amount of Rayleigh

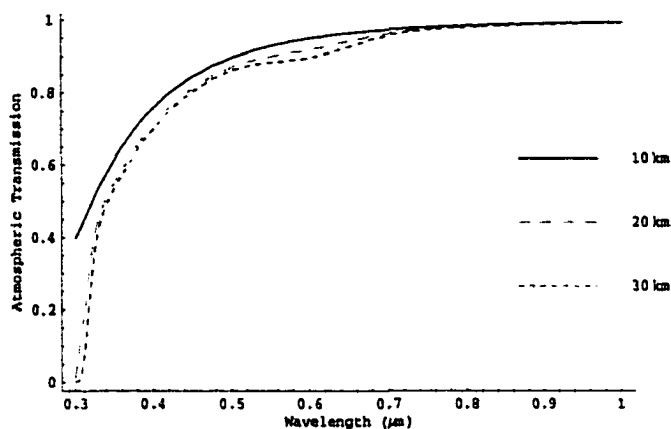


FIGURE B.3. Spectral transmission of the atmosphere from sea level to the indicated heights. The model incorporates losses from Rayleigh scattering and ozone absorption. Note the effects of ozone absorption around $0.6 \mu m$ for the 20 km and 30 km curves. The 10 km curve does not show the effect because that is below any significant ozone absorption.

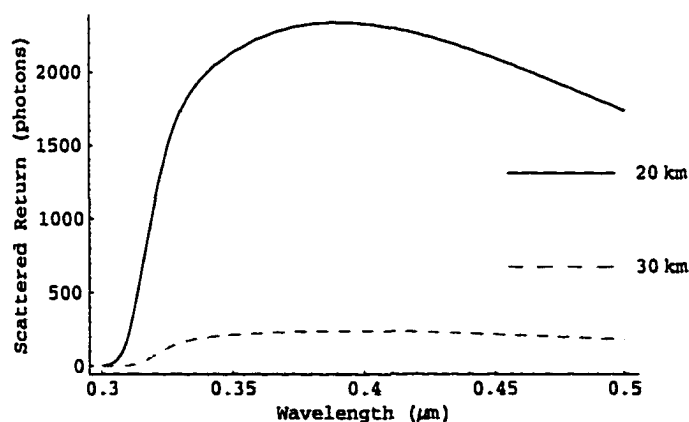


FIGURE B.4. Spectral return (photons) from 20 km and 30 km scattering heights. This is for pulses of 0.165 Joules, pulse lengths of 1.25 km, and collecting subapertures of just under $0.02 m^2$. It assumes that the telescope is at sea level, and perfect optics collection efficiency and perfect detector quantum efficiency.

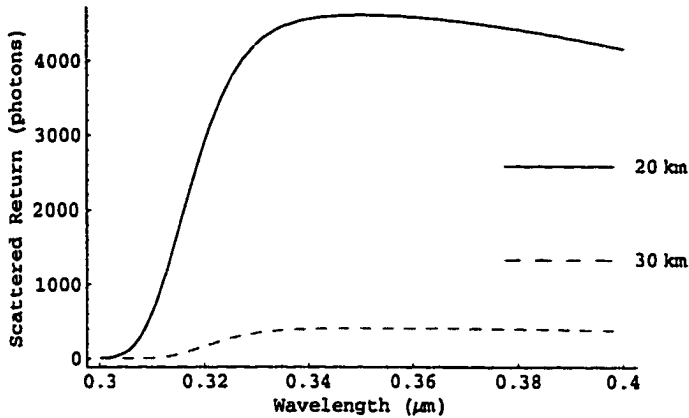


FIGURE B.5. Spectral return from 20 km and 30 km scattering heights (msl), assuming the telescope and laser projector are situated 3 km above sea level. All other conditions are the same as those used to produce Figure B.4.

scattering, significantly improving atmospheric transmission at the short end of the spectrum. The result is that the optimal operational wavelength is shifted to higher energies. In fact, for a telescope system at 3 km, the optimal operating wavelength (for maximum Rayleigh backscatter) is $0.35 \mu m$, as shown in Figure B.5. Finally, we can see the effects of tracking a pulse of wavelength 355 nm through various heights above the telescope. This is seen in Figure B.6. These lines assume a 1.0 Joule pulse, an integration period allowing a 1.0 km and a 0.5 km pulse to be observed, collected by a 1.0 m^2 subaperture.

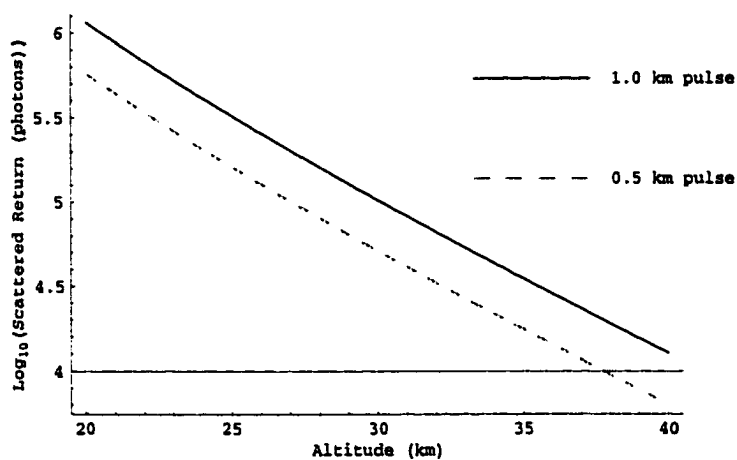


FIGURE B.6. The return expected from pulses of specified length as a function of height (MSL). This is for 1.0 Joule pulses of light at 355 nm, collected by a 1.0 m² subaperture assuming perfect collection efficiency and perfect detection efficiency.

REFERENCES

- [1] Govind P. Agrawal. *Nonlinear Fiber Optics*. Optics and Photonics. Academic Press, San Diego, second edition, 1995.
- [2] C. W. Allen. *Astrophysical Quantities*. The Athlone Press, 4 Gower St., London, 1973.
- [3] L. Allen and J. H. Eberly. *Optical Resonance and Two-Level Atoms*. Dover Publications, Inc., New York, 1987.
- [4] K. Avicola, J. M. Brase, J. R. Morris, H. D. Bissinger, J. M. Duff, H. W. Friedman, D. T. Gavel, C. E. Max, S. S. Olivier, R. W. Presta, D. A. Rapp, J. T. Salmon, and K. E. Waltjen. Sodium-layer laser-guide-star experimental results. *Journal of the Optical Society of America - A*, 11(2):825–831, February 1994.
- [5] Kenneth Avicola, James Brase, James Morris, Horst Bissinger, Herbert Friedman, Donald Gavel, Rodney Kiefer, Claire Max, Scot Olivier, David Rapp, Thad Salmon, David Smauley, and Kenneth Waltjen. Sodium laser guide star system at lawrence livermore national laboratory: system description and experimental results. In *Adaptive Optics in Astronomy*, volume 2201, pages 326–341. SPIE - The International Society for Optical Engineering, 1994.
- [6] H. J. Baker, A. Chesworth, D. Lelaez Millas, and D. R. Hall. Power scaling of thin nd:glass and nd:yag slab lasers, face-pumped by laser diodes. In *OSA TOPS*, volume 19, pages 407–410. The Optical Society of America, 1998.
- [7] Norman P. Barnes, Keith E. Murray, Elka B. Ertur, Brian M. Walsh, and Ralph L. Hutcheson. Compositionally tuned solid state lasers. In *OSA Trends in Optics and Photonics on Advanced Solid-State Lasers*, volume 1 of *Topical Meeting*, pages 522–5. Optical Society of America, 1996.
- [8] T. T. Basiev, 2000. Private communication through Dr. Robert Eckardt.
- [9] T. T. Basiev and S. V. Mirov. *Room Temperature Tunable Color Center Lasers*. Harwood Academic Publishers, Poststrasse 22, 7000 Chur, Switzerland, 1994.
- [10] T. T. Basiev, A. A. Sobol, P. G. Zverev, Yu. K. Voron'ko, V. V. Osiko, and R. C. Powell. Comparative raman spectroscopy study of crystals for raman lasers. *OSA TOPS Advanced Solid State Lasers*, 19:546–549, 1998.

- [11] T. T. Basiev, A. A. Sobol, Petr G. Zverev, Vyachislav V. Osiko, and Richard C. Powell. Comparative spontaneous raman spectroscopy of crystals for raman lasers. *Applied Optics*, 38(3):594–598, 20 January 1999.
- [12] N. Bloembergen. The stimulated raman effect. *American Journal of Physics*, 35(11):989–1023, November 1967.
- [13] B. Brandl, B. J. Sams, F. Bertoldi, A. Eckart, R. Genzel, and S. Drapatz. Adaptive optics near-infrared imaging of r136 in 30 doradus: the stellar population of a nearby starburst. *The Astrophysical Journal*, 466:254–273, 1996.
- [14] B. Buijsse, J. Schmidt, I. Y. Chan, and David J. Singel. Electron spin-echo-detected excitation spectroscopy of manganese-doped $\text{ba}_3(\text{vo}_4)_2$: Identification of tetrahedral mn^{5+} as the active laser center. *Physical Review B*, 51(10):6215–6220, March 1995.
- [15] B&W Tek, Inc. <http://www.bWtek.com/>, 2001. Web page maintained by B&W Tek.
- [16] B&W Tek, Inc. Private communication, 2001.
- [17] J. A. Capobianco, G. Cormier, R. Moncorge, H. Manaa, and M. Bettinelli. Gain measurements of Mn^{5+} ($3d^2$) doped $\text{Sr}_5(\text{PO}_4)_3\text{Cl}$ and $\text{Ca}_2\text{PO}_4\text{Cl}$. *Applied Physics Letters*, 60(2):163–165, 13 January 1992.
- [18] E. C. Cheung, J. G. Ho, H. Injeyan, M. M. Valley, J. G. Berg, R. L. Byer, and Y. Huang. A solid state raman laser for sodium d2 line resonant excitation. In *OSA Adaptive Optics*, 1996.
- [19] L. M. Close, F. Roddier, J. L. Hora, J. E. Graves, M. Northcott, C. Roddier, W. F. Hoffman, A. Dayal, G. G. Fazio, and L. K. Deutsch. Adaptive optics infrared imaging-polarimetry and optical hst imaging of hubble’s variable nebula (r mon/ngc 2261): a close look at a very young active herbig ae/be star. *The Astrophysical Journal*, 489:210–221, 1 November 1997.
- [20] S. C. Collins, T. D. Wilkerson, V. B. Wickwar, D. Rees, J. C. Walling, and D. F. Heller. The alexandrite ring laser: A spectrally narrow lidar light source for atmospheric fluorescence and absorption observations. In *Advances in Atmospheric Remote Sensing with Lidar. Selected Papers of the 18th International Laser Radar Conference (ILRC)*, pages 577–580. Springer-Verlag, 22-26 July 1996.
- [21] B. Comasky, G. Albrecht, R. Beach, S. Velsko, S. Sutton, S. Mitchell, C. Petty, K. Jancaitis, W. Bennett, B. Freitas, and R. Solarz. A one kilowatt average power diode pumped nd:yag folded zigzag slab laser. In *Diode Pumping*

of Average-Power Solid State Lasers, volume 1865, pages 17–27. SPIE - The International Society for Optical Engineering, 1993.

- [22] J. C. Dainty. Optical effects of atmospheric turbulence. In N. Ageorges and C. Dainty, editors, *Laser Guide Star Adaptive Optics for Astronomy*, pages 1–21. Kluwer Academic Publishers, Netherlands, 2000.
- [23] Christopher C. Davis. *Lasers and Electro-Optics*. Cambridge University Press, The Pitt Building, Trumpington St., Cambridge CB2 1RP, London, U.K., 1996.
- [24] S. Desgreniers, S. Jandl, and C. Carlone. Temperature dependence of the raman active phonons in CaWO_4 , SrWO_4 and BaWO_4 . *Journal of the Physical Chemistry of Solids*, 45(11/12):1105–1109, 1984.
- [25] W. W. Duley. Gas lasers. In Robert A. Meyers, editor, *Encyclopedia of Lasers and Optical Technology*, pages 139–148. Academic Press, Inc., San Diego, 1991.
- [26] Gisela Eckhardt. Selection of raman laser materials. *IEEE Journal of Quantum Electronics*, QE-2(1):1–8, January 1966.
- [27] J. C. Elliott. *Structure and Chemistry of the Apatites and Other Calcium Orthophosphates*. Elsevier, Turner Street, London E1 2AD, U. K., 1994.
- [28] R. Foy and A. Labeyrie. Feasibility of adaptive telescope with laser probe. *Astronomy and Astrophysics*, 152(2):L29–31, November 1985.
- [29] Herbert Friedman. private communication at ESO workshop, June 1997.
- [30] Herbert Friedman, Gaylen Erbert, Thomas Kuklo, Thaddeus Salmon, David Smauley, Gary Thompson, Jody Malik, Nan Wong, Keith Kanz, and Kurt Neeb. Sodium beacon laser system for the lick observatory. In *Adaptive Optical Systems and Applications*, volume 2534, pages 150–159. SPIE, 1995.
- [31] Institute fuer Angewandte Festkoerperphysik. <http://www.iaf.fgh.de/diamond/diamond.thermics.htm>, 2001. Web page maintained by IAF.
- [32] Robert Q. Fugate. Review of laser technology and status. In *Adaptive Optics*, volume 13 of *Technical Digest Series*, pages 90–92. Optical Society of America, July 1996.
- [33] Robert Q. Fugate and Walter J. Wild. Untwinkling the stars. *Sky and Telescope*, pages 24–31, May 1994.

- [34] Donald T. Gavel and Herbert W. Friedman. Measurements of the lick observatory sodium laser guide star. In Domenico Bonaccini and Robert K. Tyson, editors, *Adaptive Optical System Technologies*, volume 3353, pages 254–259. SPIE, 23-26 March 1998.
- [35] Jian Ge, Roger Angel, David Sandler, Chris Shelton, Don McCarthy, and Jim Burge. Adaptive optics spectroscopy: Preliminary theoretical results. In R. Tyson and R. Q. Fugate, editors, *Adaptive Optics and Applications*, volume 3126, pages 343–354. SPIE, JULY 1997.
- [36] Jian Ge, B. P. Jacobsen, J. R. P. Angel, P. C. McGuire, T. Roberts, B. McLeod, and M. Lloyd-Hart. Simultaneous measurements of sodium column density and laser guide star brightness. In *1998 SPIE conference Proceedings 3353 on Adaptive Optics System Technologies*, volume 1434. SPIE - The International Society for Optical Engineering, 1998.
- [37] J. Gieseke, G. Schmidt, C. Schnitzler, T. Mans, R. Wester, K. M. Du, P. Loosen, and R. Poprawe. Highly efficient diode end pumped nd:yag slab laser. In *Solid State Lasers IX*, volume 3929, pages 98–107. SPIE - The International Society for Optical Engineering, 2000.
- [38] Y. Y. Gu, J. Qian, G. C. Papen, G. R. Swenson, and P. J. Espy. Concurrent observations of auroral activity and a large sporadic sodium layer event during anlc-93. *Geophysical Research Letters*, 22(20):2805–2808, October 15 1995.
- [39] W. Hackenberg, H.-C. Holstenberg, A. Quirrenbach, and N. Wilnhammer. The alfa laser-guidestar system - an overview. In *ESO Workshop on Laser Technology for Laser Guidestar Adaptive Optics Astronomy*, 1997.
- [40] Morton Hamermesh. *Group Theory and its Application to Physical Problems*. Dover Publications, Inc., 31 E. Second St., Mineola, New York, 11501, USA, 1962.
- [41] W. Happer, G. MacDonald, C. E. Max, and F. Dyson. Atmospheric-turbulence compensation by resonant optical backscattering from the sodium layer in the upper atmosphere. *Journal of the Optical Society of America A*, 11:263–276, 1994.
- [42] Eugene Hecht. *Optics*. Addison-Wesley, Reading, Massachusetts, third edition, 1998.
- [43] John N. Howard. Optics. In Herbert L. Anderson, editor, *Physics Vade Mecum*, page 253. American Institute of Physics, 335 E. 45th St., New York, New York, 10017, 1981.

- [44] Frank P. Incropera and David P. DeWitt. *Introduction to Heat Transfer*. John Wiley and Sons, New York, second edition, 1990.
- [45] Bruce P. Jacobsen, Ty Martinez, J. Roger P. Angel, Michael Lloyd-Hart, Steve Benda, Dave Middleton, Herb Friedman, and Gaylen Erbert. Field evaluation of two new continuous-wave dye laser systems optimized for sodium beacon excitation. In *Proceedings of the SPIE*, volume 2201, pages 342–351, 1994.
- [46] Thomas H. Jeys. Development of a mesospheric sodium laser beacon for atmospheric adaptive optics. *The Lincoln Laboratory Journal*, 4(2):133–150, 1991.
- [47] P. D. Johnson, J. S. Prener, and J. D. Kingsley. Apatite: Origin of blue color. *Science*, 141(1A):1179–1180, September 1963.
- [48] T. F. Johnston, Jr., R. H. Grady, and W. Proffitt. Powerful single-frequency ring dye laser spanning the visible spectrum. *Applied Optics*, 21(3):2307–2316, July 1982.
- [49] Alexander A. Kaminskii. *Laser Crystals*. Springer-Verlag, Berlin, Heidelberg, 1981.
- [50] Alexander A. Kaminskii, Hans J. Eichler, Ken ichi Ueda, Nikolai V. Klassen, Boris S. Redkin, Ludmila E. Li, Julian Findeisen, Daniel Jacque, Jose Garcia-Sole, Joaquin Hernandez, and Rolindes Balda. Properties of Nd³⁺-doped and undoped tetragonal PbWO₄, NaY(WO₄), CaWO₄, and undoped monoclinic ZnWO₄ and CdWO₄ as laser-active and stimulated raman scattering-active crystals. *Applied Optics*, 38(21):4533–4547, July 1999.
- [51] Nam Seong Kim, Mahendra Prabhu, Cheng Li, Jie Song, and Ken ichi Ueda. 1239/1484 nm cascaded phosphosilicate raman fiber laser with cw output power of 1.36 w at 1484 nm pumped by cw yb-doped double-clad fiber laser at 1064 nm and spectral continuum generation. *Optics Communications*, 176:219–222, 15 March 2000.
- [52] Nam Seong Kim, Mahendra Prabhu, Cheng Li, Jie Song, and Ken ichi Ueda. Output characteristics of p-doped raman fiber laser at 1484 nm with 2.11 w maximum output power pumped by cw 1064 nm yb-doped double-clad fiber laser. *Japanese Journal of Applied Physics*, 39(11):6264–6267, November 2000.
- [53] Walter Koechner. *Solid State Laser Engineering*. Springer, Berlin, Heidelberg, fourth edition, 1996.
- [54] T. Komukai, K. Tamura, and M. Nakazawa. An efficient 0.04-nm apodized fiber bragg grating and its application to narrow-band spectral filtering. *IEEE Photonics Technology Letters*, 9(7):934–936, July 1997.

- [55] Lucent Bell Labs. <http://www.lucent.com/press/0597/970528.bla.html>, 1997. Web page maintained by Lucent, Inc.
- [56] Herbert Lachwa and Dirk Reinen. Color and electronic structure of manganese(v) and manganese(vi) in tetrahedral oxo coordination. a spectroscopic investigation. *Inorganic Chemistry*, 28:1044–1053, 1989.
- [57] O. Lai, D. Rouan, F. Rigaut, R. Aresenault, and E. Gendron. Adaptive optics observations of ultra-luminous infrared galaxies: I, j, h, k images of mkn231. *Astronomy and Astrophysics*, 334:783–788, 1998.
- [58] Richard L. Liboff. *Introductory Quantum Mechanics*. Addison Wesley Longman, Inc., Reading, Massachusetts, 1996.
- [59] M. Lloyd-Hart, R. Dekany, D. Sandler, D. Wittman, R. Angel, and D. McCarthy. Progress in diffraction-limited imaging at the multiple mirror telescope with adaptive optics. *Journal of the Optical Society of America A*, 11(2):846–857, February 1994.
- [60] M. Le Louarn. Sky coverage with laser guide star systems on 8 meter telescopes. In N. Ageorges and C. Dainty, editors, *Laser Guide Star Adaptive Optics for Astronomy*, pages 169–183. Kluwer Academic Publishers, Netherlands, 2000.
- [61] Hacene Manaa, Yannick Guyot, Ferhat Deghoul, Richard Moncorge, and Larry D. Merkle. Excited state absorption in $\text{Mn}^{5+}:\text{Sr}_5(\text{VO}_4)_3\text{F}$. *Chemical Physics Letters*, 238:333–337, 2 June 1995.
- [62] C. E. Max, S. S. Olivier, H. W. Friedman, J. An, K. Avicola, B. V. Beeman, H. D. Bissinger, J. M. Brase, G. V. Erbert, D. T. Gavel, K. Kanz, M. C. Liu, B. Macintosh, K. P. Neeb, J. Patience, and K. E. Waltjen. Image improvement from a sodium-layer laser guide star adaptive optics system. *Science*, 277:1649–1652, 12 September 1997.
- [63] Richard C. Mayer and Raymond H. Hsu. Modelling the gain of a diode-pumped solid state laser. *Mathematical Computations Modelling*, 11:308–312, 1988.
- [64] D. McConnell. *Apatite: Its Crystal Chemistry, Mineralogy, Utilization, and Geologic and Biologic Occurrences*. Springer-Verlag, New York, 1973.
- [65] L. S. Meng, K. S. Repasky, P. A. Roos, and J. L. Carlsten. Widely tunable continuous-wave raman laser in diatomic hydrogen pumped by an external-cavity diode laser. *Optics Letters*, 25(7):472–474, 1 April 2000.
- [66] L. D. Merkle, B. H. T. Chai, and Y. Guyot. Spectroscopy of the laser ion Mn^{5+} in $\text{Sr}_5(\text{VO}_4)_3\text{F}$. In *New Materials for Advanced Solid State Lasers*, volume 329, pages 239–244. Materials Research Society, 1994.

- [67] Larry D. Merkle, Albert Pinto, Horacio R. Verdun, and Bruce McIntosh. Laser action from Mn^{5+} in $Ba_3(VO_4)_2$. *Applied Physics Letters*, 61(20):2386–2388, 16 November 1992.
- [68] Fred P. Milanovich. Stimulated raman scattering. In Marvin J. Weber, editor, *Optical Materials, Part I*, volume III of *Handbook of Laser Science and Technology*, pages 283–296. CRC Press, Boca Raton, Florida, 1986.
- [69] P. W. Milonni and L. E. Thode. Theory of mesospheric sodium fluorescence excited by pulse trains. *Applied Optics*, 31(6):785–800, 20 February 1992.
- [70] Peter W. Milonni, John M. Telle, Paul D. Hillman, and Robert Q. Fugate. Sodium guidestar pump laser requirements program. *Gemini Guide Star Laser Working Group*, December 1998.
- [71] J. R. Morris. Efficient excitation of a mesospheric sodium laser guide star by intervediate-duration pulses. *Journal of the Optical Society of America A*, 11(2):832–845, February 1994.
- [72] D. Mouillet, J. D. Larwood, J. C. B. Papaloizou, and A. M. Lagrange. A planet on an inclined orbit, as an explanation of the warp in the β pictoris disc. *Monthly Notes of the Royal Astronomical Society*, 292:896–904, 1997.
- [73] J. T. Murray, W. T. Roberts, Jr., W. L. Austin, R. C. Powell, and D. Bonaccini. Fiber raman laser for sodium guide star. In Domenico Bonaccini and Robert K. Tyson, editors, *Adaptive Optical System Technologies*, volume 3353 Part 1, pages 330–339. SPIE, 23-26 March 1998.
- [74] James T. Murray, William L. Autstin, and Richard C. Powell. End-pumped intracavity solid state raman lasers. In Walter R. Bosenberg and Martin M. Fejer, editors, *OSA Trends in Optics and Photonics on Advanced Solid-State Lasers*, volume 10 of *Topical Meeting*, pages 129–135. Optical Society of America, 1998.
- [75] Nancy G. Newberry, Eric J. Essene, and Donald R. Peacor. Alforsite, a new member of the apatite group: the barium analogue of chlorapatite. *American Mineralogist*, 66:1050–1053, 1981.
- [76] Ueli Oetliker, Markus Herren, Hans U. Gudel, Ute Kesper, Christa Albrecht, and Dirk Reinen. Luminescence properties of Mn^{5+} in a variety of host lattices: Effects of chemical and structural variation. *Journal of Chemical Physics*, 100(12):8656–8665, 15 June 1994.
- [77] Department of Materials Science Engineering. http://www.mse.arizona.edu/classes/mse222/1997_diamond/structure.htm, 1997. Web page maintained at the University of Arizona.

- [78] National Institute of Standards and Technology. http://physics.nist.gov/cgi-bin/AtData/main_asd, 2000. Atomic Spectroscopy Database maintained by NIST.
- [79] Scot S. Olivier, Jong An, Kenneth Avicaola, Horst D. Bissinger, James M. Brase, Herbert W. Friedman, Donald T. Gavel, Claire E. Max, J. Thaddeus Salmon, and Kenneth E. Waltjen. Performance of laser guide star adaptive optics at lick observatory. In R. Tyson and R. Q. Fugate, editors, *Adaptive Optical Systems and Applications*, volume 2534, pages 26–37. SPIE, July 1995.
- [80] G. C. Papen, C. S. Gardner, and J. Yu. Characterization of the mesospheric sodium layer. In *Adaptive Optics*, volume 13 of *OSA Technical Digest Series*. Optical Society of America, Washington D. C., 1996.
- [81] John M. C. Plane, Rachel M. Cox, Jun Qian, William M. Pfenninger, George C. Papen, Chester S. Gardner, and Patric J. Espy. Mesospheric na layer at extreme high latitudes in summer. *Journal of Geophysical Research*, 103(D6):6381–6385, March 27 1998.
- [82] Richard C. Powell. *Physics of Solid-State Laser Materials*. AIP Press, New York, 1998.
- [83] M. Prabhu, N. S. Kim, C. Li, J. Song, K. ueda, and C. Allen. 4.11 w raman fiber laser at 1239 nm using phosphosilicate fiber. In *Conference on Lasers and Electro Optics 2000*, page 544. Optical Society of America, 2000.
- [84] S. C. Rand and L. G. DeShazer. Visible color-center laser in diamond. *Optics Letters*, 10(10):481–483, October 1985.
- [85] Stephen C. Rand. Diamond lasers. In Gordon Davies, editor, *Properties and Growth of Diamond*, pages 235–239. INSPEC, London, 1994.
- [86] John F. Reintjes. Nonlinear optical processes. In Robert A. Meyers, editor, *Encyclopedia of Lasers and Optical Technology*, pages 332–384. Academic Press, Inc., San Diego, 1991.
- [87] Kevin S. Repasky, Lei Meng, Jason K. Brasseur, and John L. Carlsten. High-efficiency, continuous-wave raman lasers. *J. Opt. Soc. Am. B*, 16(5):717–721, May 1999.
- [88] W. T. Roberts, Jr., T. Martinez, and J. R. P. Angel. Sodium guide star laser used at the mmt. In *Laser Technology for Laser Guide Star Adaptive Optics Astronomy*. European Southern Observatory, 23-26 June 1997.

- [89] William T. Roberts, Jr., James T. Murray, W. L. Austin, Richard C. Powell, and J. Roger P. Angel. Solid-state raman laser for mmt sodium guide star. In *Adaptive Optical System Technologies*, volume 3353 Part 1. SPIE, 1998.
- [90] F. Roddier, A. Brahic, C. Dumas, J. E. Graves, B. Han, and M. J. Northcott. Adaptive optics observations of solar system objects. *Bulletin of the American Astronomical Society*, 29(3):1023, 1997.
- [91] F. Roddier, C. Roddier, A. Brahic, C. Dumas, J. E. Graves, and M. J. Northcott. First ground-based adaptive optics observations of neptune and proteus. *Planetary and Space Science*, 45(8):1031–1036, 1997.
- [92] François Roddier, editor. *Adaptive Optics in Astronomy*. Cambridge University Press, The Edinburgh Building, Cambridge CB2 2RU, UK, 1999.
- [93] Judith A. Ruffner. private communication, 1999.
- [94] Schott Glass Technologies, Inc. *Schott Optical Glass*, 1992.
- [95] D. C. Senft, G. C. Papen, C. S. Gardner, J. R. Yu, D. A. Krueger, and C. Y. She. Seasonal variations of the thermal structure of the mesopause region at urbana, il (40 degrees n, 88 degrees w) and ft. collins, co (41 degrees n, 105 degrees w). *Geophysical Research Letters*, 21(9):821–4, 1 May 1994.
- [96] Fang Shi. Sodium laser guide star experiment with a sum-frequency laser for adaptive optics. *Publications of the Astronomical Society of the Pacific*, 113:366–378, March 2001.
- [97] R. J. Shine, Jr., T. C. Merrill, A. J. Alfrey, E. K. Gustafson, and R. L. Byer. Design considerations for a 50-watt cw, fundamental mode, diode-pumped solid-state laser. In *Diode Pumping of Average-Power Solid State Lasers*, volume 1865, pages 17–27. SPIE - The International Society for Optical Engineering, 1993.
- [98] Richard L. Shoemaker. Class Notes from OPTI 511 at The University of Arizona, 1995.
- [99] Anthony E. Siegman. *Lasers*. University Science Books, 20 Edgehill Road, Mill Valley, CA 94941, 1986.
- [100] William T. Silfvast. *Laser Fundamentals*. Cambridge University Press, 40 West 20th St., New York, New York, 10011, USA, 1996.
- [101] M. Simon, L. M. Close, and Tracy L. Beck. Adaptive optics imaging of the orion trapezium cluster. *The Astronomical Journal*, 117:1375–1386, March 1999.

- [102] Krassimir Stankov. Private communication, 2001.
- [103] Jun Suda and Tsutomu Sato. Temperature dependence of the linewidth of the first-order raman spectra for CaWO_4 crystal. *Journal of the Physical Society of Japan*, 66(6):1707–1713, June 1997.
- [104] Satoru Sugano, Yukito Tanabe, and Hiroshi Kamimura. *Multiplets of Transition-Metal Ions in Crystals*. Academic Press, 111 Fifth Avenue, New York, New York, 10003, 1970.
- [105] Laird A. Thompson and Richard M. Castle. Experimental demonstration of a rayleigh-scattered laser guide star at 351 nm. *Optics Letters*, 17(21):1485–1487, November 1 1992.
- [106] Robert K. Tyson. *Principles of Adaptive Optics*. Academic Press, 525 B Street, Suite 1900, San Diego, CA 92101, 1998.
- [107] J. R. Unternahrer, H Sekiguchi, T. Motegi, and T. Mochizuki. 100 watt class moving slab glass laser. In *High Power Solid State Lasers*, volume 1021, pages 20–23. SPIE - The International Society for Optical Engineering, 1988.
- [108] R. K. Watts and W. C. Holton. New intermediate gain laser material: $\text{Y}_3(\text{Al}_{1-x}\text{Ga}_x)_5\text{O}_{12} : \text{Nd}^{\dagger}$. *Journal of Applied Physics*, 45(2):873–881, February 1974.
- [109] Robert C. Weast, editor. *The CRC Handbook of Chemistry and Physics*. CRC Press, Inc., Boca Raton, Florida, 1985.
- [110] Marvin J. Weber, editor. *Handbook of Laser Science and Technology*, volume 5. CRC Press, Boca Raton, Florida, 1987.
- [111] Jonathan C White. Stimulated raman scattering. In L. F. Mollenauer and J. C. White, editors, *Tunable Lasers*, pages 115–207. Springer-Verlag, Berlin, 1987.
- [112] Elizabeth A. Wood. *Crystals and Light*. Dover Publications, Inc., 180 Varick St., New York, NY, 10014, 1977.
- [113] James C. Wyant and Katherine Creath. Basic wavefront aberration theory for optical metrology. *Applied Optics and Optical Engineering*, XI:39, 1992.
- [114] Amnon Yariv. *Quantum Electronics*. John Wiley and Sons, New York, second edition, 1975.
- [115] Amnon Yariv and Pochi Yeh. *Optical Waves in Crystals*. John Wiley and Sons, New York, 1984.